National Institute of Technology Rourkela

Doctoral Thesis

Exploring the Physics and Application of biphasic La_2NiMnO_6 based Double Perovskites

A thesis submitted in fulfilment of the requirements
for the degree of Doctor of Philosophy

in Physics

Author:
Achyuta Kumar Biswal

Supervisor:
Dr. P.N. Vishwakarma

Department of Physics and Astronomy
National Institute of Technology Rourkela
Rourkela - 769008, Odisha, India

January 2016

Declaration of Authorship

I, Achyuta Kumar Biswal, declare that this thesis titled, 'Exploring the Physics and Application of biphasic La_2NiMnO_6 based Double Perovskites ' and the work presented in it are my own. I confirm that:

- This work was done wholly or mainly while in candidature for a research degree at this institute.
- Where any part of this thesis has previously been submitted for a degree or any other qualification at this institute or any other institution, this has been clearly stated.
- Where I have consulted the published work of others, this is always clearly attributed.
- Where I have quoted from the work of others, the source is always given. With the exception of such quotations, this thesis is entirely my own work.
- I have acknowledged all sources of help.
- Where the thesis is based on the work done by myself jointly with others, I have made clear exactly what was done by others and what I have contributed myself.

Signed: _____

Date: _____

Dr. P. N. Vishwakarma
Assistant Professor,
Department of Physics & Astronomy,
National Institute of Technology, Rourkela,
Odisha, India - 769008

Certificate

This is to certify that the research work embodied in the thesis entitled 'Exploring the Physics and Application of biphasic La_2NiMnO_6 based Double Perovskites ' is done by Mr. Achyuta Kumar Biswal under my supervision, towards the degree of Doctor of Philosophy at NIT Rourkela, Odisha, India. To the best of my knowledge and belief the thesis embodies the work of the candidate himself and fulfills the requirements of the ordinance relating to the Ph.D degree of the Institute. The contents of the thesis, in full or in parts, have not been submitted to any other Institute or University for the award of any degree.

Signed: _____

Date: _____

"You have a right to perform your prescribed duty, but you are not entitled to the fruits of action. Never consider yourself the cause of the results of your activities, and never be attached to not doing your duty."

Bhagwat Gita

Dedicated
to my
Family and Friends

NATIONAL INSTITUTE OF TECHNOLOGY ROURKELA

Abstract

Dr.P.N.Vishwakarma
Department of Physics and Astronomy

Doctor of Philosophy

Exploring the Physics and Application of biphasic La_2NiMnO_6 based Double Perovskites

by Achyuta Kumar Biswal

In the search of an alternative magnetoelectric material, La_2NiMnO_6(LNM) is a potential prototype due to its near room temperature ferromagnetic insulating nature, collosal magnetodielectricity & magnetoresistance. The biphasic composition is more interesting to study because of the inherent intrinsic lattice strain. In the present thesis various physical properties such as structural, surface morphology, electrical, magnetic, magnetoimpedance, magnetoresistance and gas sensing properties of biphasic LNM and its derivatives are studied. Low temperature impedance, resistance, magnetoresistance, magnetoimpedance measurements are done in a Closed Cycle Refrigerator. Interfacing of instruments are done by LabView software. Biphasic LNM and its Cu^{2+} doped derivatives are prepared from the combustion method of synthesis. M-LNM is prepared by impregnating the LNM pellet. Rietveld refinement of XRD data confirms the biphasic nature of samples with varying degrees of $R-3c$ and $Pbnm$ phases. Surface morphology study by FESEM show the size of the nanoparticles around $\sim$ 30nm. Strong correlation of dielectric relaxation with magnetic ordering is seen in LNM. Signature of Griffiths phase is seen in the magnetization data. Due to partial Cu^{2+} substitution, there is decrease in Curie temperature and saturation magnetization with enhancement of various antiferromagnetic interactions. The strength of Griffiths phase and intrinsic dielectric constant increases with Cu^{2+} substitution. Contrasting magneteimpedance behaviours comprising positive magnetoimpedance for LNM and negative magnetoimpedance for M–LNM is seen. Based on the conductance and magnetoresistance behaviour, the conduction mechanism is modelled as spin polarized tunnelling through insulating gap in LNM and through shunt resistances in M-LNM. Signature of inverse metamagnetic transition originating due to the dipolar field of $Pbnm$ phase acting on $R-3c$ phase is seen in magnetoresistance of M-LNM. Exploration of gas sensing property of LNM reveals maximum sensitive for Argon gas amongst N_2, Argon & O_2 .

Acknowledgements

. . . This doctoral thesis has been possible with the help and support of the kind individuals around me, to only some of whom it is possible to give particular mention here.

First and foremost, I owe my entire life to the grace of almighty, gurus and my motherland.

Secondly, I would like to acknowledge and extend my gratitude to my thesis supervisor Dr. P. N. Vishwakarma for his patience, constant support and encouragement, without which this work could not attained the shape which it has taken. While joining Ph. D., I had a little knowledge in this field of experimental research, but he showed his enormous patience and spent sufficient time to teach me instruments, data analysis etc. His immense knowledge, logical approach to tackle any problem and the sense of presentation has been a great motivation to me. His kind presence and advice at all my adverse situation is highly respectable. He is really a nice man.

I am thankful to the agencies like BRNS, BARC, India and CSIR India for providing the fellowships.

I would like to acknowledge Prof. Sunil Kumar Sarangi, Director, NIT Rourkela for his leadership and for improving the research environment in the institute.

Dr. V. Siruguri, Dr. P. D. Babu and Dr. M. K. Gupta is highly acknowledged for providing magnetization and x - ray diffraction facilities.

I would like to express my gratitude to all my Doctoral Scrutiny Committee members, Dr. S.C. Mishra (MM), Dr. D. K. Bisoyi (PH), Dr. S. Panigrahi (PH) and Dr. R. K. Sahoo (ME) for their useful discussions and constructive suggestions to improve the quality of this research work.

I am grateful to Dr. D.K. Pradhan for valuable discussions.

It gives me a great pleasure to thank my labmate Ms. Jashashree Ray for her cooperation and companionship. I acknowledge my labmates Mr. Sourav Kuila for assisting me in experiments. Mrs. Sanghamitra Acharya and Ms. Sweta Tiwary are acknowledged for their help.

I would like to thank to all the members of Department of Physics & Astronomy, NIT Rourkela.

I am also thankful to Mr. Ravinder Sharma & Mr. Somanath Das, for their constant help in the design and fabrication part.

I will always cherish the moments spent with Sukant, Prakash, Sudhansu, Rakesh Bhai, Satya Bhai, Ranjit Bhai, Jyoti Bhai, Baba Bhai, Bamadeva, Prakash, Surya, Kailash, Nilkantha, Satya, Krutika, Kadambimi, Bibek, Priyambada, Soumya, Binayak, Subhojit and Hari.

I would like to acknowledge all Swayamsevaks of Aryabhatt Sayam Sakha, NIT Rourkela. I am sure, with all the basic training we had in our sakha will be translated for the sake of our motherland.

I am always thankful to all the research scholars of Department of Physics & Astronomy.

I am indebted to Kalandi Bhai, Puskar Bhai, Silu Bhai and other well wishers of my family who helped financially, morally and stood with me during the most difficult phase of my life.

Finally, I am forever indebted to my parents and other members of my family for their constant encouragement, support and persistent love.

Achyuta Kumar Biswal
Roll No. - 510PH603,
Research Scholar,
Department of Physics & Astronomy,
National Institute of Technology, Rourkela,
Odisha, India - 769008

Publications

1. Dielectric relaxations in La_2NiMnO_6 with signatures of Griffiths phase.
   A. K. Biswal, J. Ray, P. D. Babu, V. Siriguri and P. N. Vishwakarma
   J. Appl. Phys. **115**, 194106 (2014)*.

2. Effect of Cu substitution on the magnetic and dielectric properties of La_2NiMnO_6.
   A. K. Biswal, J. Ray, P. D. Babu, V. Siriguri and P. N. Vishwakarma
   J. Appl. Phys. **117**, 17B728 (2015)*.

3. Exotic behaviour of magnetoresistance in the modified La_2NiMnO_6.
   A. K. Biswal, J. Ray, P. D. Babu, V. Siriguri and P. N. Vishwakarma
   Communicated*.

4. Gas Sensing Applications of La_2NiMnO_6.
   A. K. Biswal, J. Ray, S.Kuila, P. D. Babu, V. Siriguri and P. N. Vishwakarma
   AIP Conf. Proc. **1665**, 140050(1-3) (2015)*.

5. Low temperature magneto-dielectric measurements on $BiFeO_3$ lightly substituted by cobalt.
   J. Ray, **A. K. Biswal**, P. D. Babu, V. Siriguri and P. N. Vishwakarma
   J. Appl. Phys. **117**, 134102 (2015).

6. Magnetoelectricity in $BiFeO_3$ and $BiFe_{0.98}Co_{0.02}O_3$ nanoparticles.
   J. Ray, **A. K. Biswal**, P. D. Babu, V. Siriguri and P. N. Vishwakarma
   J. Alloys Compd. **628**, 32 (2015).

7. Magnetic and dielectric studies of Fe substituted sillenite phase bismuth cobaltite nanoparticles.
   J. Ray, **A. K. Biswal**, S.Kuila and P. N. Vishwakarma
   J. Alloys Compd. **633**, 370 (2015).

8. Signature of Griffith singularity in half doped $LaMn_{0.5}Cu_{0.5}O_3$.
   A. K. Biswal, J. Ray, P. D. Babu, V. Siriguri and P. N. Vishwakarma
   AIP Conf. Proc. **1591**, 1630 (2014).

9. Magnetic origin of dielectric transition in $BiFeO_3$.
   J. Ray, **A. K. Biswal**, P. D. Babu, V. Siriguri and P. N. Vishwakarma
   AIP Conf. Proc. **1591**, 1595 (2014).

10. Neutron diffraction studies on cobalt substituted $BiFeO_3$.
    J. Ray, **A. K. Biswal**, S. Acharya, P. D. Babu, V. Siriguri and P. N. Vishwakarma
    AIP Conf. Proc. **1512**, 1124 (2013).

11. Study of $Bi_2Sr_2CaCu_2O_8/BiFeO_3$ nano-composite for electrical transport Applications.
    S. Acharya, **A. K. Biswal**, J. Ray, and P. N. Vishwakarma
    J. Appl. Phys. **112**, 053916 (2012).

12. Effect of Co substitution on the magnetic properties of $BiFeO_3$.
    J. Ray, **A. K. Biswal**, S. Acharya, V. Ganesan, D. K. Pradhan and P. N. Vishwakarma
    J. Magn. Magn. Mater., **324**, 4084 (2012).

13. Near Room Temperature Giant Magnetodielectricity in $BiFeO_3/CoFe_2O_4$ composite
    S.Kuila, J. Ray, **A. K. Biswal**, P. D. Babu, V. Siriguri and P. N. Vishwakarma
    AIP Conf. Proc. **1665**, 130054(1-3) (2015).

14. Signature of relaxor behaviour in $BiFe_{0.98}Co_{0.02}O_3$.
    J. Ray, **A. K. Biswal**, S.Kuila, P. D. Babu, V. Siriguri and P. N. Vishwakarma
    AIP Conf. Proc. **1665**, 140058(1-3) (2015).

15. Neutron diffraction study of $BiFeO_3$ & $BiFe_{0.98}Co_{0.02}O_3$ nanoparticles.
    J. Ray, **A. K. Biswal**, P. D. Babu, V. Siriguri and P. N. Vishwakarma
    Solid state Commun. **1220**, 57 (2015).

16. Structural, ac conductivity scaling and magnetodielectric behaviour of a partially disordered insulating ferromagnetic double perovskite Eu_2NiMnO_6.
    M.G. Masud, H. Sakta, **A. K. Biswal**, P. N. Vishwakarma, B.K. Chaudhuri
    J. of Phys. D: Appl. Phys. **48**, 375504 (2015).

Present thesis is based on publications marked with *.

Contents

List of Figures

List of Tables

Abbreviations

w.r.t	**w**ith **r**espect **t**o
ZFC	**Z**ero **F**ield **C**ooling
FC	**F**ield **C**ooling
LNM	La_2NiMnO_6
CFO	$CoFe_2O_4$
XRD	**X**-**R**ay **D**iffraction
FESEM	**F**ield **E**mission **S**canning **E**lectron **M**icroscope
LIA	**L**ock **I**n **A**mplifier
DUT	**D**evice **U**nder **T**est
CCR	**C**losed **C**ycle **R**efrigerator
VSM	**V**ariable **S**ample **M**agnetometer
PPMS	**P**hysical **P**roperty **M**easurement **S**ystem
MI	**M**agnetoimpedance
MR	**M**agnetoresistance
GMR	**G**iant **M**agnetoresistance
CMR	**C**olossal **M**agnetoresistance
TMR	**T**unneling **M**agnetoresistance
AMR	**A**nisotropic **M**agnetoresistance
MD	**M**agnetodielectric
CMD	**C**olossal **M**agnetodielectric

Physical Constants

Speed of Light	c	=	$2.997\ 924\ 58 \times 10^{8}$ m/s
Bohr magneton	μ_B	=	$9.27400968(20) \times 10^{-24}$ J/T
Permittivity of Vacuum	ϵ_0	=	$8.854\ 187\ 82 \times 10^{-12}$ F/M
Permeability of Vacuum	μ_0	=	$1.256\ 637\ 06 \times 10^{-6}$ H/M

Chapter 1

Introduction

1.1 Perovskite Oxides

Perovskites, named after Russian mineralogist Lev Perovski, are the compounds having same crystal structure as Calcium Titanate ($CaTiO_3$) or ABO_3, where A is a large sized 12 coordinated ion and B is a small size 6 coordinated ion. The B - atom is in coordination with six oxygen atoms forming BO_6 octahedra. The crystal structure of $BaTiO_3$ representing an ideal perovskite cell is shown in fig.1.1.

The structure and physical properties largely depend on the nature of B – site ion and the B – O bond lengths of BO_6 octahedra. Ideal perovskite structure is generally a cubic lattice but very often oxides choose a lower symmetry (e.g. hexagonal or orthorhombic) structure. The deviation from the ideal cubic structure is expressed as Goldschmidt tolerance factor (t)[1].

$$t = \frac{(r_A + r_O)}{\sqrt{2}(r_B + r_O)} \tag{1.1}$$

where r_A & r_B are the radius of A and B site cations respectively and r_O is the radius of oxygen anion. For an ideal cubic structure, t = 1. The value of t lies between approximately 0.80 and 1.10 for many of the perovskites[1]. For

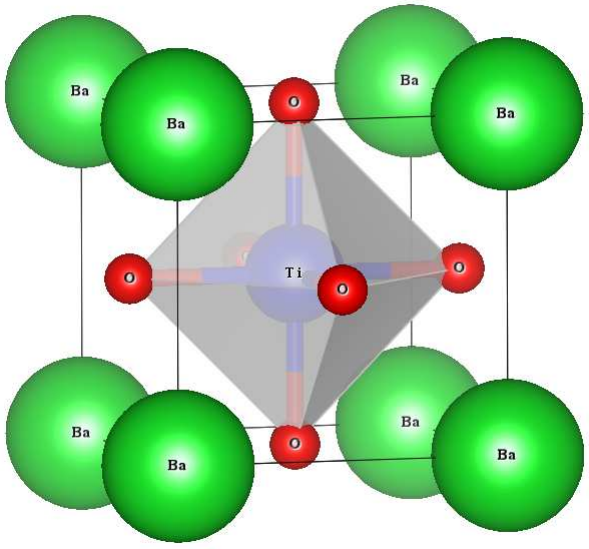

FIGURE 1.1: Ideal perovskite structure representing a cubic $BaTiO_3$ unit cell.

orthorhombic structure t = 0.7 to 0.9 ($GdFeO_3$ t = 0.81). For a monoclinic structure t < 1, the perovskite becomes hexagonal for t > 1 ($BaNiO_3$, t = 1.13).

Typical Property	**Typical Compounds**
Ferroelectric Property	$BaTiO_3$,$PbTiO_3$
Piezoelectricity	$Pb(ZrTi)O_3$,$(BiNa)TiO_3$
Electrical conductivity	ReO_3,$SrFeO_3$,$LaCoO_3$,$LaNiO_3$,$LaCrO_3$,
Superconductivity	$La_{0.9}Sr_{0.1}CuO_3$, $YBa_2Cu_3O_7$, $HgBa_2Ca_2Cu_2O_8$
Ion conductivity	$La(Ca)AlO_3$,$CaTiO_3$, $La(Sr)Ga(Mg)O_3$, $BaZrO_3$, $SrZrO_3$,$BaCeO_3$
Magnetic Property	$LaMnO_3$, $LaFeO_3$, La_2NiMnO_6
Catalytic property	$LaCoO_3$, $LaMnO_3$,$BaCuO_3$
Electrode	$La_{0.6}Sr_{0.4}CoO_3$, $La_{0.8}Ca_{0.2}MnO_3$

TABLE 1.1: Typical properties of Perovskite oxides[1].

Due to the strong correlation between the structure and physical properties, perovskite oxides are one of the most investigated compounds among the researchers. The diverse physical properties exhibited by the perovskite compounds are listed in Table. 1.1[1].

1.2 Double Perovskite Oxides

Double perovskites have the general chemical formula $A'A''B'B''O_6$, where the primes distinguishes between the possible cations. The tolerance factor (t) of a double perovskite structure is represented as [2]

$$t = \frac{((r_{A'} + r_{A''})/2) + r_O}{\sqrt{2}((r_{B'} + r_{B''})/2) + r_O} \tag{1.2}$$

where the symbols have their usual meanings.

Depending on the arrangement of B' and B'' cations in the crystal, the double perovskites can be categorized as random, rock salt and layered(see fig.1.2). The compounds which have random sublattice have no B – site ordering. The cubic lattice with space group $Pm\bar{3}m$ and orthorhombic lattice with space group $Pbnm$ are random double perovskites. The rock salt and layered type double perovskites have ordered B – site cations. The ordering of B – site cations depend on the charge difference between B' and B''. The double perovskite is more ordered when

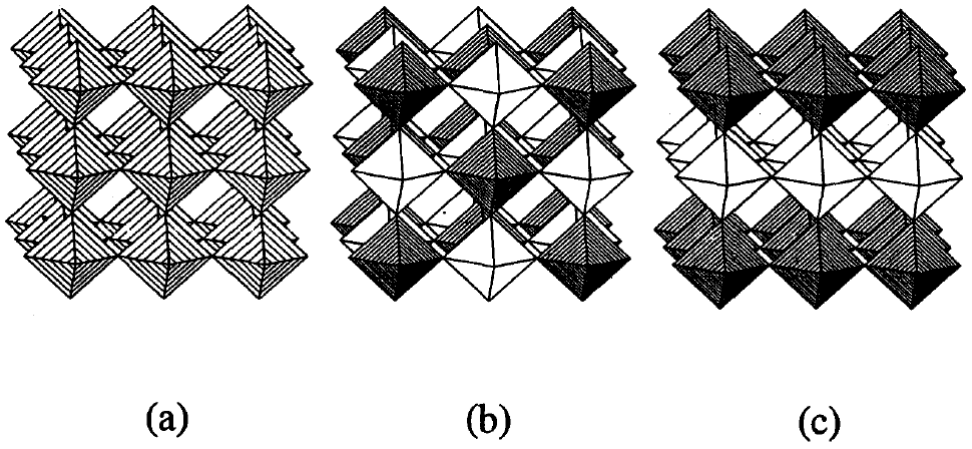

FIGURE 1.2: Classification of Double perovskites depending on B - site atom occupation a. random, b. rock salt & c. layered [2].

the charge difference is greater than 2. The order - disorder effect are mostly encountered when the charge difference is two or less. The rock salt type configuration have alternate B' and B'' cationic arrangements. Cubic lattice (space

group: $Fm\bar{3}m$) and monoclinic sublattice (space group: $P2_1/n$) are the few examples of rock salt configurations. The layered double perovskite is realized when $B^{'}$ and $B^{''}$ cations are arranged in alternate layers (see fig.1.2). The layered double perovskite usually crystallizes in the monoclinic sublattice (space group: $P2_1/m$).

Generally the $B^{'}$ and $B^{''}$ cations determine the physical properties. Among the double perovskites Sr_2CoMoO_6 (SCMO) & Sr_2FeMoO_6 (SFMO) are the most studied compounds. The Fe/Co and Mo ions order in rock salt type superlattice structure. The compound has drawn much attention due to its high ferromagnetic (FM) Curie temperature ($T_C \sim 400K$) and half metallic character opening up the possibility for room temperature spintronics applications [3]. The magnetic property is fundamentally very much interesting due to its high FM T_C. The high FM T_C is counter-intuitive because the superexchange interaction of neighbourhood magnetic ions Fe–O–Mo–O–Fe results antiferromagnetic (AFM) order[4]. The ferromagnetism is explained on the basis of hybridization driven mechanism. The Mo t_{2g} energy levels, which are energetically placed within the spin split energy levels of Fe d orbitals, attain a negative spin polarization through hybridization between Mo t_{2g} and Fe t_{2g} levels, which in turn stabilizes the parallel alignment of spins in Fe sublattice[4]. SCMO also shows beautiful magnetotransport properties, where the MR behaviour is due to inter-grain tunnelling via physical grain boundary. The intrinsic intra grain MR is very low. Signatures of spin-valve type MR is also seen in SFMO [5].

Recently, manganite double perovskites like La_2NiMnO_6 and La_2CoMnO_6 have drawn much attention due to spectacular properties such as colossal magnetoresistance, colossal magnetodielectricity and room temperature ferromagnetism[6–9]. In particular, La_2NiMnO_6 (LNM) have been of considerable interest because of the rich physics involved and their prospects for spintronics applications such as magnetodielectric capacitor[10], spin based sensors, multiple state memory elements[11] and spin tunnelling junctions[12]. Since these compounds belong to the family of manganites so it is essential to understand the physical aspects viz. magnetism and transport behaviour before describing these double perovskites.

1.3 Physical aspects of manganites

1.3.1 Magnetic interactions

The magnetism in manganites appear due to the indirect interaction between the d-orbitals of manganese via the p-orbital of in-between oxygen anion. As the two metal ions need the bridging oxygen atom for mediating the interaction, hence termed as indirect exchange interaction. In this process, the conduction electron of one magnetic ion induces a spin polarization in the neighbouring ion, which is felt up to a certain range. In case of manganites, various indirect interactions e.g. superexchnage, double exchange, etc. are responsible for the ordering of individual magnetic moments.

1.3.1.1 Superexchange interaction

Superexchange interaction takes place between two magnetic cations mediated via a non-magnetic anion. This interaction was introduced by Goodenough. The material which exhibits superexchange interaction may result ferro or antiferromagnetism as shown in fig.1.3. This ferro/antiferromagnetism is governed by the Pauli's exclusion principle. Thus, a) the ferromagnetism results when the superexchange interaction is exhibited between a fully filled d-orbital and a half filled d-orbital of magnetic cations via a non-magnetic anion. b) If both the magnetic ions have half filled d-orbital, then the resulting interaction is antiferromagnetic. c) if either a half filled or filled orbital interacts with a vacant orbital, the result can be either antiferromagnetic or ferromagnetic, but in most cases it favours ferromagnetic. In general, the superexchange interaction is derived from the second order perturbation theory. According to this theory, the superexchange interaction is strongly dependent upon the metal – oxygen – metal bond angle.

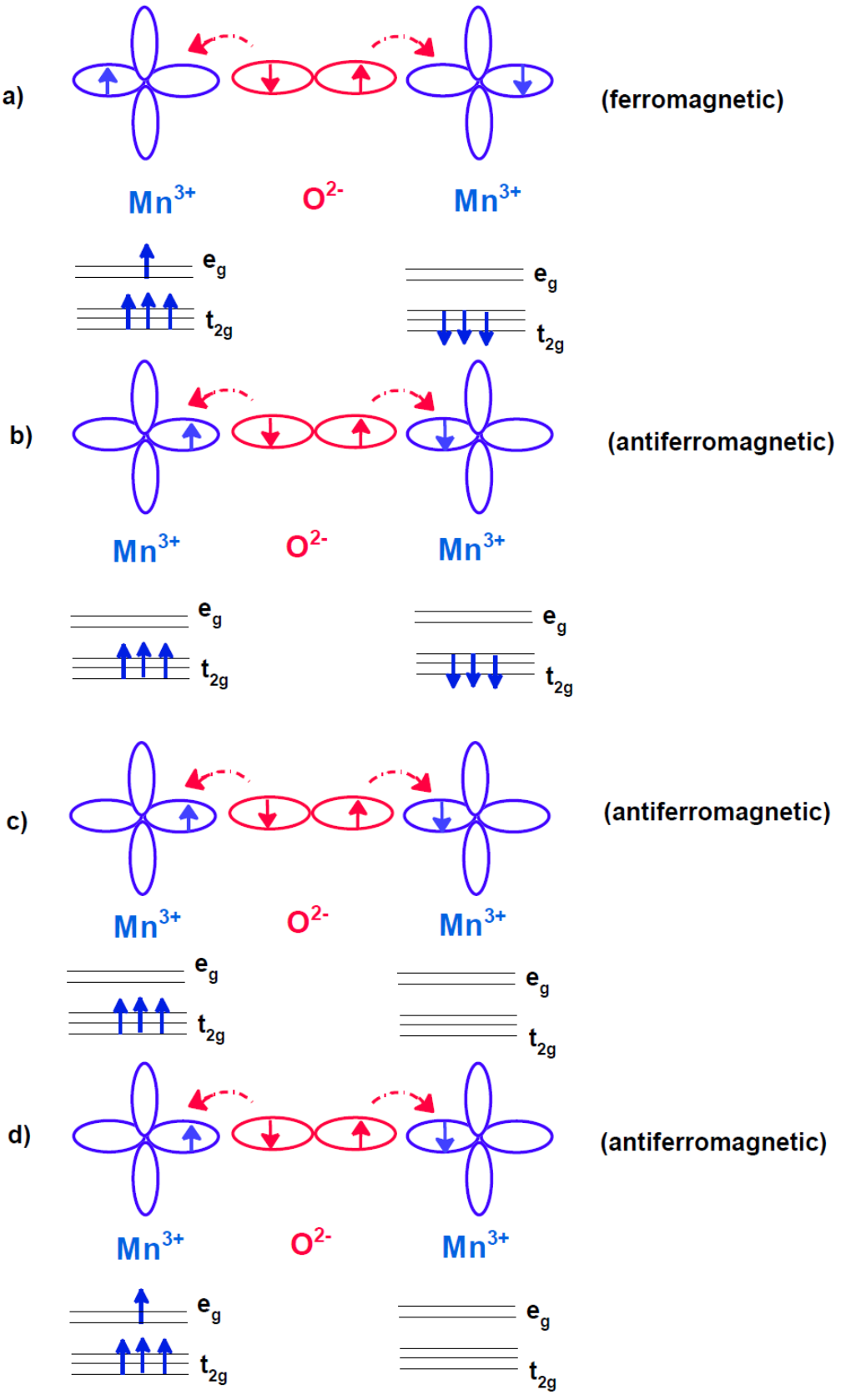

FIGURE 1.3: Superexchange interactions in several ferromagnetic and antiferromagnetic configuration.

1.3.1.2 Double - exchange interaction

This type of exchange interaction proposed by Zener induces ferromagnetic order. This interaction arises in the presence of magnetic cations of different oxidation states. In case of manganites, the electron of Mn^{3+} couples with the Mn^{4+} cation. According to Zener, the transfer of electron does not change the electron's spin. So it is expected that the exchange results only the parallel coupling between Mn^{3+} and Mn^{4+}. The electrons are arranged in their orbitals by following the Hund's rule.

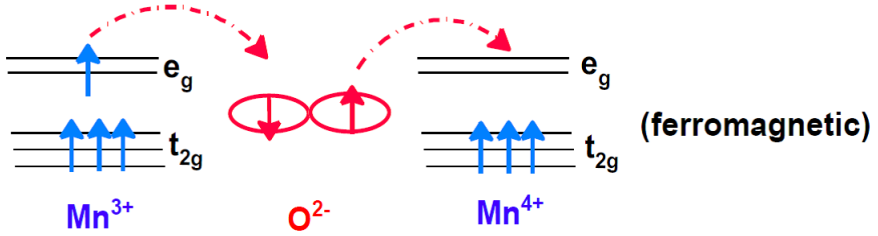

FIGURE 1.4: Double - exchange interaction due to multiple oxidation states of manganese.

Fig.1.4 shows that the electron jumps from the p-orbital of oxygen to Mn^{4+} cation, as its e_g orbital is vacant. As a result, an electron jumps from the neighbouring Mn^{3+} cation to the p-orbital of oxygen to refill it. In the end, the electron has travelled between the two neighbouring Mn ions of different oxidation state retaining its spin. This double exchange favours the ferromagnetism as this interaction facilitates the retention of electrons spin direction. So, the concept of ferromagnetic double exchange interaction is based on two simultaneous electron transfers: one from Mn^{3+} to oxygen 2p orbital and another one from oxygen 2p orbital to Mn^{4+} ion.

Anderson and Hasegawa calculated the FM interaction between two magnetic ions by using the concept of double exchange interaction and de Gennes proposed a canting state for the weakly doped compounds[13, 14]. Kumar *et. al.*, and Sen *et. al.*, discussed the appearance of randomly localized polarons in manganites due to the double exchange interaction and demonstrated that the lattice polaron effects

and spin fluctuations are controlled by the extrinsic disorder[15, 16]. An increase in the structural distortions leads to a decrease in the ferromagnetic component.

1.3.1.3 Crystal field splitting

The magnetic interactions in perovskite oxides are also governed by crystal filled splitting. In the perovskite structure, the transition metal ion is surrounded by the oxygen octahedra. In case of manganites, the central transition metal Mn ion is surrounded by the oxygen octahedra. As a result these degenerate d-orbitals get separated into lower triply degenerate t_{2g} orbitals and upper double degenerate e_g orbitals as shown in fig.1.5. The energy gap between these two levels is defined by crystal field splitting energy ($\triangle_{CF}$) and this energy is $\sim$ 1.5eV [17]. As it is well known that, manganites exhibit different oxidation state, so the e_g electrons may be localized or itinerant. The itinerant electron(s) interacts with the neighbouring e_g electron via the oxygen anion. While the electrons lying in the t_{2g} orbitals are considered as localized electrons having the net spin 3/2 μ_B.

In addition to the crystal filed splitting, manganites also undergo the Jahn – Teller distortion (JT distortion) when the e_g orbital are occupied by single electron. This interaction results a deformation of the oxygen octahedra surrounding the Mn cation. Hence, the deformation lifts the degeneracy of the e_g levels and results in the lowering of electronic energy as shown in fig.1.5. The manganites, having Mn^{3+} cations ($3d^4$) in an octahedral environment exhibit JT distortion whereas the Mn^{4+} cations ($3d^3$) would not show this effect because there is no net lowering of the electronic energy by a distortion [18]. This effect is termed as static JT effect. However, the distortion may switch from one axis to another and this effect mostly appears in the case of mixed valence manganites. This kind of distortion is known as dynamic JT distortion. In general, it has been observed that the JT effect mediates a coupling between the electrons and phonon in manganites [19]. The JT distortion plays a crucial role for determining the insulating and conducting behaviour in case of manganites.

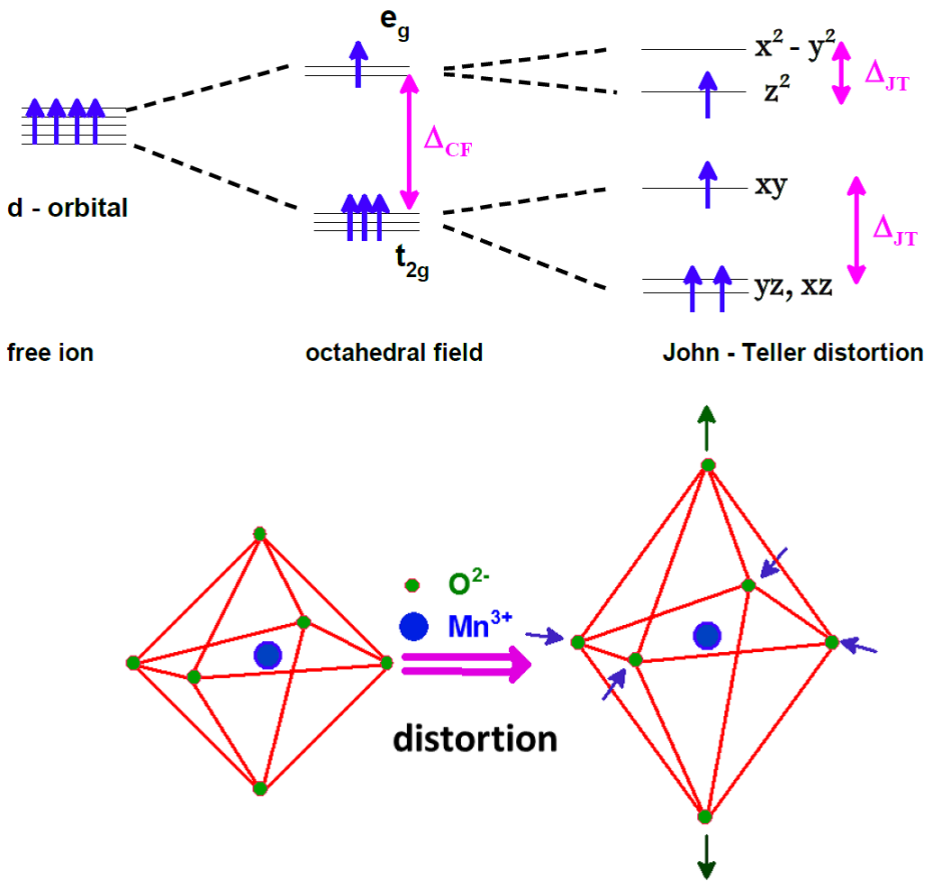

FIGURE 1.5: Energy level splitting due to crystal field and John - Teller distortion(top). Distortion of octahedra due to crystal field(bottom).

1.3.2 Griffiths Phase

Phase inhomogeneity and quenched disorder in manganites have drawn considerable attention among researchers. Phase inhomogeneity involves the pre-formation of ferromagnetic clusters at temperatures above the critical temperature T_C of ferromagnetic matrix. Quenched disorder is introduced due to the random distribution of substituted ions and local lattice distortion by John – Teller active ion Mn^{3+}. Both, phase inhomogeneity and quenched disorder leads to Griffiths singularity/phase[20]. Though the Griffiths singularity was initially proposed for randomly diluted Ising ferromagnets, it is commonly observed in R-site substituted manganites, $R_{1-x}A_xMnO_3$ (where R = La^{+3}, Pr^{+3} and A = Ca^{+2}, Sr^{+2}, Ba^{+2}). In these compounds, ferromagnetism via double exchange mechanism, is felicitated

by the substitution of divalent cations at La site and Griffiths singularity arises due to inhomogeneity and quenched disorder brought by divalent substitution. Apart from this, Griffiths phase is also observed in some double perovskite manganites Tb_2NiMnO_6[21] and La_2CuMnO_6[22].

The Griffiths phase is marked as a rapid downfall of the inverse susceptibility as a function of temperature, before the arrival of actual ferromagnetic transition from high temperature side. This rapid fall recovers with increase in external magnetic field. Such a non-linear behaviour and its disappearance with magnetic field is an indication of Griffiths phase. Appearance of Griffiths singularity is due to the formation of ferromagnetic clusters in the paramagnetic state, much before the long range ferromagnetic order sets in. These ferromagnetic clusters align themselves in the magnetic fields leading to deviation from Curie-Weiss (CW) behaviour much before the actual ferromagnetic Curie temperature. Griffiths singularity is very often characterized by power law behaviour.

$$\chi^{-1} \propto (T - \theta)^{1-\lambda} \tag{1.3}$$

This power law behaviour is a modified CW law, where θ is the critical temperature of ferromagnetic clusters in the paramagnetic matrix and the parameter $0 \leq \lambda \leq 1$ marks the deviation from CW law. For CW law $\lambda = 0$ and $\lambda > 0$ implies occurrence of Griffiths phase.

1.3.3 Magnetoresistance

The influence of external magnetic field on the electrical resistance of a material is termed as magnetoresistance (MR). In magnetic materials, the spin configurations influence the motion of electrons. Due to external magnetic field the spin arrangement inside the material changes with subsequent change in mobility of electrons. Mathematically magnetoresistance is defined as

$$MR(\%) = \left[\frac{R(H) - R(0)}{R(0)}\right] \times 100 \tag{1.4}$$

It is a unit less quantity and usually MR is quantified by percentage change in resistance value. The observed MR behaviours in materials are broadly categorized into following types.

1.3.3.1 Normal magnetoresistance

Under external magnetic field the drifting electrons experience the Lorentz force. So the free electrons under the simultaneous influence of electric and magnetic field swirl in a spiral trajectory. Hence there is always increase in resistance (+ve MR) for a non – magnetic metal under the influence of magnetic field[23].

1.3.3.2 Anisotropic magnetoresistance (AMR)

The AMR phenomenon is seen in polycrystalline bulk materials. The physical origin of AMR is the spin orbit coupling effect. Due to spin orbit interaction, the s-electrons scatter into minority d-state which in turn increase the resistance[23]. The anisotropy originates due to the difference in scattering cross section of d state for parallel and perpendicular orientation between the current flow and magnetic field as depicted in fig.1.6[23].

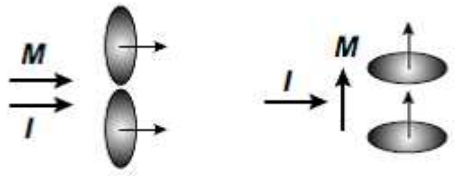

FIGURE 1.6: Scattering cross section of d-state for parallel and perpendicular orientation between the current flow and magnetic field[23].

For polycrystalline materials the AMR can be represented mathematically as

$$R(\theta) = R_{\perp} + (R_{\parallel} - R_{\perp}).cos^2(\theta_M - \theta_I) \tag{1.5}$$

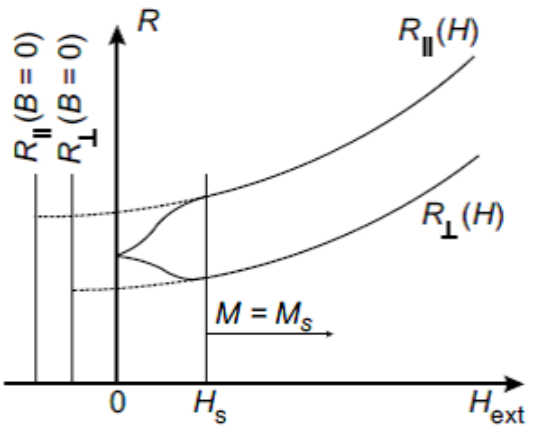

FIGURE 1.7: Demonstration of AMR effect for both perpendicular and parallel field directions[23].

where $R_{\perp}$ and $R_{\parallel}$ are the resistivity perpendicular and parallel to the magnetic field. θ_M and θ_I are the angles made by current and magnetization w.r.t a given direction (see fig.1.7[23]).

1.3.3.3 Colossal magnetoresistance (CMR)

Some compounds, specifically transition metal oxides show large change in resistance associated with paramagnetic to ferromagnetic transition. The maximum MR change was reported about several 100% at room temperature and was reached up to a value as high as 10^8% at low temperatures[23]. The CMR effect is realized in mixed valance manganites where Mn ion exhibits different oxidation states. As described in the section 1.3.1.2, double exchange is the underlying phenomenon associated with the FM to PM transition. Due to spin correlation among the localized electrons in FM state, hopping becomes easier between parallel spins. But in PM state due to spin disorder the hopping process is inhibited. Hence, there is increase in mobility in FM state below T_C. Thus there is always –ve MR in CMR effect. One such example of mixed valance manganite is $La_{0.75}Ca_{0.25}MnO_3$ which contain Mn^{3+} and Mn^{4+} ions [24]. As described in the fig .1.8 the magnetic transition is associated with insulator to metal transition. The associated CMR is achieved up to – 80% at 4T magnetic field as depicted from the fig.1.8[24]. The CMR effect is well explained by double exchange mechanism for FM metallic

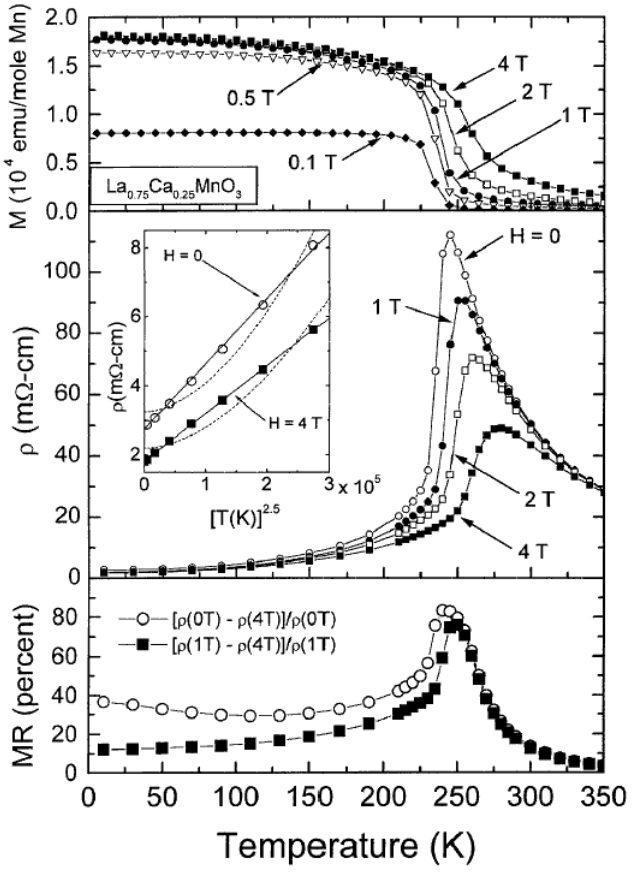

FIGURE 1.8: CMR effect in by $La_{0.75}Ca_{0.25}MnO_3$, where the MR is associated with PM - FM transition[24].

phase. Sometimes the high resistance in FM phase and associated MR couldn't fully explained by double exchange mechanism. Other possible explanations include the formation of small lattice polaron in the paramagnetic state. Hence the electron phonon coupling is also a possible cause of CMR.

1.3.3.4 Giant magnetoresistance (GMR)

The giant magneto resistance (GMR) is another spin dependent magneto transport phenomenon realized in FM/metal/FM junctions. The maximum GMR effect is realized upto several 100% at room temperature. The GMR effect is associated with the exchange coupling at the interface between the magnetic and non-magnetic layers. The exchange coupling is found to be affected by the thickness of the metallic spacer layer [25].

The resistance of the junction depend on the relative orientation of the magnetizations of the FM layers. The junction possesses high resistance for anti-parallel orientations and low resistance for parallel orientations. The GMR phenomenon is beautifully explained in in fig.1.9 for Fe and Cr multi-layers [23, 26]. For antiferromagnetic coupling between the layers the applied field forces the interlayer moments to orient parallely and hence decrease the resistance with increase in magnetic field.

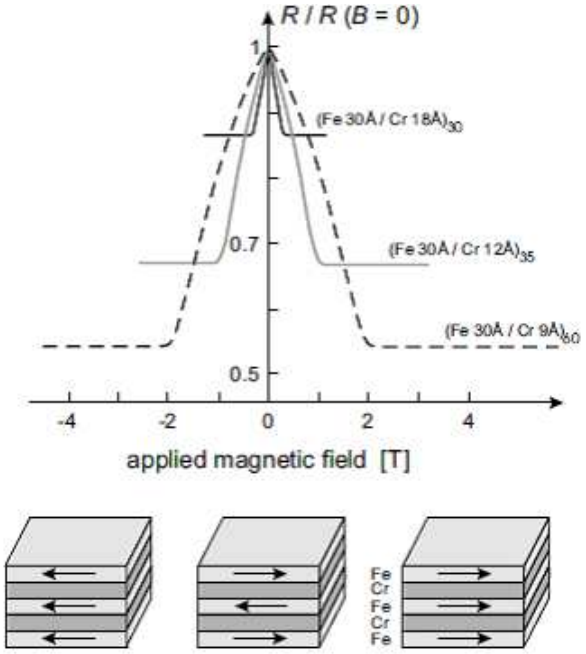

FIGURE 1.9: GMR effect shown in Fe/Cr multilayers[23, 26].

The GMR effect is described mathematically by

$$GMR = \frac{\rho_{ap} - \rho_p}{\rho_p} = \frac{\sigma_p}{\sigma_{ap}} - 1 \tag{1.6}$$

Where ρ_{ap} and ρ_p are the resistivity in anti-parallel and parallel configurations of magnetization respectively and the σ notations represent their corresponding conductance counterparts.

1.3.3.5 Tunnelling magnetoresistance (TMR)

The tunnelling magneto resistance (TMR) is realized in FM/insulator/FM type magnetic junctions. The mere difference with GMR is the insulating spacer layer, so the electron has to tunnel through the insulating barrier to reach the other electrode. TMR can also be present in FM nanoparticles embedded in the insulating matrix as represented in fig.1.10[23]. TMR can reach upto 50% at room

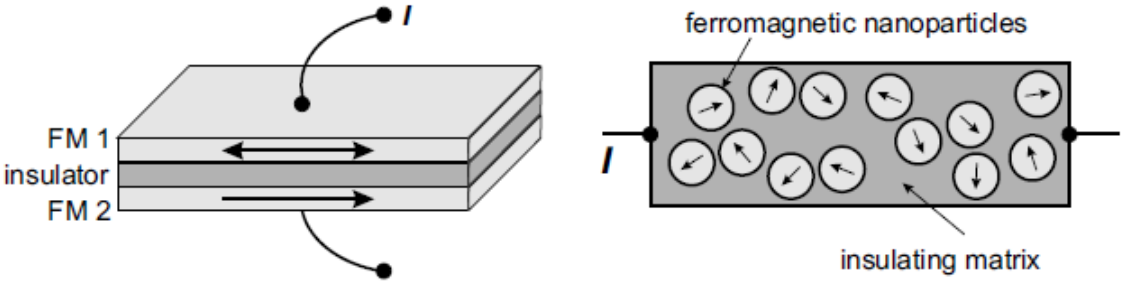

FIGURE 1.10: TMR effect in multilayers and polycrystalline materials[26].

temperature. Mathematically TMR effect can be represented as

$$TMR = \frac{R_{ap} - R_p}{R_p} \tag{1.7}$$

where R_{ap} and R_p are resistances in anti-parallel and parallel configurations of magnetizations respectively.

The effect is originally discovered in 1975 by Julliere in Fe/Ge-O/Co junction. According to Julliere the TMR can be calculated from the spin polarization density of states (D) at the fermi level by eq.1.8.

$$TMR = \frac{D_{\uparrow}(E_F) - D_{\downarrow}(E_F)}{D_{\uparrow}(E_F) + D_{\downarrow}(E_F)} \tag{1.8}$$

where, the up arrow term represents the density of spin up electrons at the fermi level aligned parallel to the magnetic field direction and down arrow term represent the density of spin down electrons at the fermi level aligned anti-parallel to the external field.

So TMR can be written based on spin polarization as

$$TMR = \frac{2P_1P_2}{1 - P_1P_2} \tag{1.9}$$

where, P_1 and P_2 are the spin polarizations of the two ferromagnets in the junction.

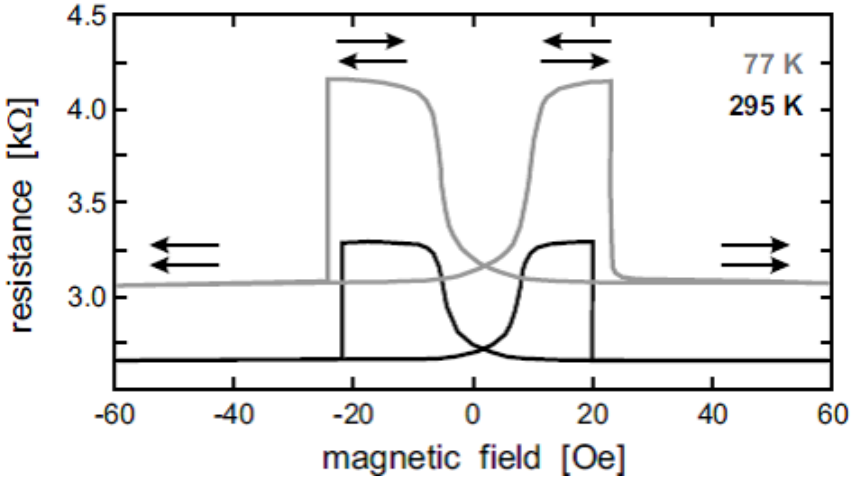

FIGURE 1.11: TMR behaviour of Co – Al_2O_3 – NiFe junction at 295K and 77K[27].

Fig.1.11 represent the TMR behaviour of Co–Al_2O_3 – NiFe junction [27]. Here Al_2O_3 act as the insulating layer. Due to different coercivities of the FM layers, anti-parallel arrangement (maximum resistance) of magnetization is achieved at some intermediate field range and with further increase in magnetic field a parallel alignment (minimum resistance) is preferred. TMR magnitude of 27% is obtained at 77K for the above mentioned junction, however at 295K the effect is about 20%.

The magnetic properties of La_2NiMnO_6 and La_2CoMnO_6 are governed by superexchange interactions. TMR magnetotrasnport phenomenon are reported for these manganite double perovskites.

1.4 Ferrmagnetic phase transition & Arrott Plot

According to Ginzburg-Landau-Wilson theory, free energy of a magnetic metal is[28]

$$F(M) = aHM + bM^2 + cM^4 + ... \tag{1.10}$$

The minimization of the free energy, i.e., $dF/dM = 0$, results mean field equation of state.

$$M^2 = a^{'} + b^{'}\frac{H}{M} + ... \tag{1.11}$$

where $a^{'} \propto \chi^{-1}$, being zero at $T = T_C$. The plot of M^2 *vs* H/M isotherms is called Arrott plot. The shape of the isotherms should be straight lines in the critical region having zero intercept at $T = T_C$, where $M \propto H^{1/3}$[29]. The saturation magnetization(M_S) and the inverse susceptibility (χ^{-1}) can be determined from the intercepts of the isotherms in $T \leq T_C$ and $T \geq T_C$ regions respectively[30]. The positive slopes in Arrott plots indicate a second order magnetic transition.

Based on Arrott – Noakes equation of state[31], the critical scaling exponents of magnetization $\beta, \gamma \,\&\, \delta$ can be extracted from the critical scaling approach. The critical exponent β characterizes the order parameter M for $T < T_C$. Similarly γ characterizes the susceptibility χ for $T > T_C$ and δ represents the influence of magnetic field H on the magnetization M at $T = T_C$. A generalized form of mean field equation of state (eq.1.11), which includes critical fluctuations and obeys the scaling law is given by equation 1.12.

$$M^{\frac{1}{\beta}} = a^* + b^*\left(\frac{H}{M}\right)^{\frac{1}{\gamma}} + ... \tag{1.12}$$

The above equation yields the modified Arrott plot $M^{1/\beta}$ *vs* $(H/M)^{1/\gamma}$. At $T = T_C$, the isotherm is a zero intercept straight-line for which $M \propto H^{1/\delta}$. The saturation magnetization and the susceptibility are related to the critical exponents by the following relations.

$$M_S(T) = M_0 \mid \epsilon \mid^{-\beta},\ \epsilon < 0, T < T_C \tag{1.13}$$

$$\chi_0^{-1} = (h_0/M_0)\epsilon^{\gamma},\ \epsilon > 0, T > T_C \tag{1.14}$$

where $\epsilon = (T - T_C)/T_C$ is the reduced temperature and $M_0, h_0/M_0$ are the critical amplitudes.

1.5 Impedance spectroscopy

Complex impedance spectroscopy is a powerful technique for characterizing the electrical properties of the materials. This technique analyses the a.c. electrical response of a material, when it is subjected to a small sinusoidal electrical perturbation. So the response data can be collected in varied amplitude and frequency conditions. The dynamics of bound and mobile charge carriers present in bulk as well as in the interface regions can also be analysed by using this technique [32].

The a.c. electrical response of a material can be represented in four inter-convertible formats as represented below.

Complex impedance: $Z^* = Z^{'} - jZ^{''}$

Complex admittance: $Y^* = (Z^*)^{-1}$

Complex permittivity: $\epsilon^* = (j\omega C_0 Z^*)^{-1} = \epsilon^{'} - j\epsilon^{''}$

Complex modulus: $M^* = j\omega C_0 Z^* = M^{'} + jM^{''}$

Where $j = \sqrt{-1}$, $\omega = 2\pi f$ is the angular frequency and $C_0 = \epsilon_0 A d^{-1}$ in which C_0 is the vacuum capacitance of the cell without the sample. A and d are the sample effective area and thickness respectively.

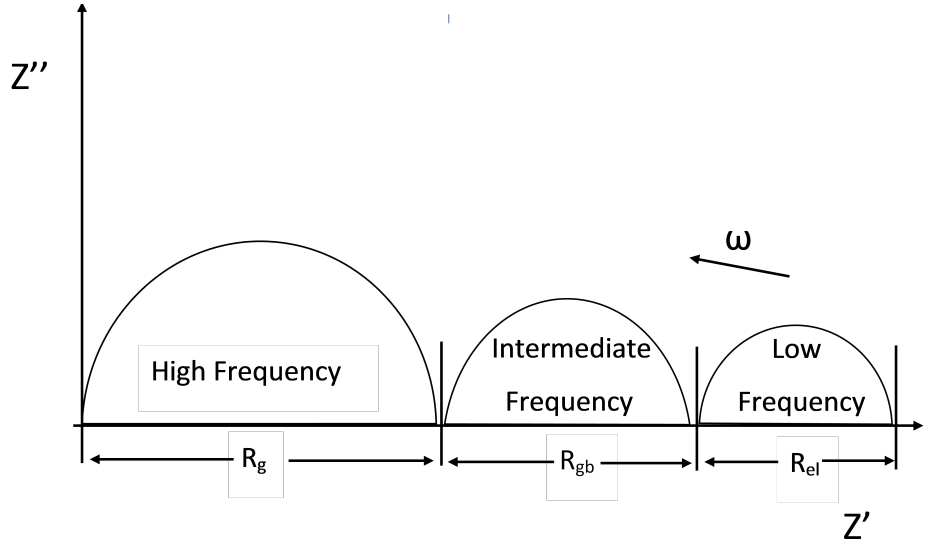

FIGURE 1.12: The relaxations due to grains(R_g), grain boundaries(R_{gb}), & sample electrode interface(R_{el}) in a polycrystalline material represented in complex argand diagram.

The data represented in complex argand diagram appears as multiple semicircles representing the various relaxation phenomenon taking place within the material.

The relaxations due to grains, grain boundaries and interface are given in the fig.1.12. The grain boundaries and electrode contain trapped air molecules (space charges) which easily responds at lower frequencies. However the relaxation of the grains is due to the occurrence of intrinsic dipolar polarization at high frequency. The grain and grain boundaries relax with different relaxation times due to the difference in their conductivities. Similarly crystallographic phases also show different relaxations. The relaxations due to crystallographic phases is evident in fig.1.13. The 2.2 mole % Y_2O_3 in ZrO_2 show a large bulk arc (fig.1.13a) due to tetragonal and orthorhombic phases. However 3.4 mole % Y_2O_3 in ZrO_2 sample displays a single high frequency arc (fig.1.13b) due to the tetragonal phase only[32].

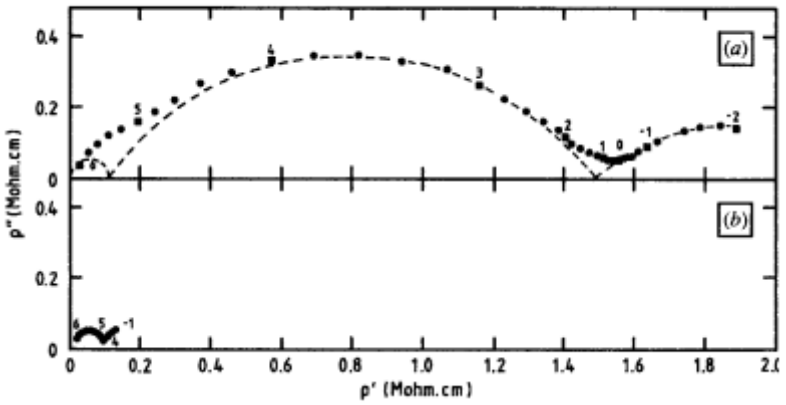

FIGURE 1.13: a. The high frequency large bulk arc is due to tetragonal and orthorhombic phases of 2.2 mole% Y_2O_3 in zirconia. b. The small high frequency arc is due to only tetragonal phase for 3.4 mole % Y_2O_3 in zirconia[32].

These relaxations are understood by different theoretical models viz. Debye, Maxwell-Wagner, Cole-Cole, Cole-Davidson and Harverliak-Negami equations.

1.5.1 Debye relaxation

It is the most basic relaxation model in dielectrics since its inception[32]. This model is applicable for ideal dielectrics with single relaxation time. Mathematically

Debye type relaxation can be expressed as

$$\epsilon^*(\omega) = \epsilon_\infty + \frac{\epsilon_s - \epsilon_\infty}{1 + j\omega\tau} \tag{1.15}$$

where ϵ_s, ϵ_∞ low and high frequency permittivity and τ represents the relaxation time. The real and imaginary part of the permittivity have the same relaxation times as evident from fig.1.19.

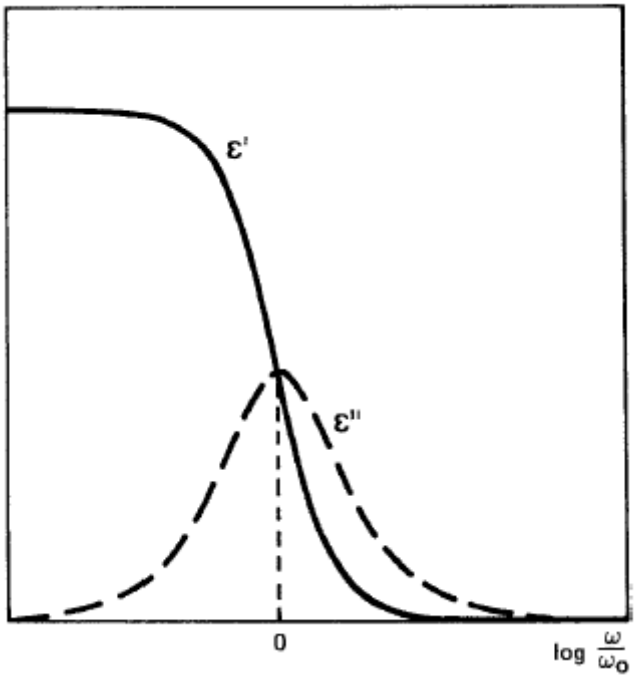

FIGURE 1.14: The real and imaginary part of the permittivity relaxing at the same relaxation frequency[32].

Other models like Maxwell-Wagner, Cole-Cole, Cole-Davidson are the suitable modifications of the Debye model for different practical problems.

1.5.2 Maxwell-Wagner polarization

Many times space charge or interfacial polarization greatly affects the relaxation spectrum. This polarization is caused due to the piling up of space charges in the volume or of surface charges at the interface of the material. The relaxation spectra can be modelled via Maxwell – Wagner condenser by adding the conductivity

contribution to the Debye relaxation as represented in equation 1.16 [33]. The relaxation spectra of a Maxwell-Wagner condenser is shown in fig.1.15.

$$\epsilon^*(\omega) = \epsilon_\infty + \frac{\epsilon_s - \epsilon_\infty}{1 + j\omega\tau} - j\frac{\sigma}{\omega\epsilon_0} \tag{1.16}$$

where $\epsilon_s, \epsilon_\infty$ low and high frequency permittivity. The symbols σ,ω & τ represent the conductivity, angular frequency and relaxation times respectively.

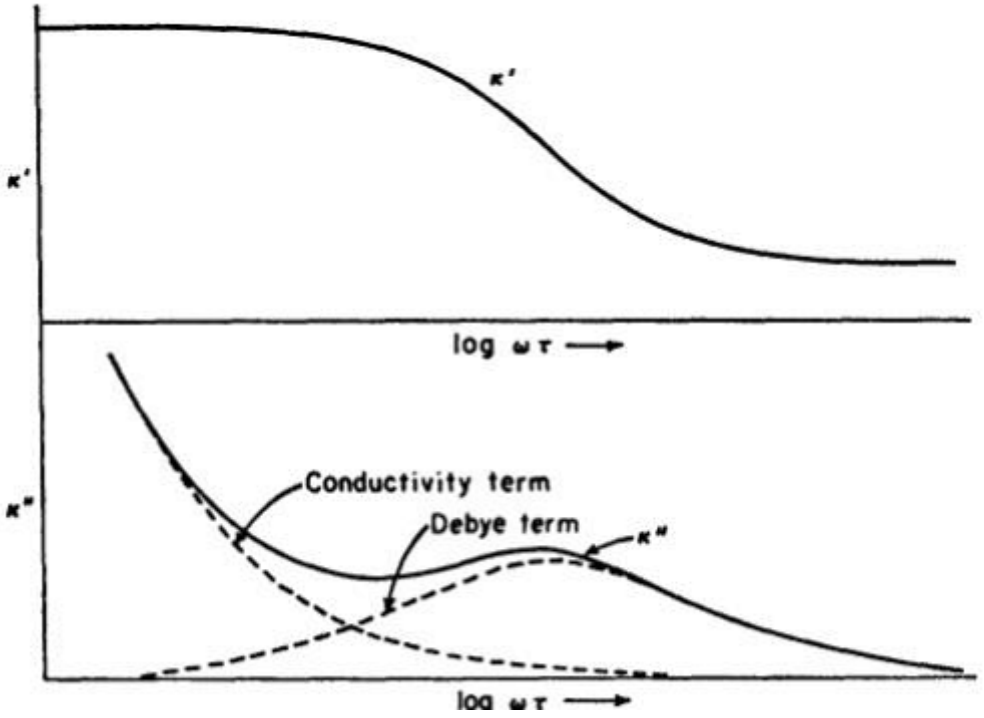

FIGURE 1.15: The relaxation spectra of real part of the permittivity(top), the imaginary part showing the conductivity contribution(bottom) for a Maxwell-Wagner condenser[33].

1.5.3 Harverliak - Negami relaxation

This is the most generalized empirical model representing relaxation processes in a material. Mathematically Harverliak - Negami(HN) equation is the modification of Debye equation by adding two exponential parameters α and β.

$$\epsilon^*(\omega) = \epsilon_\infty + \frac{\epsilon_s - \epsilon_\infty}{[1 + (j\omega\tau)^\alpha]^\beta} \tag{1.17}$$

where $\epsilon_s, \epsilon_\infty$ are the low and high frequency permittivity respectively. Exponents α,β are the asymmetry and broadness parameters of the semicircles respectively. $0 < \alpha < 1$ represents a depressed semicircular arc with its origin below the abscissa. $0 < \beta < 1$ describe a skewed semicircular arc. The variation of the arcs of the semicircles for different values of $0 \leq \alpha, \beta \leq 1$, are given in the fig. 1.16[34]. For

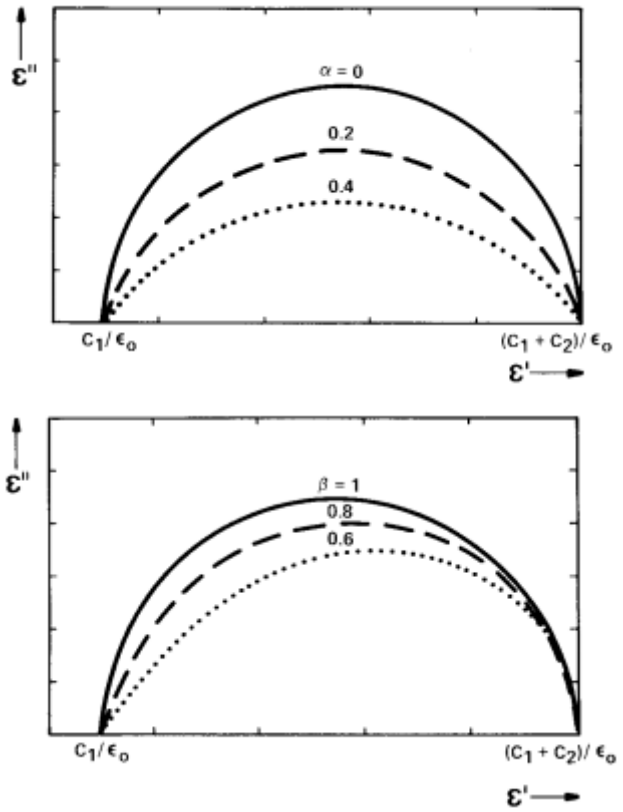

FIGURE 1.16: The variation of the shape of the arcs for different values of α &β[32].

$\beta = 1$ the Havriliak–Negami equation reduces to the Cole–Cole equation. For $\alpha = 1$ the HN equation reduces to Cole-Davidson equation.

1.6 La_2NiMnO_6

Among the family Re_2NiMnO_6 (Re = Rare earth elements), La_2NiMnO_6(LNM) has created a new buzz among the researchers due to the realization of application

oriented properties like near room temperature insulating ferromagnet, magnetodielectricity and magnetoresistance. These properties are realized due to the coupling between electric, magnetic and lattice degrees of freedoms[35]. This makes the material interesting to study it fundamentally as well as for spintronic device applications such as magnetodielectric capacitor, spin based sensors, multiple state memory elements, spin tunnelling junctions etc.

1.6.1 Structural property

As described in the section 1.2, the structure of a double perovskite largely depends on the B – site cationic ordering. Ordering of Mn^{4+} and Ni^{2+} ions in LNM transforms an orthorhombic $Pbnm$ phase to monoclinic $P2_1/n$ phase with angle $\beta = 90^0$[36]. Similarly the same ordering transforms a rhombohedral $R-3c$ to $R-3$ or $R-3m$[36]. The initial report on LNM suggest an orthorhombic crystal symmetry with slight monoclinic distortion for sample synthesized at 1100^0C [37]. The samples synthesized at temperature higher than 1300^0C is crystallized in monoclinic structure [8, 36]. The monoclinic crystal structure (Space group: $P2_1/n$) of LNM is having B – site ordered rock salt arrangement of cations as shown in fig.1.17.

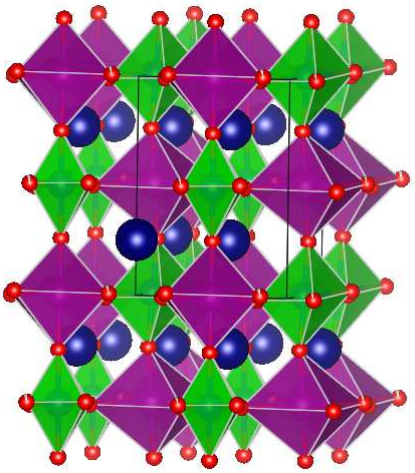

FIGURE 1.17: Crystal structure of monoclinic La_2NiMnO_6.

The monoclinic lattice parameters obtained from neutron diffraction (ND) data are $a = 5.467$Å, $b = 5.510$Å, $c = 7.779$Å and $\beta = 90.12^0$ [38, 39]. Some researchers have also observed the biphasic rhombohedral ($R-3$) and monoclinic ($P2_1/n$) phase for samples synthesized at 1300^0C in O_2 atmosphere[36]. Similar biphasic compositions are also reported by F.N. Sayed *et. al.,* after carrying out exclusive ND measurements[40]. Only orthorhombic phase also been reported by some researchers with lattice parameters $a = 5.501$Å, $b = 5.470$Å and $c = 7.751$Å[41]. Nanoparticles of LNM synthesized at 600^0C are found to biphasic with $R-3c$ and $Pbnm$ phases[42]. Similar biphasic samples are reported by Blasco *et. al.,*, the lattice parameters calculated from ND data are $a = b = 5.5047$Å, $c = 13.2353$Å for $R-3c$ phase and $a = 5.5035$Å, $b = 5.4527$Å, c = 7.7279Å for $Pbnm$ phase[43]. Samples synthesized by glycine – nitrate combustion synthesis are found to contain similar $R-3c$ and $Pbnm$ phases[44].

In LNM, the B-site ions are magnetic in nature and B – site ions play an important role in the stability via tolerance factor. Thus a close correlation of structure and the magnetic property is seen.

1.6.2 Magnetic property

The first principle density functional theory (DFT) calculations based on the full-potential linearized augmented plane wave (FP-LAPW) method has verified a ground state ferromagnetic insulating property of LNM [45]. The band gap of LNM was calculated to be $\sim$ 1eV signify the semiconducting nature of LNM. The spin polarized calculations have verified the experimentally observed magnetic moment of $5\mu_B$ per formula unit. The magnetic moment value satisfies the conditions for the Hund's first rule moments $Mn^{4+}(3d^3)$:$t_{2g}^3e_g^0$ and $Ni^{2+}(d^8)$:$t_{2g}^6e_g^2$. This result also confirms the prediction of Goodenough–Kanamori (GK) rule that the coupling between the adjacent Mn^{4+} and Ni^{2+} ions are ferromagnetic in nature. Similar first principle calculations on thin film structures have predicted the ferromagnetic half metallic nature of LNM [38]. The calculated magnetic moment value $4.7\mu_B$/f.u is very close to the bulk magnetic moment.

The ferromagnetic (FM) ordering due to superexchange interaction $Ni^{2+} - O^{2-} - Mn^{4+}$ is realized below transition temperature ($T_C \sim 280$K) [8]. The magnetic transition is of second order nature based on the calculations from Landau's theory [46]. The FM T_C very close to room temperature, makes it a promising candidate for spintronics applications. The B – site highly ordered sample also have antiphase boundaries [36]. The antiphase boundary couples the adjacent FM domains antiferromagnetically at zero field but a modest applied field able to rotate the FM domains with a 360^0 spin rotation across the antiphase boundaries giving rise to small remnance in the hysteresis loop [36].

The antisite disorder induced couplings $Ni^{2+} - O^{2-} - Ni^{2+}$ and $Mn^{4+} - O^{2-} - Mn^{4+}$ introduce antiferromagnetic (AFM) components in LNM hence the saturation magnetization deviates from theoretically calculated magnetic moment $5\mu_B$/f.u [47]. The saturation magnetization and FM T_C also reduced in decreasing the particle size[41, 48]. The nanometric size hinders the long range ordering and hence decreases the T_C and saturation magnetization.

Sometimes another magnetic transition is seen at low temperature especially for biphasic sample. The low temperature FM T_C at ~ 150K is due to the ordering of *Pbnm* phase because of superexchange interaction $Ni^{3+} - O^{2-} - Mn^{3+}$ [44].

Low temperature spin glass behaviour is also reported [8, 42]. The spin glass transition temperature is around ~ 40K as seen in the temperature dependent magnetization data[8].

Short range ordering of small FM clusters before the actual arrival of T_C is reported by Iliev *et. al.,* [49], and S. Zhou *et. al.,* [50]. Similar short range ordering and Griffiths phase like behaviour is observed in another prototype of the family Tb_2NiMnO_6[21]. So Griffiths like phase may be expected in LNM.

1.6.3 Dielectric and Magnetodielectric property

The room temperature permittivity (ϵ_r) value is of the order of $\sim 10^3$ (see fig. 1.18a). Both intrinsic and extrinsic effect contribute to ϵ_r [8]. The extrinsic or

Maxwell – Wagner contribution comes from the grain boundaries and interfaces[8]. Relaxor like dielectric behaviour is reported by Y.Q lin *et. al.*,[51]. The relaxor ferroelectric behaviour also reported by M. G. Masud *et. al.*,[41] and they found a lossy elliptical hysteresis $P \sim E$ loop at 100K. Glassy dielectric behaviour is also reported by D Choudhury *et. al.*,[8].

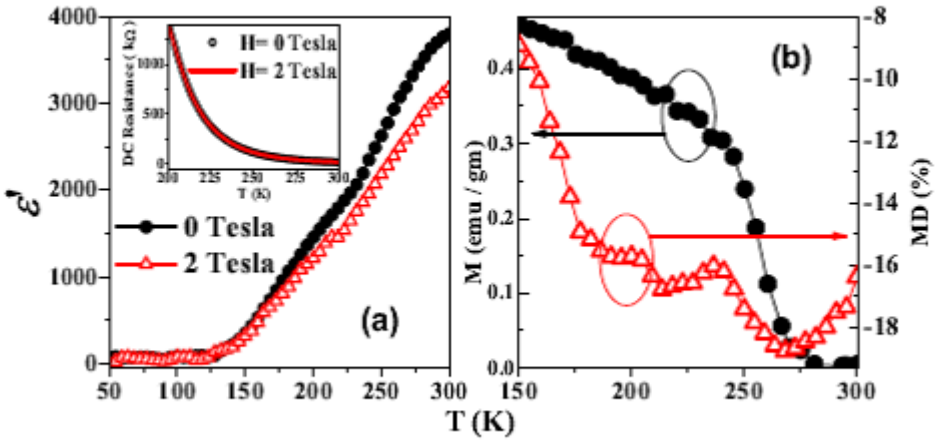

FIGURE 1.18: a. Change in $\epsilon^{'}$ induced due to application of magnetic field of 2T. b. Temperature dependent MD, a strong correlation of MD with magnetic order is seen[8].

The applied magnetic field induces large change in $\epsilon^{'}$ (see fig.1.18.a). About 18% magnetodielctricity (MD) is observed at 2T magnetic field for partially disordered LNM [8]. Around 15% MD reported at 0.1T for biphasic LNM [10]. The applied magnetic field increases the spin - spin correlation below FM T_C[8]. So the spin dependent asymmetric hopping is the cause of induced intrinsic MD. Above the FM T_C = 280K, the spin correlation breaks and due to thermal disorder there is decrease in MD value.

Extrinsic contribution to MD is also reported in bulk [52] and nanoparticles of LNM [42]. The obtained MD percentage remained around 5%. MD is also observed in the sample in thin film form [53, 54]. However the maximum MD percentage is reported to be 6% for the B – site ordered film.

1.6.4 DC Resistivity and Magnetoresistance

As discussed earlier LNM exhibits a band gap $\sim$ 1eV, so it is semiconducting which is further confirmed from the temperature dependent resistivity data. Unlike other manganites the temperature dependent resistivity data of LNM don't show any anomaly across the magnetic transitions. Various conduction mechanisms like thermally activated conduction [55], variable range hopping (VRH) [41], small polaron hopping (SPH) [41] and Schnakenberg's polaronic conduction[42] are proposed to understand the mechanism of conduction.

At 200K a 3% decrease in resistance is observed at 1T magnetic field for biphasic LNM[10]. Similarly, a 4% -ve magnetoresistance (MR) at 5T is observed for LNM nanoparticles[42]. The isothermal MR at 250K show spin polarized tunnelling (SPT) of charge carriers at low fields and at high fields the MR contribution comes from the Zener Double exchange mechanism inside each grain [42]. Near room temperature TMR behaviour is observed in LNM, where 11% -ve MR in 5T magnetic field at temperature 250K is reported [56].

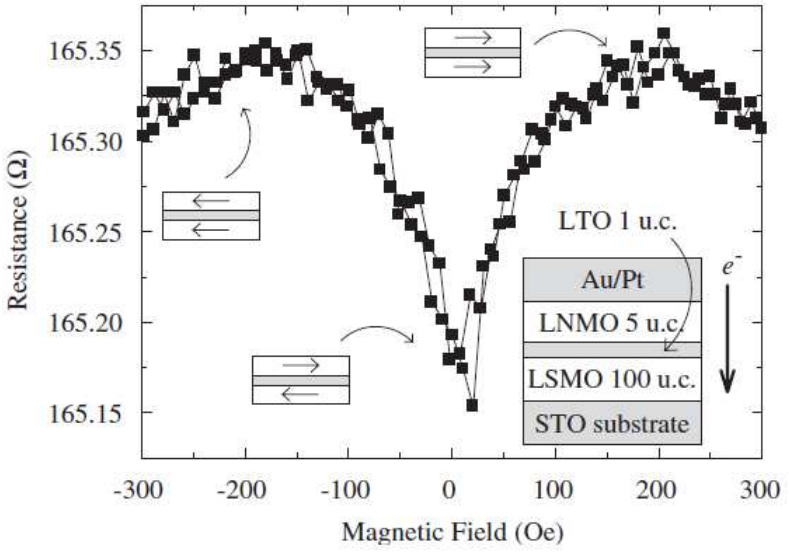

FIGURE 1.19: Spin filtering effect in hetero junctions LNM/$LaTiO_3$/$La_{0.7}Sr_{0.3}MnO_3$ in $SrTiO_3$ substrate[57].

The antisite disorders in LNM, integrate into antiphase boundaries separating FM domains. The TMR behaviour is manifested due to the tunnelling of electrons through these antiphase boundaries[56]. The spin filtering effect of LNM is realized at 150K in hetero-junctions LNM/$LaTiO_3$/$La_{0.7}Sr_{0.3}MnO_3$ in $SrTiO_3$ substrate for device applications as per fig.1.19[57]. The nonmagnetic $LaTiO_3$ layer is sandwiched between the two magnetic layers. So the MR behaviour is highly dependent on the spin alignments of the magnetic LNM and $La_{0.7}Sr_{0.3}MnO_3$ layers.

1.6.5 Effect of chemical substitution

Substitution of other lanthanide elements at La - site show decrease in unit cell volume due to smaller ionic radii[58]. There is also decrease in FM T_C from 287K to 40K as one moves from La to Lu in the series[47, 58, 59]. However the resistivity value increases from 541Ωcm (for La) to 1806Ωcm(for Gd) with increase in band gap from 0.9eV to 1.4eV. Decrease in FM T_C to a value 79K is observed for Y - substitution[47]. Band-structure calculations by *ab initio* method predicts the half metallic nature with insulator to metal transition on Sr - substitution[60, 61]. Exchange bias effect with increased antisite disorder is also observed for Sr - substituted LNM[62]. The Ca - substituted LNM show monotonic decrease in FM T_C and saturation magnetization with increase in Ca content[63]. The partial substitution of K at La - site, increase the catalytic activity of LNM[64]. In $La_2Ni(Mn_{1-x}Ti_x)O_6$, partial substitution of Ti decrease the FM T_C and spontaneous magnetization[65]. Other report of B -site substituted compound viz. La_2MgMnO_6, show relaxor like dielectric response with Debye type dielectric relaxation[66].

1.7 Motivations

La_2NiMnO_6(LNM) is truly multifunctional due to its exotic properties such as magnetodielectricity and magnetoresistance. The multiple structures, multiple magnetic transitions and multiple magnetic states makes it an interesting candidate for fundamental study.

1. Two Phase systems like composites and epitaxial multilayers show enhanced magnetoelectric effect than the parent single phase systems[67, 68]. The enhanced magnetoelectric effect is due to indirect magnetoelectric coupling via strain. Hence due to lattice parameter mismatch between crystallographic phases in biphasic LNM the strain is intrinsic to the system. So magnetoelectric response of biphasic LNM will be interesting and worth for investigation.

2. Recently, in a study by D. Chaudhari *et. al.,* considerable magnetodielectricity was observed in temperature $150 - 250$K. Incidentally, this region marks the ordering of ferromagnetic $R-3c$ phase in the background of paramagnetic $Pbnm$ phase, in the biphasic LNM. This is an indication of possible coupling between dielectricity to the magnetic states of the compound, thus a possibility of magnetoelectric coupling.

3. The $R-3c$ phase is dominated by $Ni^{2+} - O^{2-} - Mn^{4+}$, super-exchange interactions and the $Pbnm$ due to $Ni^{3+} - O^{2-} - Mn^{3+}$. Thus a substitution by divalent element is expected to stabilize the $R-3c$ phase and substitution of trivalent, to the $Pbnm$ phase. Thus via substitution, the relative compositions of the two phases can be tailored. Since the $R-3c$ phase is more technologically important due to its magnetic ordering near to room temperature, we intended to increase the $R-3c$ phase content in the sample. Owing to similar ionic radii of Cu^{2+}(73pm) to that of Ni^{2+}(70pm), partial substitution by Cu^{2+} is expected to solve the purpose.

4. $CoFe_2O_4$ (CFO) is a well-known near-room-temperature magnetostriction compound. Insertion of CFO in the voids of LNM pellet may lead to a

third junction apart from that due to the two respective phases of LNM. Since multiphase materials are better magnetoelectrics due to stress at the junctions, utilizing the magnetostriction of CFO, we intend to achieve high value magnetoelectricity.

5. LNM is well known for its splendid possible applications making it a true multifunctional material. Large surface compared to volume in nano-form of LNM opens the door for another possible application such a gas sensor. So gas sensing ability of LNM is investigated in various gaseous environments like argon, oxygen and nitrogen.

Chapter 2

Sample Preparations and Characterizations

2.1 Synthesis

The structural and compositional aspect of La_2NiMnO_6(LNM) are very sensitive to the synthesis conditions. Different polymorphs of LNM such as orthorhombic, rhombohedral and monoclinic are coexistent for different ranges of temperatures. Ordering of $B^{'}$ & $B^{''}$ atoms inside the unit cell is determinant of magnetic, dielectric eventually magnetodielectric properties. Apart from that, the oxygen stoichiometry is very much dependent on the synthesis condition. Thus the synthesis must be chosen carefully, to tune the B - site ordering. Plentiful reports on both solid state and liquid phase methods for the preparation of LNM have been proposed. The following sections highlights a few of them.

2.2 Literature Reviews on Synthesis of La_2NiMnO_6

2.2.1 Solid State Method

To the best of our knowledge, the first report on the preparation of LNM goes back to 1958, where A. Wold *et. al.,*[37] prepared a series of solid solution of $LaMnO_3$ - $LaNiO_3$. They took the oxide precursors of the respective metals and heat treated the mixture in different gaseous atmospheres. Three important observations were made

1. The composition $LaNi_{0.5}Mn_{0.5}O_3$ crystallized in orthorhombic crystal structure with a slight distortion towards the monoclinic structure.

2. The lattice symmetry of the solid solution changes from orthorhombic to rhombohedral when the concentration of Mn^{4+} ions exceeds 21%.

3. Commenting on oxygen stoichiometry; they attributed the excess oxygen to the Mn^{4+} ions and oxygen deficiency to Ni^{2+} ions.

Other reports on solid state method of preparation are Y.Q. Lin *et. al.,*[51] & X. Yuan *et. al.,*[69] where the stoichiometric constituent oxides are properly ground. After grinding, the powder is heat treated for multiple times at higher temperature to undergo the physical diffusion of constituent atoms. Both the groups observed that the sample is crystallized in monoclinic structure with the space group $P2_1/n$. Though X. Yuan *et. al.,* obtained the monoclinic structure but they also inferred some anti-site disorder of B – site atoms. However Y.Q. Lin *et. al.,* claimed to obtain a perfect B – site ordered structure following calcination in air at 1473K for 3hrs and sintering it at 1723K for 3hrs.

2.2.2 Wet Chemical Method

Apart from solid state synthesis, ample reports are available on the synthesis via wet chemical method. This method is based on the bottom up approach of material synthesis where the individual atoms/ions coalesce to form the compound.

R.I. Dass *et. al.,* used the wet chemical method for the synthesis of LNM[36]. In their well described detailed report, they followed Pechini method [70] of synthesis. Stoichiometric amounts of constituent nitrates and acetates were used as precursors. These salts were dissolved in de – ionized water, with few drops of nitric acids to dissolve the acetate. The emerald green solution was mixed with 1.5 times amount by weight of citric acid and few drops of ethylene glycol. The solution then heated at approximately 150°C to undergo polysterification as well as removal of excess water. The obtained gel was dried and decomposed at 375°C for 24hrs. The so obtained dark brown powder was calcined at various temperatures and different gaseous atmospheres. The series of samples obtained were oxygen excessive. The sample heated at 1350°C for 6hrs in Ar – atmosphere was found to be composed of single phase (space group = $P2_1/n$). Samples synthesized at 600°C and 725°C in air were also single phase but having different structure (space group = $R-3$). The samples synthesized at 1100°C were biphasic (space group = $P2_1/n + R-3$).

J. Blasco *et. al.,* followed a similar process but they assigned the structures to different space groups ($R-3c$ & $Pbnm$)[43]. The biphasic nature was persistent for samples heat treated under different atmosphere(Argon, Air, Nitrogen, Oxygen).

Another method of preparation under the category of wet chemical method is glycine – nitrate combustion synthesis[71]. This method is specialized for the preparation of oxide or ceramic powders. In this method, the metal nitrates added with glycine are dissolved in distilled water and heated continuously until the solution is ignited and burn vigorously to form the required ceramic powdery ash. Joly *et. al.,*[44] used the glycine – nitrate combustion method for the preparation of LNM. They heat treated the sample at different temperatures and drew the

following conclusions. Glycine nitrate method of preparing LNM result biphasic samples, with varying degree of $Pbnm$ and $R-3c$ depending on the sintering temperature. For T > 1300°C, purely $R-3c$ phase and for T < 400°C purely $Pbnm$ phase and 400°C < T < 1300°C, both phases coexists. F. N. Sayed *et. al.*,[40] used a similar glycine – nitrate method for the preparation and obtained the biphasic sample.

2.3 Synthesis of $La_2Ni_{1-x}Cu_xMnO_6$, $x = 0, 0.05 \,\&\, 0.1$.

Polycrystalline LNM sample is prepared by glycine – nitrate combustion synthesis technique. $La(NO_3)_3.6H_2O$, $Ni(NO_3)_3.6H_2O$, $Mn(NO_3)_2.4H_2O$ and $Cu(NO_3)_2.3H_2O$ are taken as precursors and glycine as the fuel. In this synthesis, fuel to metal nitrates ratio is maintained at 1:1. Stoichiometric amounts of metal nitrates and glycine are dissolved in the distilled water to form an emerald green solution. The solution is continuously stirred and slowly heated till the gel formation. After gelation, the solution is further heated at 150°C on a hot plate to undergo combustion forming black powder.The desired powder is ground properly and pressed into pellet of 10mm diameter and ∼ 1mm thickness. The pressed pellets are sintered at a temperature 1000°C for 12 h in a muffle furnace. Fig.2.1 represents the flowchart of the synthesis procedure followed.

2.4 Synthesis of $CoFe_2O_4$ impregnated La_2NiMnO_6 Nano composite

We have used a novel method for synthesizing $CoFe_2O_4$ (CFO) impregnated LNM composites. Stoichiometric amount of $Co(NO_3)_3.6H_2O$ and $Fe(NO_3)_3.9H_2O$ are dissolved in 100ml of distilled water in a glass beaker. The solution is continuously stirred and heated until 90% of the water is evaporated. Pellets of LNM prepared via sol-gel auto-combustion method, are modified via impregnation in the acidic

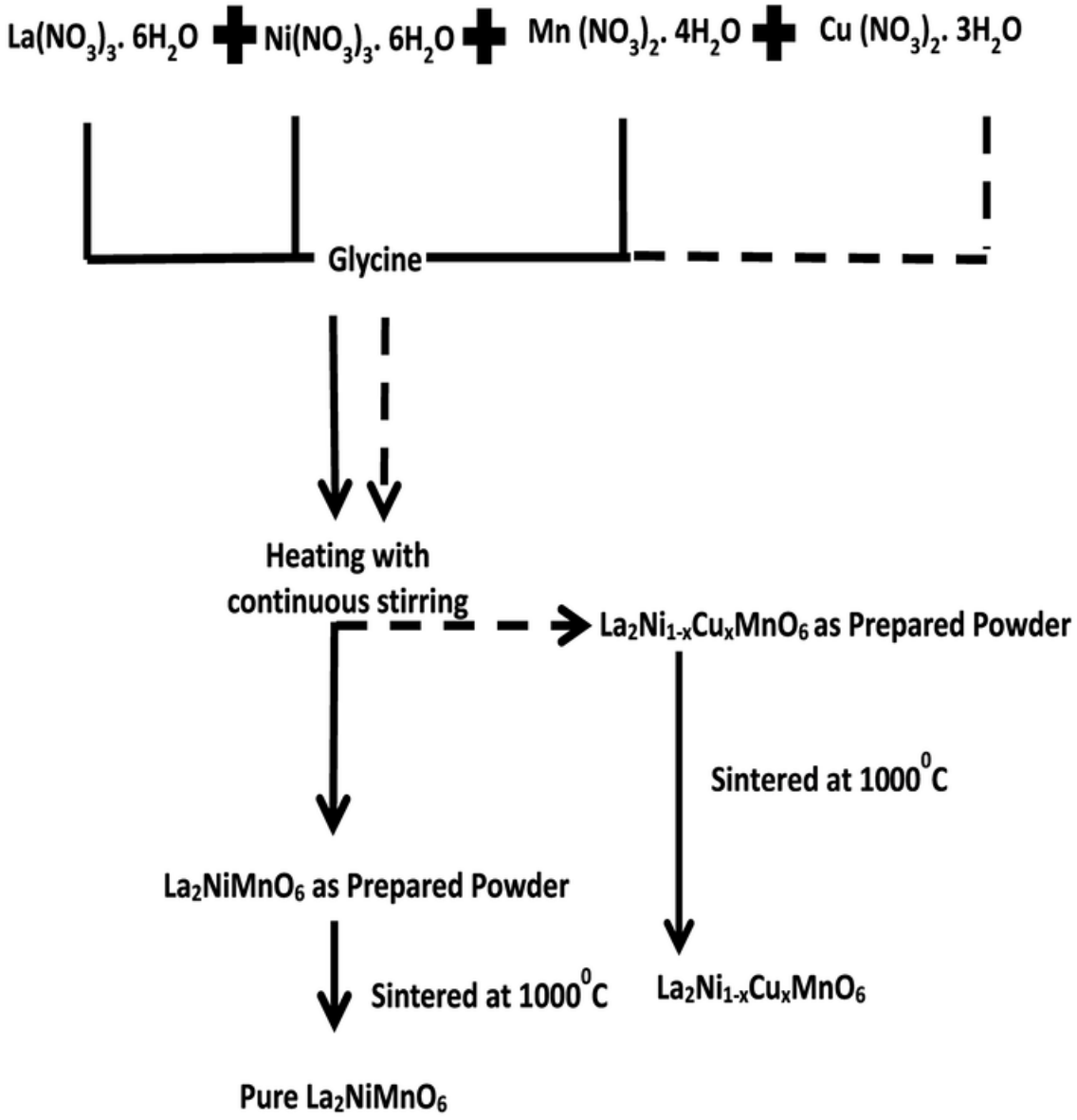

FIGURE 2.1: Sample Synthesis Flow chart.

(pH = 0.1) aqueous solution. The beaker containing the LNM pellets in aqueous solution is placed inside a desiccator and evacuated for 3hrs. The evacuation sucked the air molecules out of the pores, which is further filled by the aqueous solution. After taking out from the solution, the excess solvent over the pellet is wiped-off and the pellet is kept in an oven at 100^0C for drying. The dried pellet is then heat treated at 600^0C for 1hr to obtain the required modified-LNM or M-LNM.

2.5 Characterizations

2.5.1 X -Ray Diffraction and Rietveld Refinement

Some of the sintered pellets are crushed and powdered for x-ray diffraction (XRD) measurement in Bruker D8 Advance X-ray diffractometer. The XRD measurement is carried out in the 2-theta range of $20° - 80°$. The data so obtained are refined via Rietveld method using FullProf program to explore the structural details. The Rietveld refinement reveals biphasic nature, i.e., coexistence of rhombohedral $R-3c$ $[a = b = 0.550149(6)$ and $c = 1.3228(2)$ (in nm)] and orthorhombic $Pbnm$ $[a = 0.54995(1), b = 0.54508(1)$ and $c = 0.773214(3)$ (in nm)] phases of LNM sample (fig.2.2 top panel). The volume percentage of rhombohedral and orthorhombic phases in LNM is found to be 71% and 29%, respectively. The biphasic ($R-3c+Pbnm$) nature of LNM is found to persist in Cu substituted samples $La_2Ni_{1-x}Cu_xMnO_6$: x = 0.05 and x = 0.1 as well (fig.2.2 middle & bottom panels). On increasing Cu substitution, the $R-3c$ phase is found to be increasing: $71\%(x = 0)$, $74\%(x = 0.05)$ and $76\%(x = 0.1)$. Both the crystallographic phases show negligible volume change due to Cu substitution, probably due to very close values of ionic radius. The structural parameters are listed in table.2.1.

	x = 0	x = 0.05	x = 0.1	M - LNM
% $R-3c$ phase	71	74	76	31
$R-3c$ phase volume in $Å^3$	347.00(3)	346.45(2)	346.20(4)	346.98(7)
a in nm	0.550149(6)	0.54969(4)	0.54961(3)	0.54995(6)
c in nm	1.3228(2)	1.3240(8)	1.3233(1)	1.3247(1)
% $Pbnm$ phase	29	26	24	69
$Pbnm$ phase volume in $Å^3$	231.45(2)	231.30(2)	231.17(9)	233.90(5)
a in nm	0.54995(1)	0.54893(2)	0.54889(1)	0.55073(8)
b in nm	0.54508(1)	0.54577(2)	0.54608(9)	0.54697(6)
c in nm	0.773214(3)	0.77206(6)	0.771225(8)	0.77646(9)

TABLE 2.1: Structural parameters for x = 0, 0.05, 0.1 & M - LNM

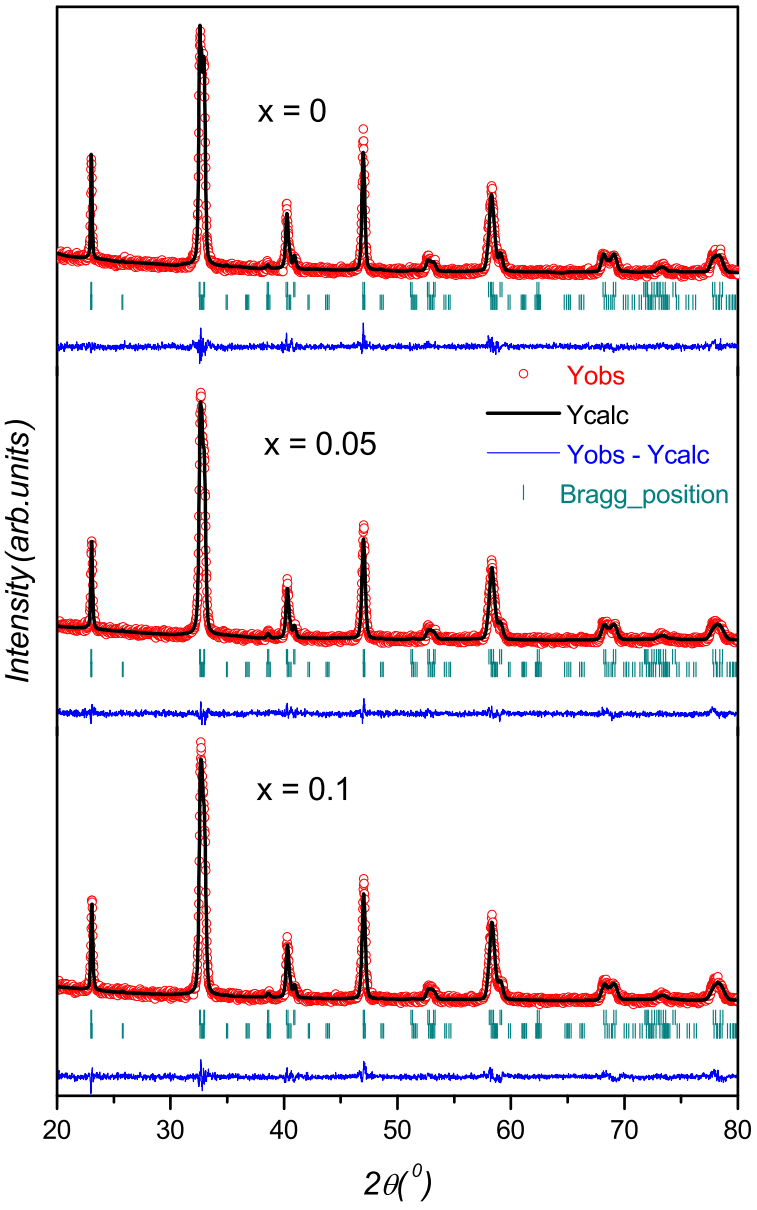

FIGURE 2.2: Rietveld refined x – ray diffraction data for $La_2Ni_{1-x}Cu_xMnO_6$: x = 0, 0.05 & 0.1.

The Rietveld refinement of x-ray diffraction (xrd) data for M - LNM is shown in fig.2.3. The biphasic nature of the sample also persists for M - LNM. The coexisting $R-3c$ and *Pbnm* phases share a volume fraction of 31% and 69% respectively whereas in LNM they were found to be 71% and 29% respectively [55] . Thus in M-LNM, the *Pbnm* phase fraction shows a substantial enhancement from 29% to 69% and consequent reduction in the $R-3c$ phase. The key to sudden rise of *Pbnm* phase lies in the modification process followed. While impregnating LNM,

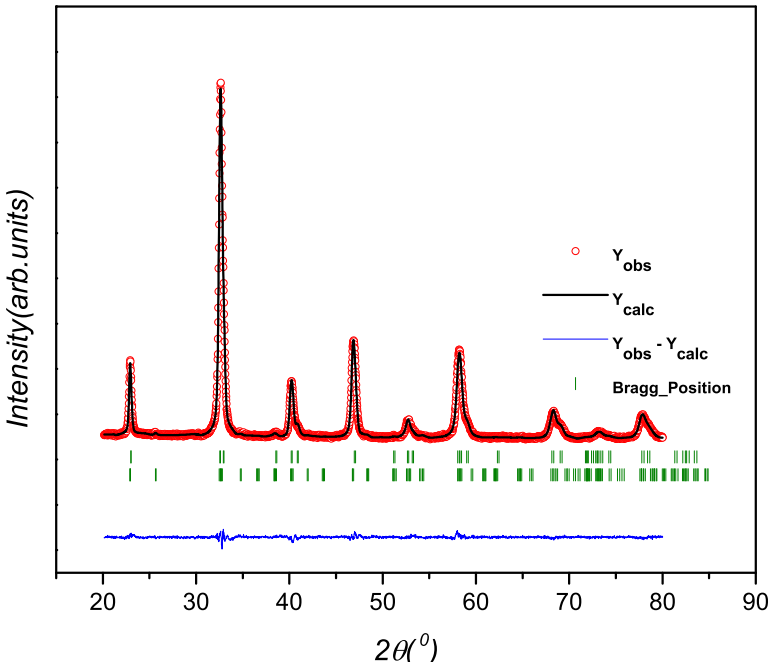

FIGURE 2.3: Rietveld refined x – ray diffraction data for M - LNM.

the acidic (pH $\sim$ 0.1) solvent which got soaked in the pores, etched the surface of LNM. While drying at 100°C, all the solvent got evaporated leaving behind the precipitated disordered LNM, which on sintering at 600°C recrystallized into *Pbnm* phase. The $R-3c$ lattice parameters are found to be a = 0.54995(6)nm c = 1.3247(1)nm and the *Pbnm* lattice parameters are a = 0.55073(8)nm, b = 0.54697(6)nm, c = 0.77646(9)nm are listed in table.2.1.

2.5.2 Low Temperature Impedance Measurement using Lock – In Amplifier

Low temperature environment is facilitated by Janis make Closed Cycle Refrigerator(CCR), with a specially designed home-made feed-through and sample holder for a.c measurement. The feed through consists of a hollow Teflon cylinder with one end closed. Three BNC connectors are fixed on the Teflon cylinder and made air tight by areldite. Coaxial cables are used to draw the electrical connections. The sample holder is a copper disc of 15mm diameter and 2mm thickness. The sample holder is mounted on the cold head of CCR, with thin mica sheet placed

in between. A cernox sensor is placed near to the sample for accurate temperature measurement. A snapshot of impedance measurement with zoomed view of special feed through is given in Fig.2.4. For magnetoimpedance measurement the outer shroud of the CCR is specially designed to fit into the 20mm pole gap of the electromagnet. The electromagnet is of GMW model 5403 make, provided with Kepco BOP $25-40$MG bipolar power supply. So an external magnetic field upto 1.2T is achievable with 20mm pole gap. The electromagnet is tilted 90° and placed on the top of a indigenously designed movable stand. The picture of the magnetoimpedance measurement is given in fig.2.5.

FIGURE 2.4: Snapshot of impedance measurement. The arrow signifies the zoomed feed- through region.

Impedance measurement in the frequency range 100Hz – 100kHz is done using Lock - In Amplifier(LIA). The SR 830 model LIA of Stanford Research System is used for impedance measurement. SR 830 LIA is known for its sensitivity down to nano-volts. It is based on the technique of phase sensitive detection by which

FIGURE 2.5: Snapshot of modified CCR shroud with in the pole piece of the electromagnet for magneto - electrical characterizations.

in-phase and out-of-phase components of signal are singled out from the noise at a specific reference frequency and phase. Detection of signals at higher order harmonics is also possible through LIA.

Impedance is measured by a method called vector ratio detection (VRD) method. In this method the vector voltages are measured across the sample and a series resistor. Fig.2.6 depicts the adopted measurement circuit in which R represents the series resistor and DUT(X) represents the sample. The VRD consists of a relay, and LIA. A sinusoidal voltage of 0.5V from sine out of LIA is applied to the sample and resistor in series. Voltage drop across the sample and the resistor is fed to the differential input of LIA. A relay is added to the circuit for alternate switching of the differential input to the LIA. The sequential data acquisition is made by programming the LIA & Lakeshore 331 temperature controller through Labview 2010 software. Fig.2.7 represents the programmed user interface window for on -line data acquisition.

Mathematically, voltage drop across the sample can be represented in the vector format $V_x = a + ib$ & voltage drop across the resistor can be represented by

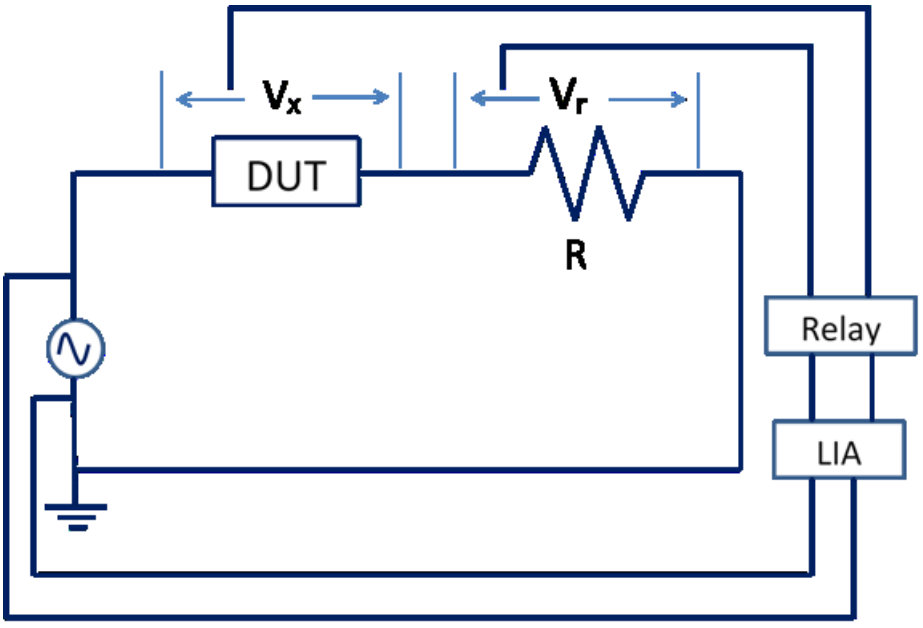

FIGURE 2.6: Circuit diagram for VRD impedance measurement method.

$V_r = c + id$. By using simple mathematical formalism the complex impedance of the sample(Z^*) can be calculated as.

$$Z^* = Z^{'} + jZ^{''} = R\Big[\frac{ac+bd}{c^2+d^2} + j\frac{bc-ad}{c^2+d^2}\Big] \tag{2.1}$$

where R represents the resistance of the series resistor. The real part $Z^{'}$ is the resistance and imaginary part $Z^{''}$ represents the reactance. The dielectric (ε^*), conductivity(σ^*) and modulus(M^*) parameters can be calculated by simple conversion formulas as describe in section 1.5 of chapter 1.

2.5.3 Gas Sensing by Impedance measurement

Sample is mounted on the cold head of CCR, where in addition to temperature variation; the sample chamber may be purged by various gases at different pressures. The measurement is done at various stable temperatures from 300K to 350K. A bladder filled with 99.9% pure Argon/Nitrogen/Oxygen gases is connected to the vacuum couplings of CCR. A fixed volume of gas is purged to the chamber by

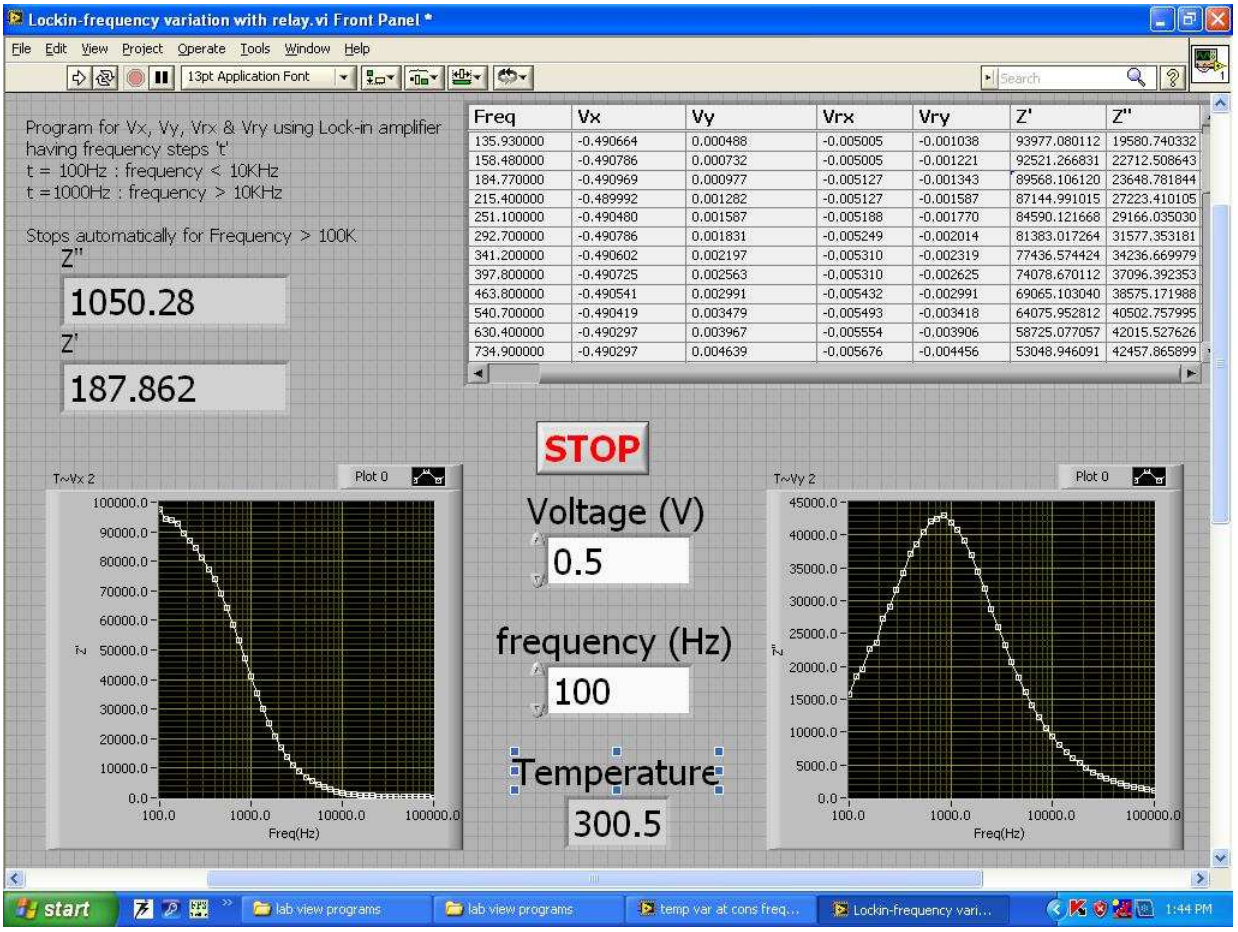

FIGURE 2.7: Snapshot of Labview Program for impedance data acquisition .

controlling through two stage valves. After the gas is purged, the sample is left for a waiting period of 15mins before each measurement. This is done for homogenization of adsorption process before the measurement. The pressure of various gases inside the chamber is calculated by simple conversion using Boyle's law.

2.5.4 Low Temperature Transport Property and Magnetoresistance Measurement

Low temperature bulk resistivity and magnetoresistance measurement is done in the CCR equipped with Keithley 6517B electrometer. Without disturbing the sample, resistivity is measured in the same capacitor configuration as for impedance measurement. Magnetic field is provided by the electromagnet externally as shown in fig.2.5. The sequential measurements are also programmed through Labview

2010 software (see AppendixA). I $\sim$ V characteristics is done at stable temperatures by standard four probe method with Keithley 6221 Current Source and Keithley 2182A nanovoltmeter programmed through Labview.

2.5.5 Magnetization Measurement

Magnetization measurement is done in Quantum Design make PPMS Variable Sample Magnetometer(VSM). The zero field cooled (ZFC) data and Field Cooled warming(FC) data is collected at magnetic fields 0.01T, 0.1T & 1T. The isothermal magnetization data at different temperatures is collected in the magnetic field range $\pm$9T. The dynamics of magnetic moments is measured by switching off the applied field and measuring the magnetization w.r.t. time.

2.5.6 Field Emission Scanning Electron Microscopy (FE-SEM) Measurement

The surface morphology of some of the samples are observed through electron microscope by Nova Nano SEM. This FESEM has the resolution upto 1.4nm at 1kV. So morphology and the size of nanoparticles can be easily identified. The gold coated pellets are analysed at several resolutions and some selective images for LNM and M - LNM samples are shown in the fig. 2.8.

The morphology of LNM (fig.2.8 top panel) shows its nano porous nature with grain size 30nm. The morphology of M-LNM (fig.2.8 bottom panel) sample is almost similar to LNM, except the grains are homogeneously spread and less fused. The grain size remains same.

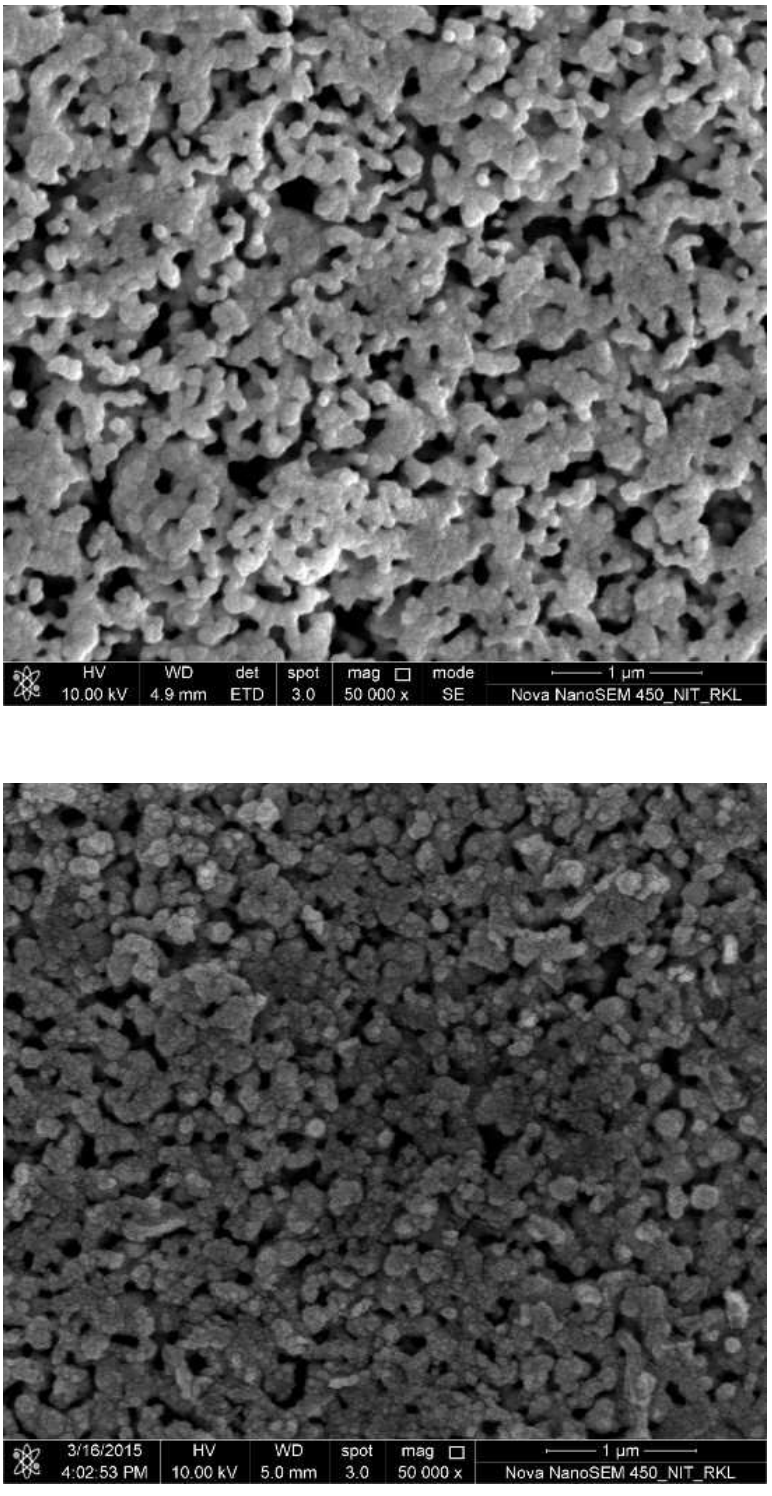

FIGURE 2.8: FESEM micrographs for LNM(top), M-LNM (bottom).

Chapter 3

Dielectric relaxations in La_2NiMnO_6 with signatures of Griffiths phase

3.1 Introduction

LNM is a ferromagnetic insulator having $T_C \sim 280K$[36]. The ferromagnetic ordering originates due to superexchange interactions between ordered Ni^{2+} and Mn^{4+} ions[72, 73]. The Mn-O-Ni superexchange interaction has been found to be very stable against external pressure, at least up to 38 GPa[74]. Hence, any effect having its origin in the coupling between charge, spin and lattice degrees of freedom[49, 75, 76] may have giant implications such as giant magnetodielectricity, giant magnetoresistance, etc. This makes the material technologically very important.

Sometimes signature of another magnetic transition at lower temperature $T \sim 150K$ has also been observed[8, 44, 69]. In LNM, epitaxial films prepared via

J. Appl. Phys. **115**, 194106 (2014).

pulsed laser deposition technique, this low temperature transition has been attributed to the disordered phase[77]. By another group, the low temperature transition in single phase LNM prepared via Pechini method is attributed to anti-site defects leading to ferromagnetic - spin glass transition[8]. The low temperature transitions in LNM prepared via solid state reaction method have been ascribed to the FM interactions related to the Ni^{3+} and Mn^{4+} Jahn-Teller ions[69]. In samples synthesized by low temperature glycine-nitrate method, the high temperature ($\sim$ 280K) transition is attributed to ferromagnetic T_C corresponding to $R-3c$ (rhombohedral) phase and low temperature ($\sim$ 150K) one as the ferromagnetic T_C to *Pbnm* (orthorhombic) phase[43, 44]. Interestingly, nano crystalline LNM with orthorhombic symmetry (*Pbnm*) shows only one magnetic transition around $T \sim 200$ [41, 48]. Relaxor[51] like ferroelectricity and multiferroic behaviour is also reported for nanoparticles of LNM[41]. However, the possibility of relaxor behaviour is completely ruled out by Chandrasekhar *et. al.,* [52].

Two Phase systems like composites[67] and epitaxial multilayers[68] have shown enhanced magnetoelectric effect than the parent single phase systems. The enhanced magnetoelectric effect is due to indirect magnetoelectric coupling via strain between the two phases. LNM is one system which can be tailored to single or biphasic on tuning the synthesis process and hence seems to be a viable candidate for investigation. Before that, the various phases (magnetic and crystallographic) and their implications on the system must be analysed in detail. That is why, in spite of several reports of low temperature magnetic transition and dielectric relaxations, the LNM is re-investigated. In the present study, signature of Griffith phase is seen in the magnetization data and strong correlation between the relaxation processes with the magnetic phases have been found.

3.2 Results and Discussion

3.2.1 Impedance Study

The sample is analysed via A.C. and D.C. electrical transport and corroborated with magnetization measurements. In A.C. technique, the electrical response of a material to the applied A.C. electric field can be represented by different complex formalisms like impedance (Z^*), dielectric (ε^*), modulus($M^* = j\omega C_0 Z^* = (\epsilon^*)^{-1}$) and conductivity ($\sigma^* = j\omega\epsilon_0\epsilon^* = ((A/d)Z^*)^{-1}$). Complex impedance spectroscopy is a powerful technique for characterizing materials as various relaxation components may be separated out. One of the efficient ways of distinguishing various relaxation mechanisms is via Nyquist plot or Cole-Cole plot, where each relaxation mechanism contributes a semicircular arc. The real ($Z^{'}$) and imaginary ($Z^{''}$) components of the impedance at various temperatures are plotted as Nyquist plot in the complex plane (fig.3.1, 3.2).

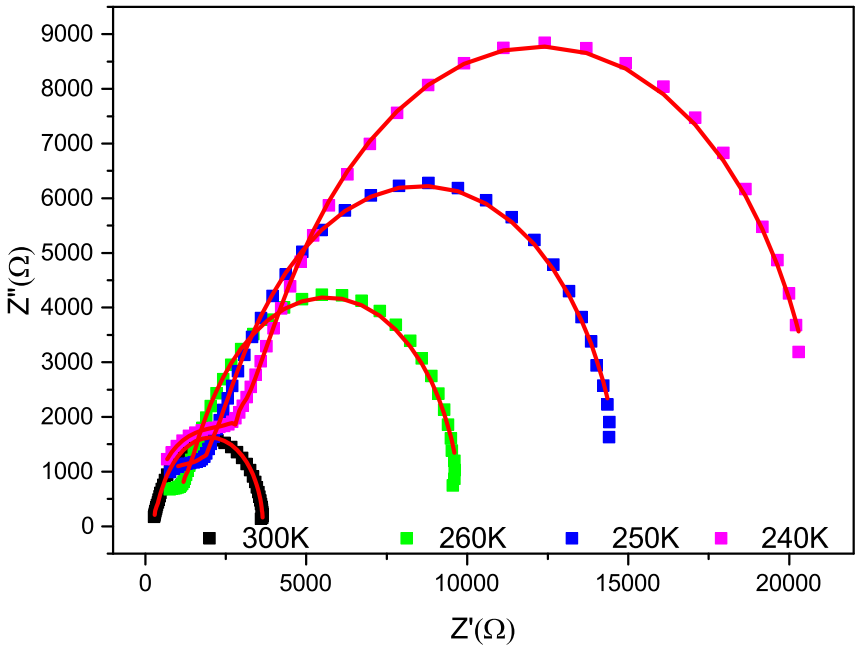

FIGURE 3.1: Cole-Cole plot of impedance data fitted with respect to Eq. (3.3). The solid lines stand for fitting.

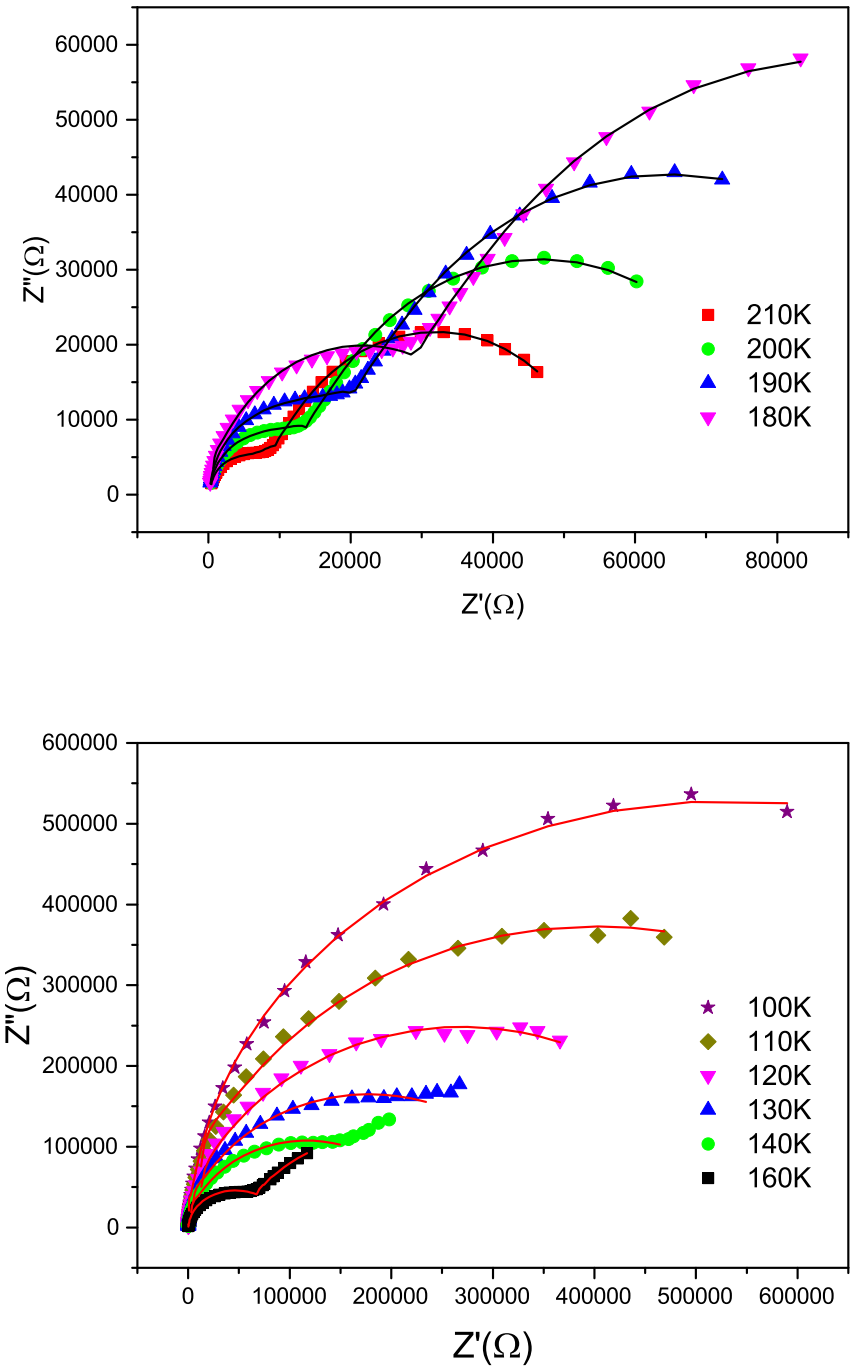

FIGURE 3.2: Cole-Cole plot of impedance data fitted with respect to Eq. (3.3). The solid lines stand for fitting.

At 300K, a single semicircle is obtained. As the temperature is lowered, near T $\sim$ 280K a tail appears on the high frequency side. On further lowering of

temperature, this tail grows as another semicircle (hence onwards second semicircle)and initial semicircle (hence onwards first semicircle)becomes bigger and partly goes out of frequency window. For still lower temperatures, the first semicircle completely goes out of the frequency window and only second semicircle remains with increasing size on lowering of temperature. For dielectrics, the Cole-Cole plot may be described by a generalized equation proposed by Haverliak-Negami[34],

$$\epsilon^*(\omega) = \epsilon_\infty + \frac{\epsilon_s - \epsilon_\infty}{[1 + (j\omega\tau)^\alpha]^\beta} \tag{3.1}$$

with $\epsilon^{'} - \epsilon_\infty$ on the real axis, $\epsilon^{''}$ on the imaginary axis and radius is $\epsilon_s - \epsilon_\infty$. Here, the parameters $\alpha < 1$ and $\beta < 1$ stands for the deviation from Debye behaviour and $\alpha = 1$ and $\beta = 1$ establishes Debye behaviour. Since there is no equivalent Haverliak-Negami expression for impedance, the impedance data is fitted to an equivalent expression[78],

$$Z^*(\omega) = \frac{R}{[1 + (j\omega\tau)^\alpha]^\beta} \tag{3.2}$$

whose real and imaginary components are related for the Cole-Cole plot as,

$$(Z^{'} - X_1)^2 - Z^{''2} = R^2\Big(1 + 2\omega\tau\alpha\cos(\frac{\pi\alpha}{2})\Big)^\beta \tag{3.3}$$

where R is the resistance term, τ represents the characteristic relaxation time, $0 < \alpha < 1$ and $0 < \beta < 1$ are the symmetric and asymmetric broadening respectively. $\alpha = 1$ and $\beta = 1$, corresponds to the Debye case, hence the above equation is a generalized form incorporating both Debye and non-Debye cases. The solid lines in the Cole-Cole plot (fig.3.1,3.2) of impedance data show the fitting to Eq. (fig.3.3). The fitting is done in Origin^{TM} software by making use of OriginC options, which facilitates fitting of Nyquist as well as Bode plots simultaneously. The fitting is found to be extremely good. From the fitting, the obtained parameters R, α, β, τ, for the two respective semicircles are shown in fig. 3.3, where the numerals 1 and 2 stand for the first and second semicircles, respectively.

A widely followed concept in the appearance of two semicircles in the case of

polycrystalline materials is that they stand for the relaxation processes in grain and grain boundaries, respectively[52]. Here, the two semicircles surely represent the two relaxation process, but not the grain and grain boundary, but to the two crystallographic phases *Pbnm* and $R-3c$. Series of samples prepared at different temperatures have been studied by Joly *et al.,* where the authors have shown that glycine nitrate method of preparing LNM results biphasic samples, with varying degree of *Pbnm* and $R-3c$ depending on the sintering temperature[44]. For T $>$ 1300°C, purely $R-3c$ phase and for T $<$ 400°C purely *Pbnm* phase and 400° $<$ T $<$ 1300°C, both phases coexists. Para to ferromagnetic transitions for $R-3c$ phase happens at 270 K and that for *Pbnm* phase 150 K. The temperature dependence of magnetization of our sample is shown in fig.3.3(a). The data are in good agreement with that obtained by Joly *et al.,* where $R-3c$ phase transition 270K and *Pbnm* phase transition 150K are clearly seen. Based on the magnetization response, the temperature range is divided in three regions: (1) T $>$ 270 K, both *Pbnm* and $R-3c$ phases are in paramagnetic state, (2) 150K $<$ T $<$ 270K, $R-3c$ ferromagnetic and *Pbnm* still paramagnetic, (3) T $<$ 150 K, both *Pbnm* and $R-3c$ are ferromagnetic. The R1 and R2 parameters obtained from the fitting are plotted in fig.(3.3)(b). At 300K and above, only R1 is in the window and R2 is apparent only below 280K, though could not be measured accurately until 250K.

At the onset of magnetic ordering $\sim$ 285K for $R-3c$ phase (obtained from the peak of derivative of M $\sim$ T plot), the behaviour of resistivity corresponding to $R-3c$ phase changes and rises more steeply. Below T_C, the resistivity of $R-3c$ phase shows logarithmic increase of resistivity with decrease in temperature, till 140K. In the same temperature range, rise in R2 is slightly steeper than that of R1. At 170K, R1 disappears whereas R2 shows a discontinuity and rises more steeply below 170K.

It is customary to fit the so obtained resistance values to hopping models: (1) nearest neighbour hopping $\rho = \rho_0\ exp\left(\frac{E_{hop}}{K_\beta T}\right)$, where an electron hops to the nearest localized state higher by E_{hop} from the former state or (2) variable range hopping model $\rho = \rho_0\ exp\left(\frac{T_0}{T}\right)^{1/4}$, where the probability of nearest neighbour hopping decreases because of low temperature and the electron has to hop between

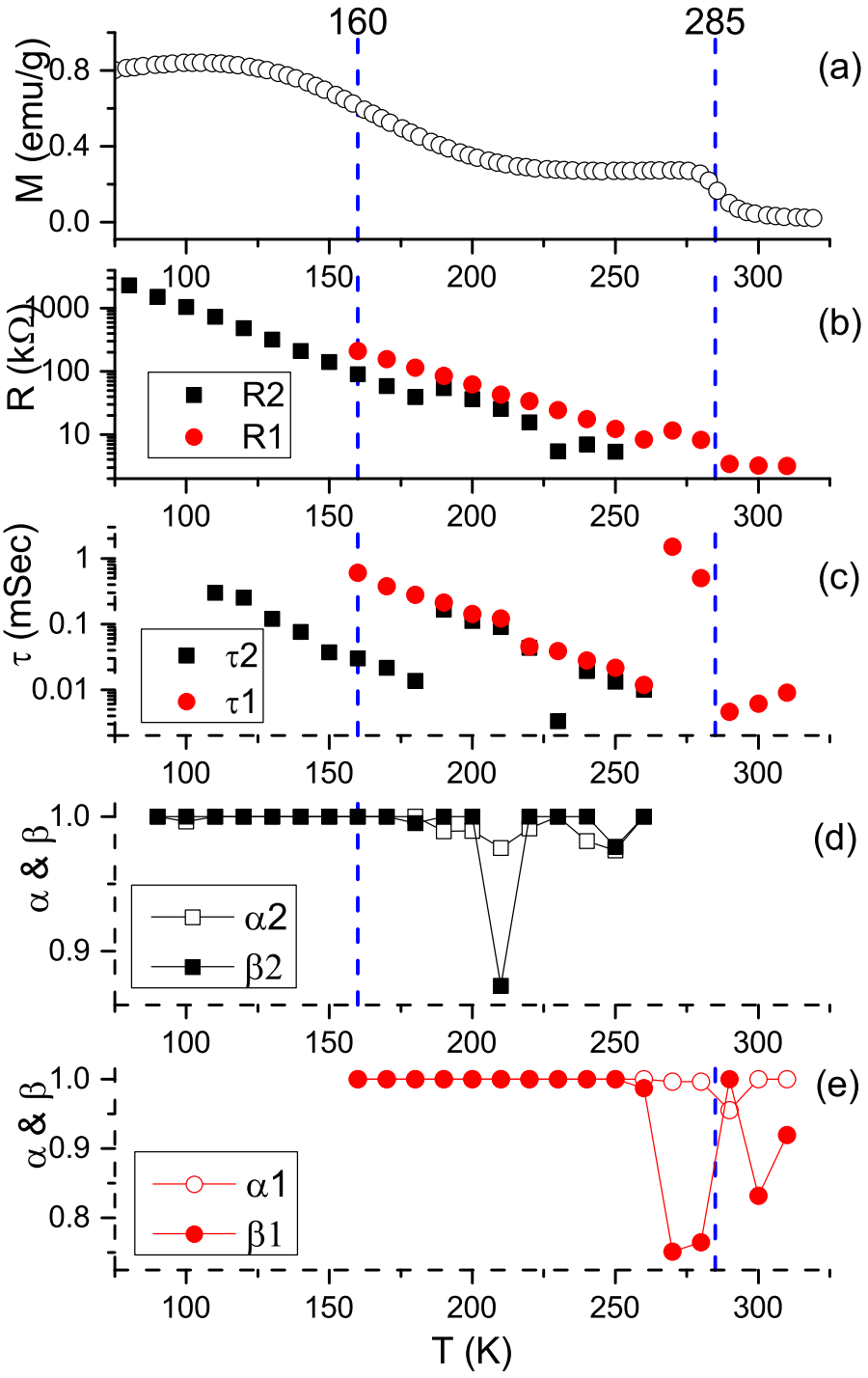

FIGURE 3.3: (a) M∼T measurement data at 0.01T. (b)-(e) Temperature dependence plot of various parameters obtained by fitting the impedance data to Eq. (3.3). (b) R1 & R2 (c) τ_1 & τ_2 (d)α_1 & β_1 (e)α_2 & β_2. The dashed vertical lines are the mark to the temperatures 160K and 285K, and just a guide to eye.

some remote states[79]. Hence, a general form of hopping expression may be written as

$$\rho \propto exp\left(\frac{A}{T}\right)^{x} \tag{3.4}$$

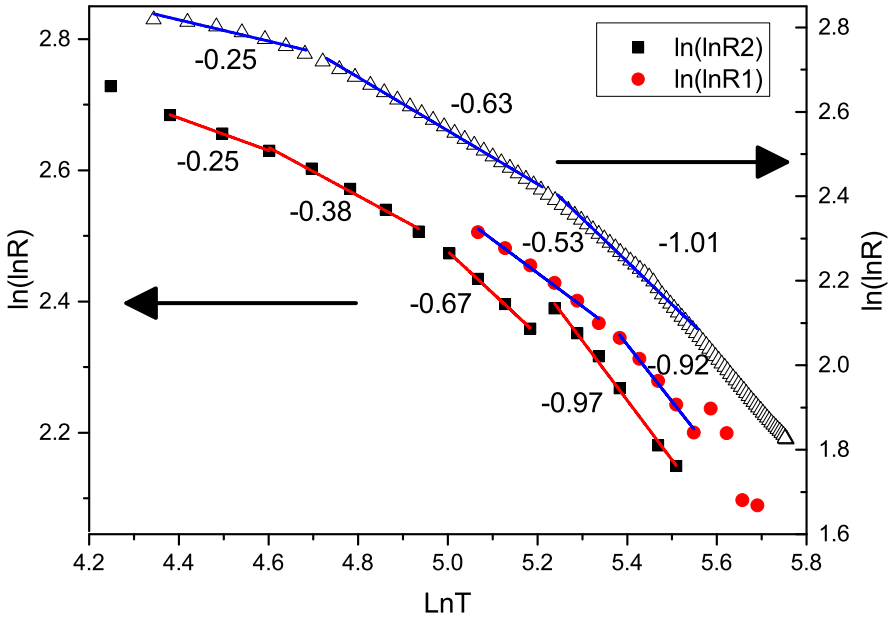

FIGURE 3.4: Hopping conduction in LNM. Solid lines are straight line fitting. The numerals against fitted line stand for the exponent '-x'. The open symbol stands for the data obtained from dc measurements and solid symbols stands for that obtained from Nyquist plot.

where A = T_0, x = 1/4 for Mott VRH and $A = E_{hop}/K_\beta$, x = 1 for nearest neighbour hopping. Often, the entire temperature range is not covered by either of the models and transition from nearest neighbour hopping near room temperature ($x = 1$) to variable range hopping at low temperature ($x = 0.25$) is observed. Many a times, the authors show these two behaviours as linear fitting of lnR vs $(1/T)$ or $(1/T)^{1/4}$ for the two hopping processes. It must be mentioned here that a small portion of any curve may be fitted to straight line. But it is the value of exponent which determines the actual hopping process: $x = 1/4$ for a Mott VRH and $x = 1$ for nearest neighbour hopping. To obtain the exponent x, we plotted the ln(ln$R$) vs lnT (see fig.3.4),whose slope gives the exponent '$-x$'[80]. From the plot, it is very clear that the high temperature region is dominated by nearest neighbour hopping ($x \sim 0.9$) which tends towards Mott VRH ($x \sim 0.25$) with lowering of temperature. One interesting point which may be noted from the plot is that the exponent values are independent for the two crystallographic phases R1 and R2, indicating independent hopping processes in the respective phases. For comparison purpose, the resistance data obtained from the dc measurement are also shown in the same plot.

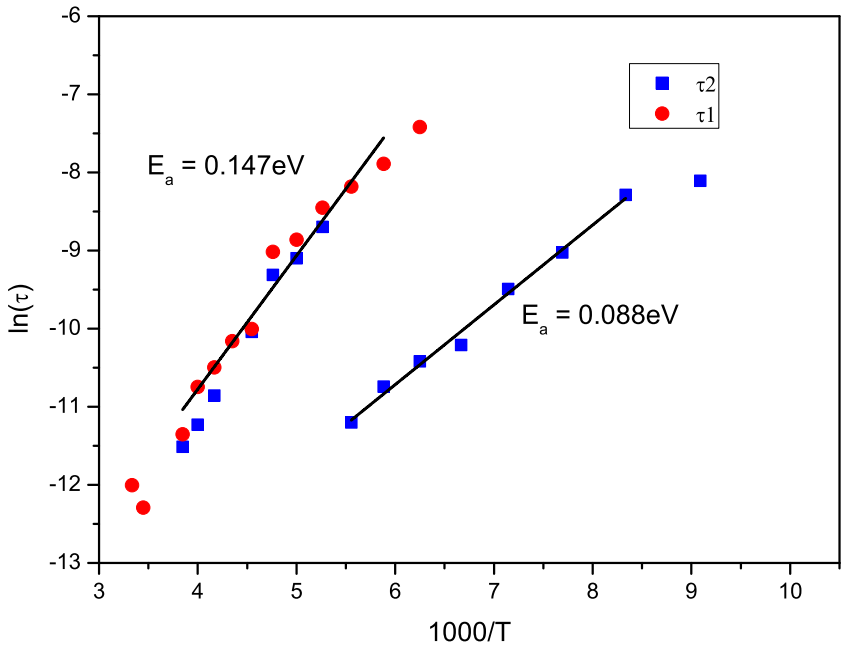

FIGURE 3.5: Activated behaviour of the two relaxation times τ_1 and τ_2. The numerals beside the fit, represents the activation energy.

The τ_1 and τ_2 obtained from the Cole-Cole plots are shown in fig 3.3c. Similar to R1 and R2 plot, here also two well distinguished relaxation times corresponding to the two phases are seen. One important point also observed in the plot is that, before the onset of T_{C2} i.e, in the paramagnetic state of *Pbnm*, the τ_2 equals τ_1 , i.e., *Pbnm* phase is relaxing at par with $R-3c$ phase. Only below T_{C2}, when *Pbnm* phase enters ferromagnetic region, τ_2 attains a different value smaller than τ_1. This is a very clear evidence of strong magnetoelectric coupling, where magnetic ordering influences the dielectric relaxation process. The relaxation times so obtained are often found to obey activated behaviour $\tau = \tau_0\ exp\Big(\frac{E_a}{K_\beta T}\Big)$. Plot of lnτ vs 1000/T in fig 3.5 showing the linear behaviour, confirms the activated behaviour of relaxation time. From the fitting, the activation energy E_a and τ_0 obtained for $R-3c$ and *Pbnm* phases are 0.147 eV & 0.088 eV and 2.2×10^{-8}s & 4.8×10^{-8}s respectively. Because of lower value of activation energy in *Pbnm* phase than that in $R-3c$ phase, below 150K the relaxations are occurring via *Pbnm* phase. Probably that's why only one semicircle corresponding to *Pbnm*

appears for T $<$ 150K where as that of $R-3c$ is absent. For 270K $\leq$ T $<$ 285K, the relaxation time τ_1 shows abrupt jump. Similar jump is seen in the plot of R (fig 3.3b) and drop in α_1 (fig 3.3d) and β_1 (fig 3.3e). These abruptnesses might be related to Griffiths like phase in the same temperature region (discussed later).

Fig 3.3d & 3.3e show the parameters for symmetric and asymmetric broadening α and β for the phases 1 & 2. Deviations from unity in the values of α and β are an indication of non-Debye nature of relaxations. According to the plot, their values prior to ferromagnetic transitions for the respective phases, are less than unity and after transition, they take a stable unity value. This indicates that the relaxation above ferromagnetic transition temperature might be associated with non-Debye nature of relaxations. Interestingly, the α and β for the phases 1 & 2 are independent and only depend on the respective magnetic state of the phases.

3.2.2 Modulus Study

To acquire more in depth information on this, the imaginary component of impedance and modulus data are co-plotted in the same graph (see fig3.6). Coincidence of maxima position for the two at the same value of frequency reflects Debye nature whereas at separate positions mark non-Debye nature of relaxation. In the plot, the dotted lines are used to locate and match the maxima position in impedance and modulus spectra.

For the sake of clarity, only selected temperature data are plotted and the impedance (normalized with respect to peak values) graphs are relatively off shifted. Based on their behaviour, the impedance spectra are divided in two sections, $T > 170$K and $T < 170$K. For $T < 170$K, there is one to one correspondence of the impedance and modulus maxima. Whereas for $T > 170$K, the impedance and modulus maxima are well separated on frequency scale. However a small shoulder is seen in the impedance spectra right at the maxima position of modulus (shown by upward arrow) and similarly for the modulus spectra as well. Since Impedance spectra

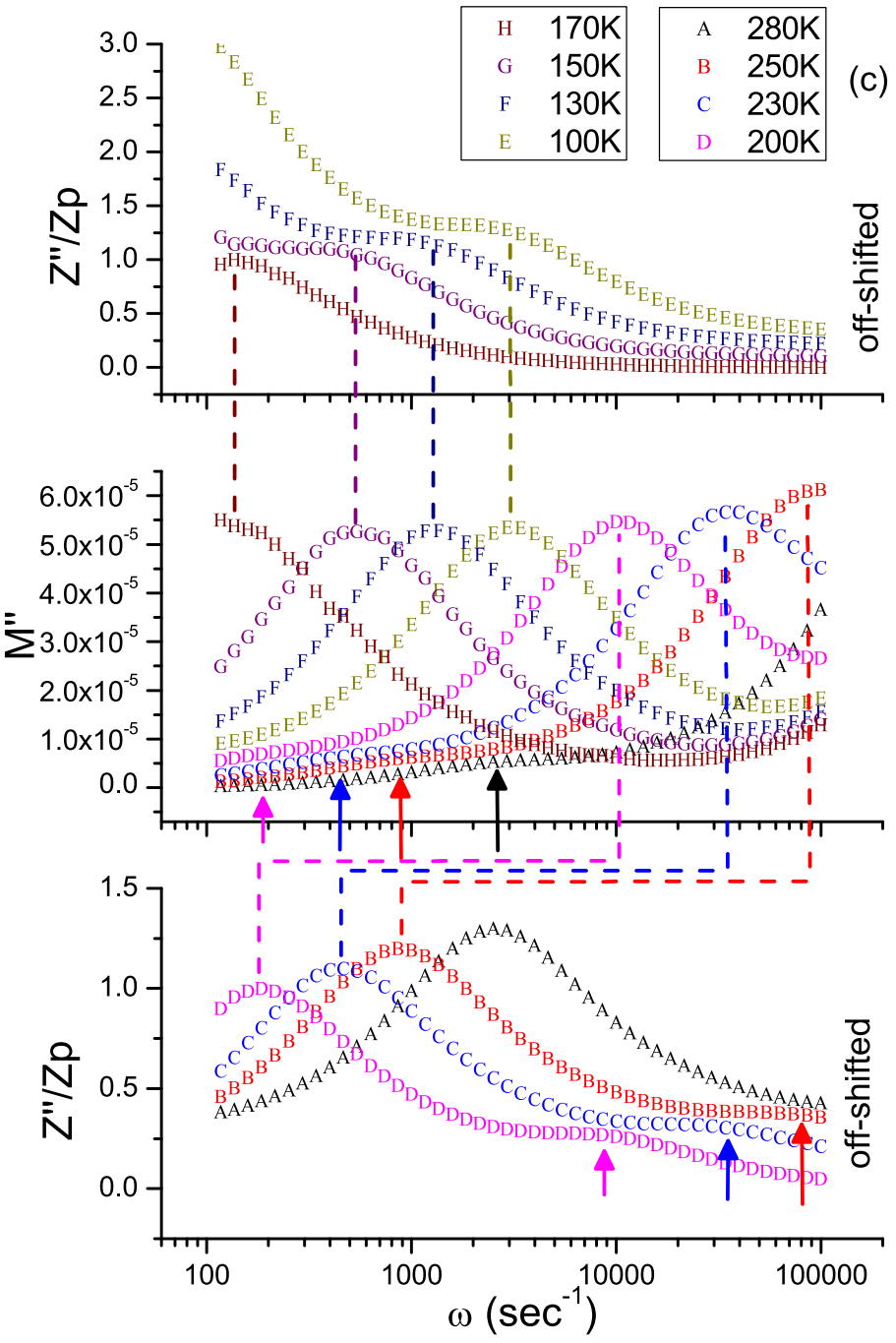

FIGURE 3.6: Co-plotting of Z'' with M'' for the investigation of Debye & non-Debye relaxations. The dashed lines join the maxima positions of modulus to impedance spectra. The arrows show the shoulder positions in impedance and modulus corresponding to the maxima positions in modulus and impedance respectively.

is dominated by resistive component and modulus spectra is dominated by capacitive component [81], such behaviour also indicates the important role played by magnetic ordering in the relaxation of resistive and capacitive components.

In spite of differences, some correlation does exist between the two components ($T > 170$K), probably because of magnetic ordering of $R - 3c$ phase. In terms of nature of relaxation, below 170K is dominated by Debye nature where both resistive and capacitive terms relax with same time constant whereas above 170K the two components relax with different time.

3.2.3 Dielectric Study

In the previous discussions, we have shown that both Debye and non-Debye processes contribute to the relaxation. However nothing has been said so far about the dielectric relaxations. It is important to know the nature of the relaxing dipoles, that is whether the dielectric relaxation is originated from intrinsic dipoles or do they have the origin from the extrinsic charge carriers.

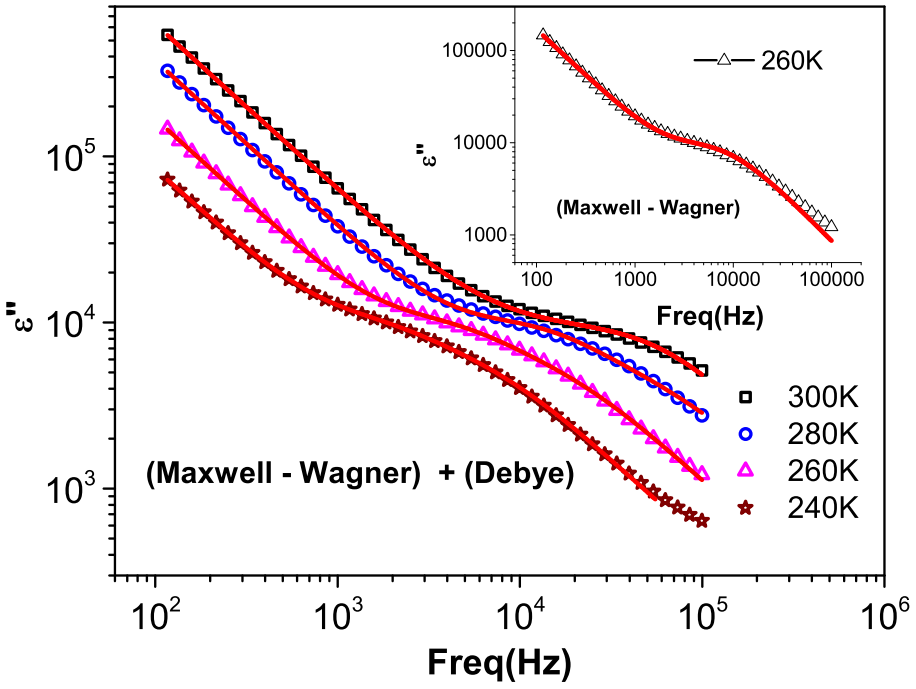

FIGURE 3.7: Frequency dependence of ϵ'' at various temperatures fitted to Maxwell-Wagner + Debye relaxation. Inset shows the poor fitting when data is fitted only to Maxwell – Wagner relaxation mechanism.

In order to address this issue frequency dependence of imaginary part of dielectric ϵ'' at various temperatures is plotted in fig.3.7. A monotonous decrease in ϵ'' with increasing frequency (at low frequency) is an indication of dominant Maxwell – Wagner type mechanism of dipolar relaxation. In an attempt to fit the data with Maxwell Wagner model alone, we found the fitting deviates from the experimental data at higher frequencies (see inset of fig 3.7), suggesting multiple dielectric relaxation mechanisms. Hence in second attempt (see fig 3.7), intrinsic dipolar relaxation or Debye type relaxation mechanism is also incorporated along with the Maxwell – Wagner relaxation mechanism [8]. The fitting (red solid line) is found to be very good. This shows that both Maxwell-Wagner and Debye type dielectric relaxations contributes. For the sake of clarity, only selected temperature data are shown.

3.2.4 Griffiths Phase Characterization

In search for the origin of non-Debye nature of relaxation in LNM, we came across reports of short range ordering before the actual T_C [50, 82] and hence possibility of Griffiths like phase [83]. For a Griffiths phase, the χ^{-1} deviates from the linear paramagnetic behaviour at T_G and drops sharply much before the actual T_C. Application of magnetic field restores this behaviour [20, 21]. Hence to confirm this, the inverse of dc susceptibility is plotted as a function of temperature (fig 3.8a). For the sake of clarity, χ^{-1} is plotted in log scale.

The data is found to be slightly oppressed in 150K $<$ T $<$ 225K and increasing magnetic field suppresses this oppression, but at the same time χ^{-1} value rises slightly. This raises a possibility of Griffiths phase in the sample, as $R-3c$ phase (which is also major phase) is already in ferromagnetic state. In fig 3.8b, the data is linearly fitted in the region before any magnetic ordering takes place i.e, in the paramagnetic region. In this region itself, we find two types of behaviour which is fitted linearly and extrapolated till x-axis intercept. Linear fitting of high temperature (T $>$ 315K) data (line A) makes an x-axis intercept at $\sim$ 230K, which also happens to be the initiation of ordering of *Pbnm* phase (see the deviation of

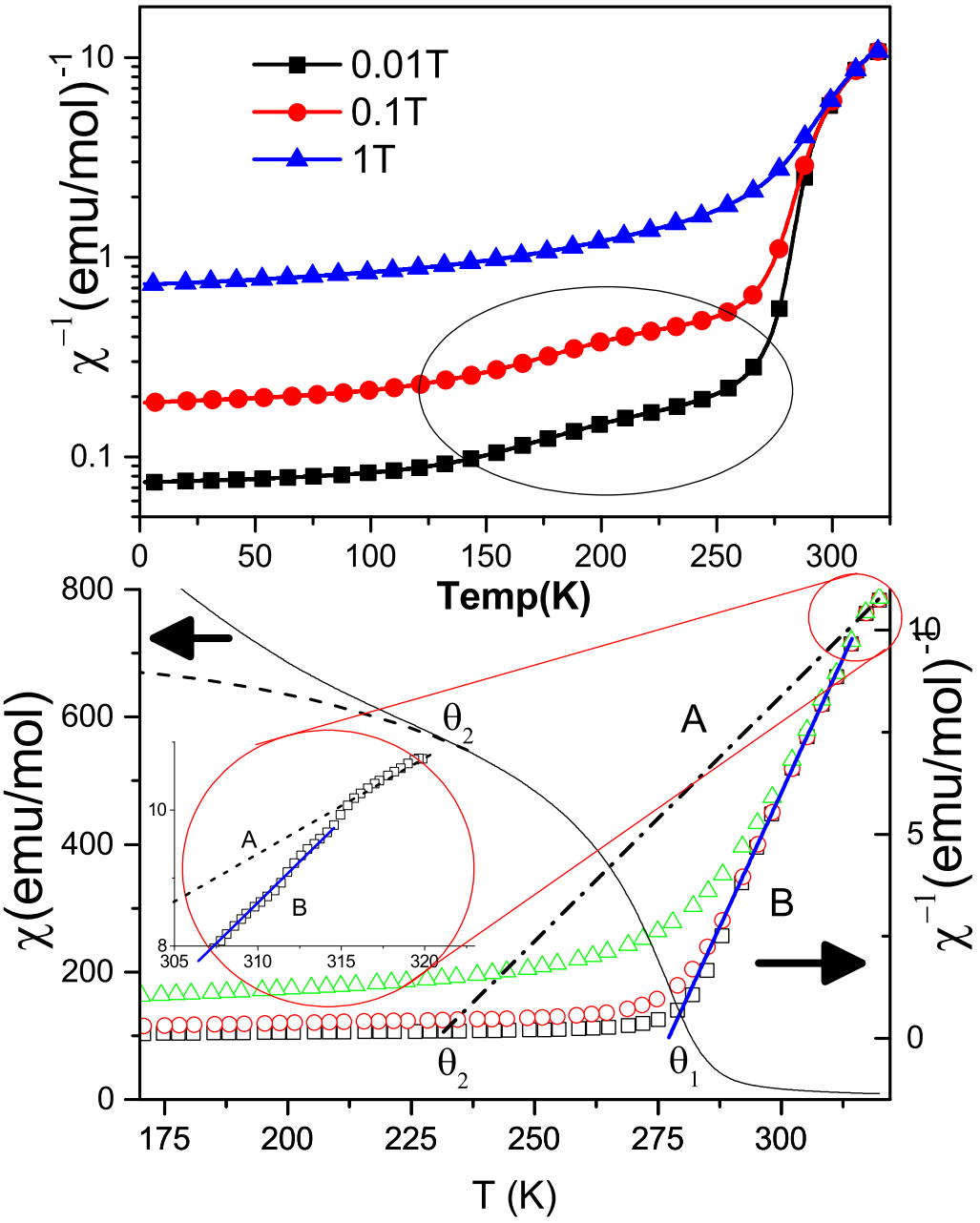

FIGURE 3.8: (a) Temperature dependence of χ^{-1} in log scale, under magnetic field of 0.01T, 0.1T & 1T. (b) Linear fitting to χ^{-1} for estimation of ordering temperature θ. Fitting of data above 315K (line A) and below 315K (line B) gives two different values of ordering temperature θ_1 and θ_2. Magnetization data is also shown to mark the behaviour of magnetization at the two ordering temperatures.

magnetization data below 230K, in fig 3.8b) hence named θ_2. For the linear fitting of data below 315K (line B), the intercept happens at $\sim$ 277K, which is close to the ordering temperature for $R-3c$ phase, hence named θ_1. Surprisingly,

T_c = 285K obtained from the peak position of derivative of magnetization data differs from θ_1, hence the data in the region 277–285K needs to be examined more closely. Fig. 3.9 shows the magnified view of temperature dependence of χ^{-1} in the Griffiths suspected region 277–285K. The data taken for 0.01T magnetic field, deviates from the linear paramagnetic behaviour at 295K and drops little faster. Linear extrapolation of this region gives x-axis intercept at $\sim$ 282K, which also happens to be the peak position of derivative of magnetization data. On applying 0.1T magnetic field, this sudden drop vanishes and the data follows a linear behaviour as per the data above 290K. At these temperatures, both the crystallographic phases are paramagnetic, hence such behaviour is reminiscent of Griffiths phase above 277K having T_G = 295K. Earlier we saw that, the dielectric

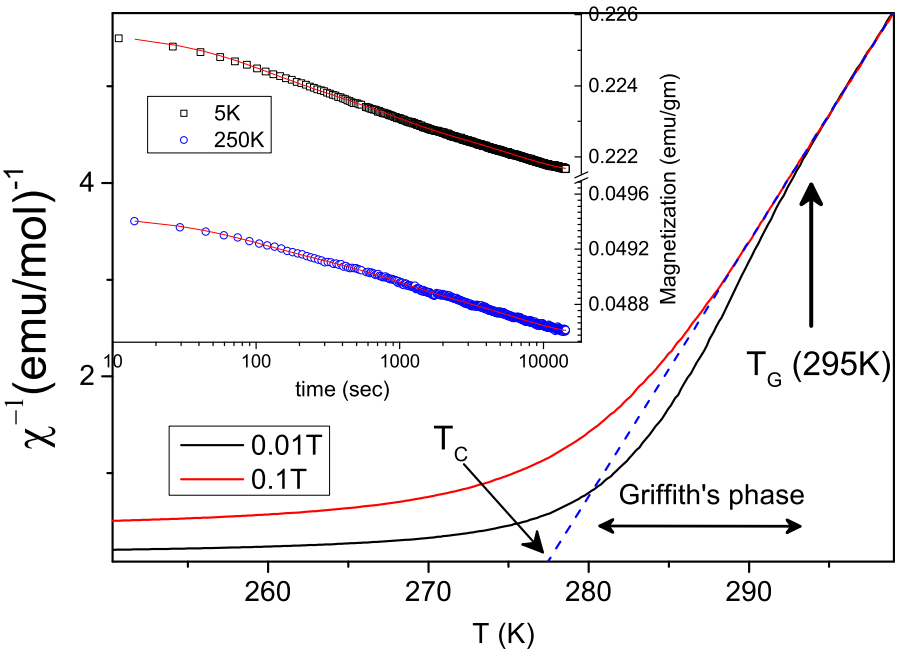

FIGURE 3.9: Enlarged view of the χ^{-1} plot near room temperature, showing the deviation from the linear paramagnetic behaviour, marking the appearance of Griffiths phase. Application of 0.1T of magnetic field removes this anomaly and true ordering temperature is seen. The inset shows the relaxation of magnetization as a function of time. The lines stand for the fitting of data to three exponential relaxation.

relaxation time is strongly linked to the magnetic ordering present. Hence to know if the spin relaxation too follows the dielectric relaxation behaviour, we performed the magnetization decay measurements as a function of time at two temperatures viz., 250K (only $R-3c$ phase is magnetically ordered) and 5K (both phases are

magnetically ordered). A good exponential decay fit (see inset of Fig.3.9) to the data is found for combination of three different time constants 4100s, 480s and 60s. Surprisingly the three time constants at the two temperatures, 5K & 250K, remain same, within the experimental errors. This shows that in spite of close association of magnetic ordering with dielectric relaxation, the respective magnetic orderings hardly interferes with the spin dynamics of each other's phases.

3.3 Conclusion

Polycrystalline LMN prepared via sol-gel nitrate method are biphasic ($R-3c$ & $Pbnm$) in nature. The $R-3c$ and $Pbnm$ phase orders ferromagnetically at 277K and 160K respectively. The impedance data is analysed via Nyquist plot and the corresponding resistance, time constant, symmetric and asymmetric broadening parameters are obtained from the fitting of Nyquist plot. Plot of resistance as a function of temperature shows hopping nature of conduction with extended hopping at room temperature and transition to Mott VRH at low temperature. The time constants for the two phases show activated behaviour with activation energy 0.147eV and 0.088eV for $R-3c$ and $Pbnm$ phases respectively. Also, indication of strong magnetic ordering dependent dielectric relaxation is seen in the time constant plot. The values of symmetric and asymmetric broadening parameters show Debye type relaxations in the ferromagnetic region of respective phases and Non- Debye nature before the ferromagnetic ordering temperature. Signature of Griffiths phase is seen in the temperature range 277 – 295K. Interestingly, the spin relaxation seen in the Magnetization vs time plot at 250K and 5K, shows relaxation with same time constants, indicates similar spin dynamics at the two temperatures.

Chapter 4

Effect of Cu substitution on the magnetic, dielectric and transport properties of La_2NiMnO_6

4.1 Introduction

Biphasic LNM, prepared at lower temperature suggest a combination of rhombohedral ($R-3c$) and orthorhombic ($Pbnm$) crystallographic phases with their respective ferromagnetic (FM) transitions at different temperatures [44, 55]. The magnetic ordering of rhombohedral phase occurs at relatively higher temperature ($\sim$ 270K) than the orthorhombic phase ($\sim$ 150K) [44, 55]. Owing to near room temperature magnetic transition of $R-3c$ phase, enhancement of $R-3c$ content in the sample via methods other than high temperature sintering, such as chemical substitution, is highly desirable.

The FM $R-3c$ phase is governed by Mn^{4+}–Ni^{2+} whereas in and FM $Pbnm$ phase is due to Mn^{3+}–Ni^{3+} superexchange interactions [36, 69]. Disorder induced

J. Appl. Phys. **117**, 17B728 (2015).

antiferromagnetic (AFM) interactions Ni^{2+}–Ni^{2+} and Mn^{4+}–Mn^{4+} along with FM order, leads magnetic frustration [8, 36] hence spin glass like magnetism in the system [8, 42]. Thus due to magnetoelectric coupling, glassy dielectric property may be witnessed for the systems with intrinsic dielectric behaviour arising from asymmetric hopping between Mn^{4+}–Ni^{2+} ions [8].

Previous chapter addressed the signature of short range magnetic ordering before T_C [50], reminiscent to Griffiths like phase, in addition to the dielectric relaxations with strong magnetic correlation [55]. In this chapter, structural, magnetic and electrical property of biphasic $La_2Ni_{1-x}Cu_xMnO_6$ is studied. Cu^{2+} is chosen for its similar ionic radii (73pm: Cu^{2+}) with Ni^{2+} (70pm). Moreover Cu^{2+}, is more divalent, so its substitution is expected to enhance Mn^{4+} – Ni^{4+} interactions thereby stabilization of $R-3c$ phase.

4.2 Results and Discussion

4.2.1 Magnetization Study

The temperature dependent zero field cooled (ZFC) magnetization (in 0.01 T) data for all the samples are shown in fig.4.1. Two distinct ferromagnetic transitions are seen for all the samples at $\sim$ 270K and $\sim$ 150K. In the earlier chapter, these transitions have been shown to represent paramagnetic (PM) to ferromagnetic (FM) transition for $R-3c$ phase at $\sim$ 270K and that of *Pbnm* phase at $\sim$ 150K.

The FM Curie temperature (T_C) obtained from the derivative plot (dM/dT vs. T: see inset fig.4.1) shows a decrease in T_C on increasing the Cu^{2+} content in sample (see table 4.1). Apart from this, few additional features found worth for investigation are, drop in magnetization below T_C leading to appearance of peak like feature in the magnetization plot at $\sim 260-270$K and $\sim$ 100K and a weak shoulder in the magnetization $\sim$ 30K. For Cu substituted samples, the 30K shoulder (also present in parent LNM), becomes prominent along with a gradual shift towards high T side. Moreover, the magnetization peak $\sim$ 100K becomes

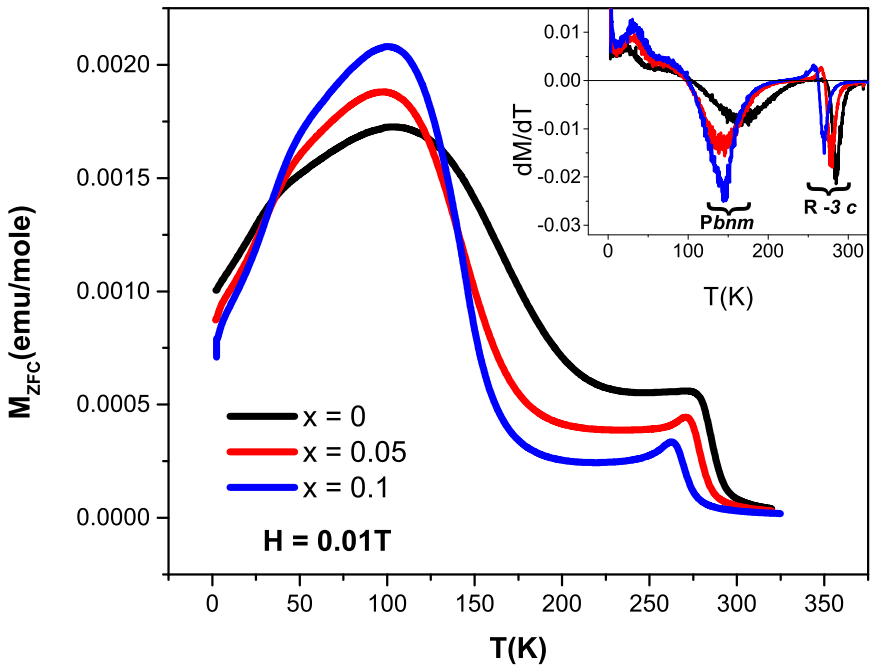

FIGURE 4.1: Zero field cooled (ZFC) magnetization vs. T at H = 0.01T, for x = 0, 0.05 & 0.1. Inset shows the respective dM/dT plots.

sharper and intense with increasing Cu^{2+} content. These developments suggest growing antiferromagnetic (AFM) interactions for Cu^{2+} substituted samples.

The above mentioned features may be summarized as (1) the PM-FM transition of $R-3c$ phase $\sim$ 270K is weakened and hint of AFM interactions just below T_C is clearly seen, for Cu substituted samples, (2) the PM-FM transition of *Pbnm* phase $\sim$ 150K becomes sharper, but at further lower temperatures, the magnetization decreases drastically, probably due to growing AFM interactions (3) a shoulder $\sim$ 30K seen in the parent LNM becomes prominent for Cu substituted samples and this also hints at the ordering of magnetic moments leading to AFM state. Thus a number of FM and AFM transitions are seen, most of them were also present in parent LNM but were masked by other perturbations and became clear only on substituting Cu^{2+}. Thus Cu^{2+} substitution minimizes the perturbations, hence gives a clear picture of the various transitions taking place as a function of temperature.

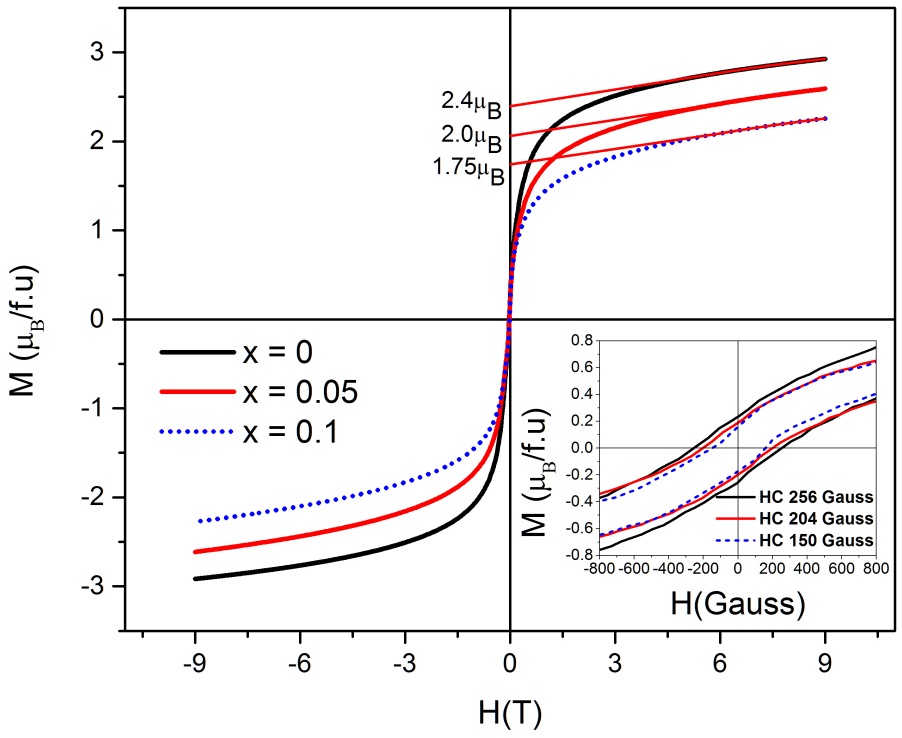

FIGURE 4.2: Isothermal magnetization data at 100K for x = 0, 0.05 & 0.1. Inset shows the zoomed near zero field region for determination of coerceivity.

The T_C of $R-3c$ phase decreases systematically with Cu^{2+} content, 285K ($x = 0$), 278K ($x = 0.05$), 270K ($x = 0.1$). As the $R-3c$ phase predominantly contains Mn^{4+} and Ni^{2+} ions [36], substitution of a strongly divalent Cu^{2+} for Ni^{2+} will strengthen the Mn^{4+}/Ni^{2+} configuration and hence stabilization of $R-3c$ phase is expected. This is supported by the X-ray diffraction results, which shows increasing percentage of $R-3c$ phase for Cu^{2+} substituted samples. The systematic decrease of T_C may be attributed to the magnetic dilution of Ni^{2+} ($2.83\mu_\beta$) by a less magnetic Cu^{2+} ($1.73\mu_\beta$). This is also supported from the observation that the value of saturation magnetization (M_s) and coercive field (H_C) at 100K (see fig. 4.2) decreases with increasing Cu^{2+} content: $2.4\mu_\beta$ & 256 Gauss ($x = 0$), $2\mu_\beta$ & 204Gauss ($x = 0.05$) and $1.75\mu_\beta$ & 150Gauss ($x = 0.1$). Inclusion of less magnetic divalent Cu^{2+} ions are expected to weaken the nearest neighbour Mn^{4+}/Ni^{2+} interactions due to low magnetic moment of Cu^{2+}. Thus the next nearest neighbour interactions such as Mn^{4+}/Mn^{4+} and Ni^{2+}/Ni^{2+} will be the

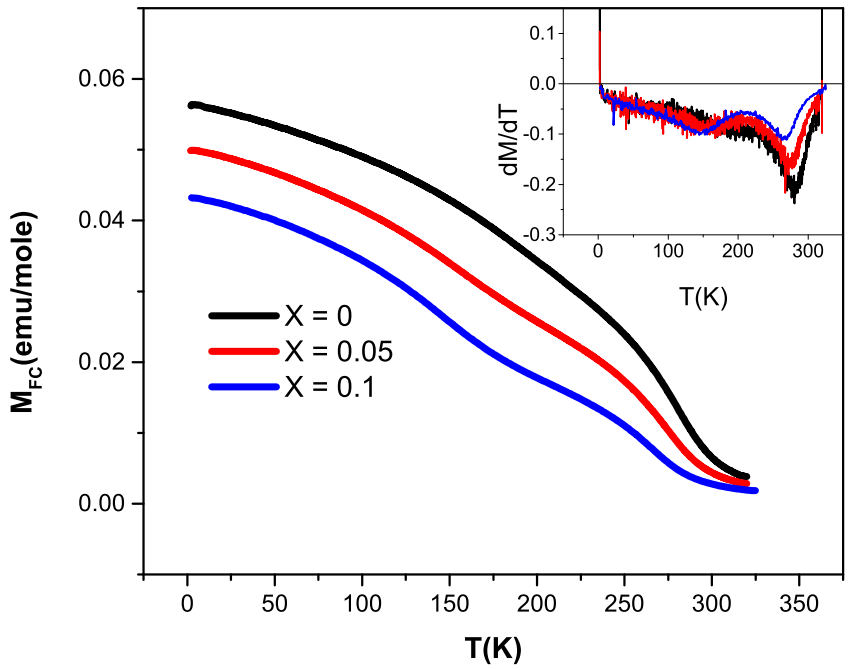

FIGURE 4.3: FC magnetization vs. T at H = 1T, for x =0, 0.05, 0.1. Inset shows the respective dM/dT plots.

leading interactions, which interacts antiferromagnetically [36]. This explains the appearance of AFM peak just below the FM T_C of $R-3c$ phase, on increasing the Cu^{2+} in sample. In the parent LNM also, these interactions were present, but were masked by the strong Mn^{4+}/Ni^{2+} FM interactions. However on applying higher magnetic field (1T) the antiferromagnetic features disappear (see fig.4.3 & inset).

The T_C (obtained from dM/dT) of *Pbnm* phase initially decreases and then remains unchanged 165K (x = 0), 145K (x = 0.05) & 145K (x = 0.1). The peak position $\sim$ 100K in the M vs. T plot remains unchanged for all the samples, rather the peak width decreases and the peak become sharper with increasing Cu^{2+}. This may be the reason behind initial shift in T_C, which was probably masked due to broadening of 100K peak and its true position is revealed only when the peak narrows down. A wider magnetic transition is an indication of magnetic disorder, where the interactions of varying strengths makes the ordering complex and prohibits it to exhibit the true transition temperature. The *Pbnm* system is known

to be dominated by Mn^{3+}/Ni^{3+} interactions, and hence reduction in magnetic disorder does not seems to be a direct consequence of Cu^{2+} substitution. It has been shown that the *Pbnm* phase is associated with large random distribution of Co/Mn ions in Pr_2CoMnO_6, which also displays dual crystallographic phases with *Pbnm* ordering being the low temperature one [84]. Random distribution of magnetic ions is supposed to display varying degree of interactions and thus may lead to increase in the width of ordering temperature, which indeed is seen for the parent ($x = 0$) sample. Reduction in the volume fraction of *Pbnm* phase due to substitution of divalent Cu^{2+}, also leads to decrease in the associated magnetic disorders, so that net magnetization of *Pbnm* phase increases. Moreover the other FM/AFM interactions become free from external perturbations to display their true ordering temperature. To confirm this proposition, relaxation dynamics of ZFC magnetization is measured at 5K (fig.4.4). Similar to the earlier chapter, here too the data are found to be fitted to three exponential decay functions, whose respective relaxation times (τ_1, τ_2, τ_3) differs by an order of magnitude. Cu-substitution causes a decrease in the magnitude of these three relaxation times (see table 4.1). Decrease in relaxation times is an indication of faster dynamics, thus supporting the above mentioned proposition. To comment more on the magnetic moments arrangements responsible for this may require a neutron diffraction studies on these samples.

In the previous chapter on LNM, signature of Griffiths phase before the onset of actual T_C has been shown [55]. Here, the effect of Cu^{2+} substitution on this Griffiths phase has been addressed. The temperature dependent inverse susceptibility (χ^{-1} vs. T) plots measured in 0.01T and 0.1T magnetic field are shown for all the three samples in fig.4.5. The χ^{-1} measured in 0.01T shows the sudden downward deviation from linear Curie Weiss behaviour (dotted red line) in the paramagnetic region. The sudden downward deviation recovers on increasing field to 0.1T. Such behaviour has been shown to be imprint of Griffiths phase[85]. The temperature, at which the deviation in χ^{-1} begins, is called Griffiths temperature (T_G). The respective T_G values are found to be 295K (for $x = 0$) and 281K (for $x = 0.05\&1$).

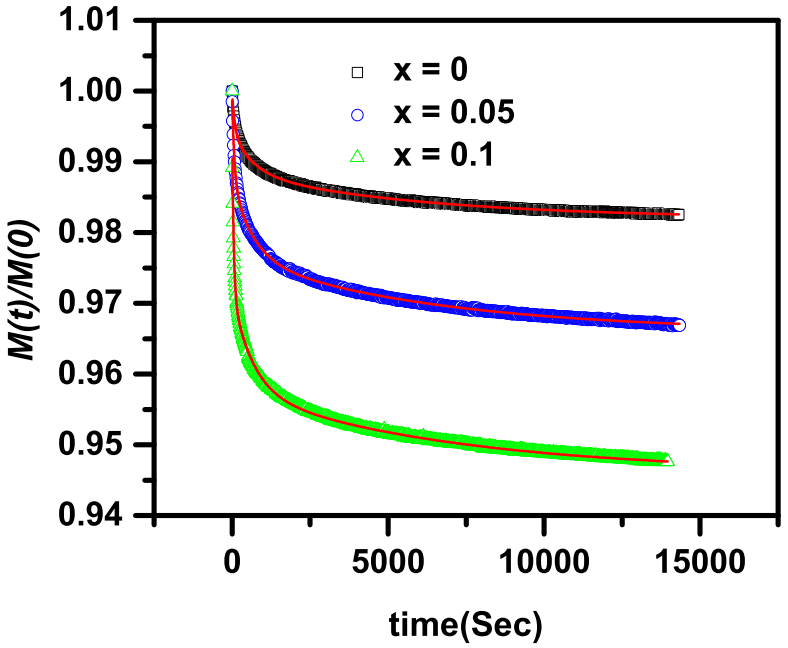

FIGURE 4.4: Relaxation dynamics of magnetization at 5K for x = 0, 0.05 & 0.1.

Similarly, the respective Curie-Weiss temperature 'θ' for the three samples thus obtained are 277K ($x = 0$), 270K ($x = 0.05$) and 260K ($x = 0.1$).

Often the Griffiths phase is found to obey modified Curie Weiss (CW) law [86] having form,

$$\chi^{-1} \propto (T - \theta)^{1-\lambda} \tag{4.1}$$

where the exponent $0 < \lambda < 1$, marks the deviation from ideal CW law. A non-zero value of λ implies the presence of Griffiths phase whereas for ideal CW behaviour, $\lambda = 0$. Fitting of the data falling in the region θ to T_G, via equation 4.1 (see inset fig.4.5), gives the exponent λ, which may also be considered as a measure of strength of Griffiths singularity. For clarity, the graphs shown in the inset are slightly off shifted by 0.3 and 0.6 units along the abscissa for x= 0.05 and 0.1 respectively. The increase in the value of λ for Cu substituted samples suggests an increase in the strength of Griffiths phase.

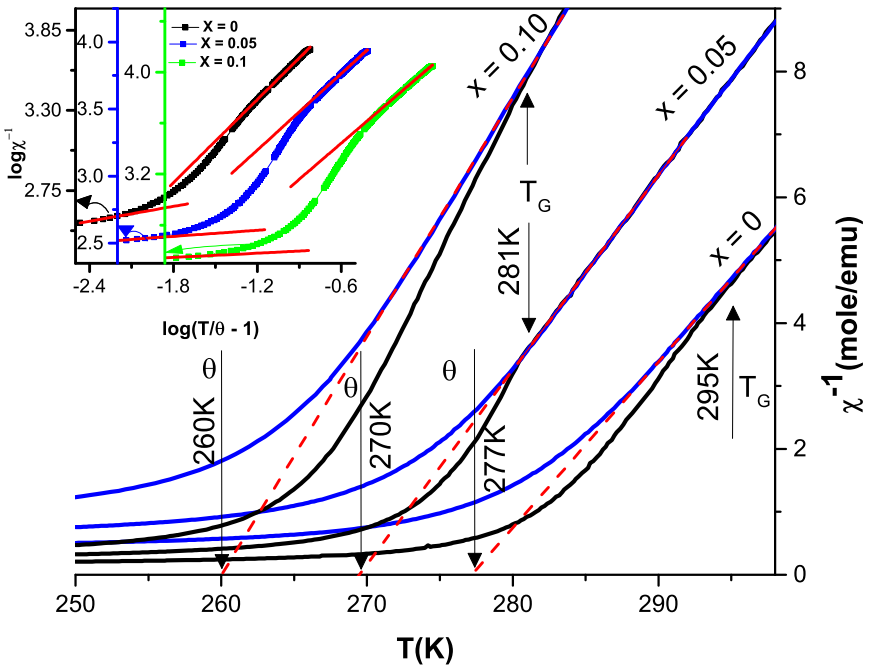

FIGURE 4.5: χ^{-1} vs. T plot in Griffiths phase region for x = 0, 0.05 & 0 .1. The dotted red line represents the Curie – Weiss fit. Inset shows the fit to eq.4.1 for determining the value of λ.

4.2.2 DC Resistance Study

In fig.3.4, we have seen the temperature behaviour of DC resistance of LNM showing nearest neighbour hopping at high temperature which tends towards Mott VRH with lowering in temperature. To know the effect of Cu^{2+} substitution on the mechanism of conduction the resistance data for all samples are plotted in ln(lnR) vs lnT plot as shown in fig.4.6. Linear fit to the plot gives the exponent of eq.3.4. For samples $x = 0.05\&0.1$, the exponent values remain close to ~ 0.9 signifying nearest neighbour hopping at high temperature. The value decreases with lowering in temperature and attains $0.33(x = 0.05)$ and $0.22(x = 0.1)$. The low temperature exponent values remain close to ~ 0.25, so the conduction mechanism adheres to Mott VRH at low temperatures. Bump in the resistance data (see the dotted ellipse in fig.4.6) are seen for all samples in the temperature range $230 - 245$K. Broad minima are obtained at this temperature range in the

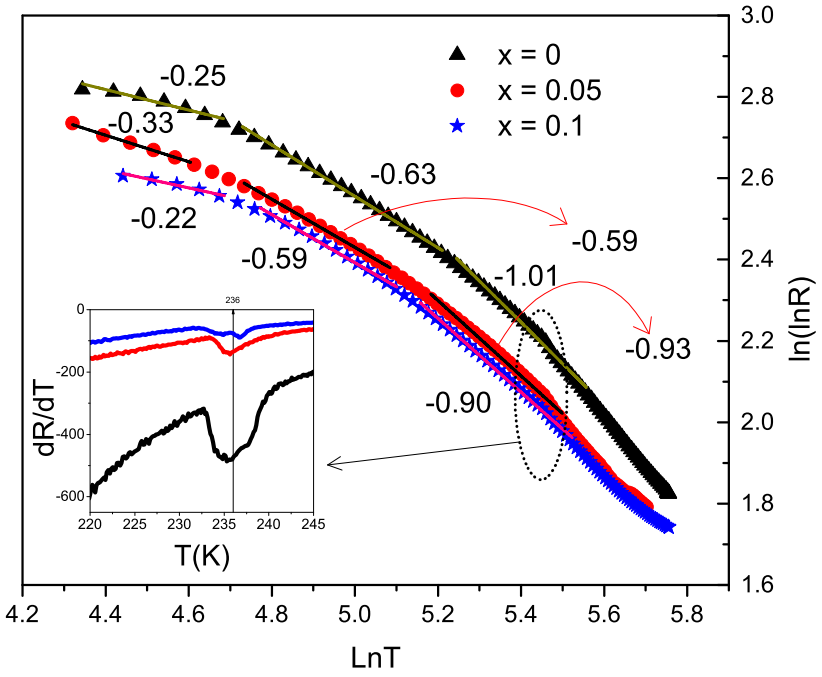

FIGURE 4.6: ln(lnR) vs lnT plot for x = 0, 0.05 & 0.1. Inset represents the corresponding derivative plot of resistance data, showing charge ordering effect.

derivative plot of resistance data. Similar type of anomaly is seen in the resistivity behaviour of Pr_2CoMnO_6 at temperature around $\sim$ 250K, where the authors ascribe the anomaly due to charge ordering[84]. From the derivative plots it is observed that the charge ordering effect minimizes with increase in Cu^{2+} content. The anomaly due to charge ordering represents, the transition from charge active state to a charge localized state.

4.2.3 Dielectric Study

Fig. 4.7a. shows the temperature dependent dielectric constant (ε_r) in the main plot and the loss factor in the inset, for $x = 0$. The plot is usual step like behaviour having dispersionless intrinsic behaviour below 200K. Above 200K, the dielectric value rises with strong dispersion to attain extrinsic plateau, though the plateau region is not seen because it's falling beyond the temperature window. The transition (from intrinsic to extrinsic region) temperature is seen as a peak in the loss plot. This peak position shows a strong dispersion with frequency. A similar

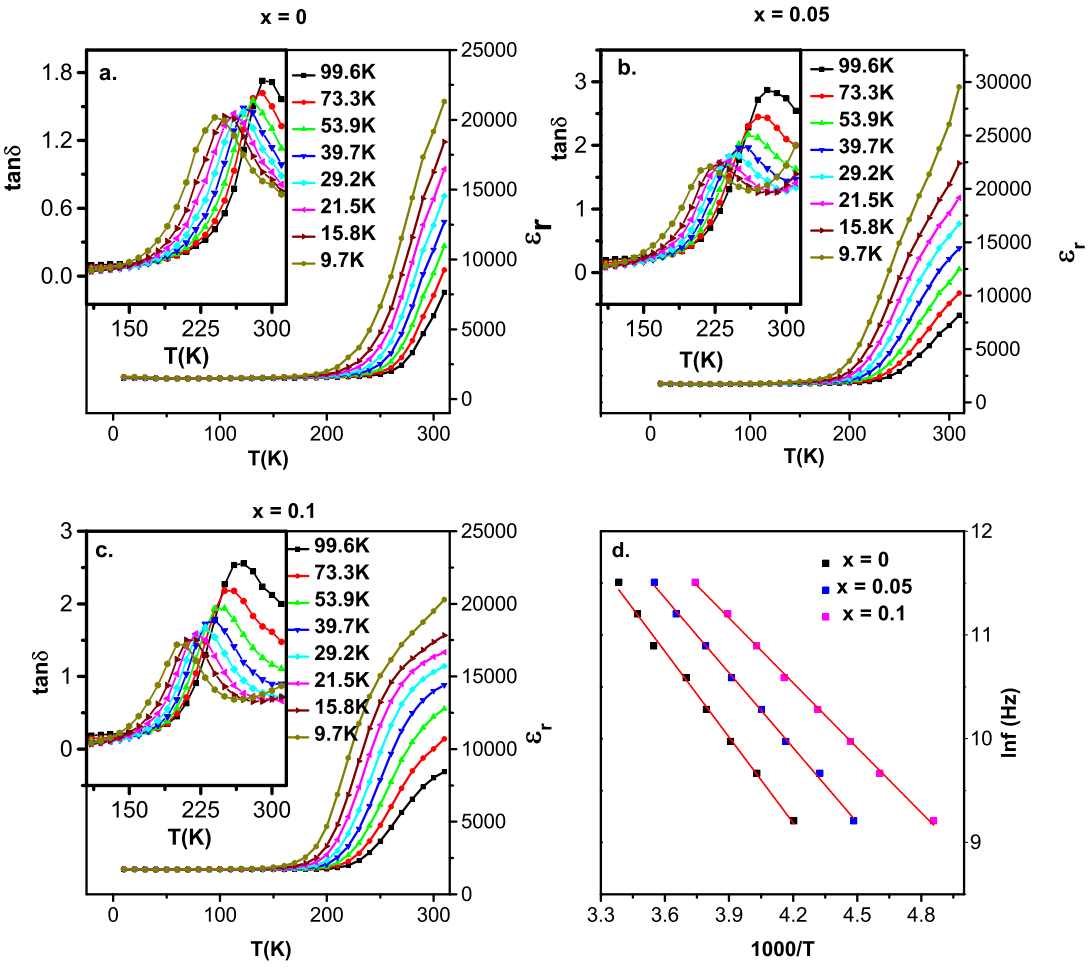

FIGURE 4.7: ε_r vs. T plot for x = 0 (a), 0.05 (b) & 0.1 (c) at various frequencies. The respective insets show the temperature dependency of respective dielectric loss. (d) shows the Arrhenius fit to the dielectric relaxation frequencies.

behaviour is seen for other two samples $x = 0.05$ (see fig.4.7b.) and 0.1 (see fig. 4.7c.), where the entire plot shows a gradual shifting towards lower temperature such that the onset of extrinsic plateau region comes within the temperature window. Because of shifting, the transition temperature and the beginning of intrinsic region also moves to lower temperature. Besides shifting, the intrinsic value of ε_r is found to increase ($\sim$ 1500 for $x = 0$ and $\sim$ 1700 for $x = 0.05$ and 0.1). The measurement frequency as a function of peak position (in temperature) of the loss plots are shown in fig. 4.7d. The plot shows a good fit to the Arrhenius behaviour, where the activation energy obtained from the fit is found to decrease with increasing Cu – content. The decrease in activation energy (E_a) is in agreement with the dielectric loss data, which found to be increasing with Cu content in sample.

	x = 0	x = 0.05	x = 0.1
T_C $R-3c$ phase in K	285	278	270
θ in K	277	270	260
T_G in K	295	281	281
T_C $Pbnm$ phase in K	165	145	145
τ_1 in sec	4111	4045	3482
τ_2 in sec	457	434	300
τ_3 in sec	63	31	20
λ	0.83	0.924	0.944
E_a in meV	237	207	180

TABLE 4.1: Magnetic and electrical parameters for x=0, 0.05 & 0.1.

4.3 Conclusion

We got success in enhancing the much sought $R-3c$ phase in LNM sample via partial substitution of Cu^{2+} in place of Ni^{2+}. This substitution has also enhanced the antiferromagnetic interactions in the sample, and thus variety of magnetic interactions which earlier were not seen properly in the parent sample, are now evident. From the Griffiths phase point of view, strength of Griffiths phase increases with shifting of Griffiths range to lower temperatures. DC resistance as a function of temperature for all samples show hopping nature of conduction with extended hopping at room temperature and transition to Mott VRH at low temperature. Transition due to charge ordering is seen in the temperature range $230-245$K. The charge ordering effect decreases due to Cu^{2+} doping. The dielectric data shows, marginal increase in the intrinsic dielectric value, $1500(x=0)$ to 1700 $(x=0.1)$, but nearly two times rise in the dielectric loss. The partial substitution of Cu, decreases the activation energy for dielectric relaxation, thus the dielectric plot shifts to lower temperature.

Chapter 5

Exotic behaviour of magnetoresistance in the modified La_2NiMnO_6

5.1 Introduction

The field induced change in electrical resistance has always been an important property for the material characterization. It not only has enabled the fundamental understanding to the scattering processes under carrier transport, but also has led to the manifestation of various device applications of modern day technology. In particular, the magnetoresistance effects in magnetic systems have been of special interest due to several exotic properties such as giant magnetoresistance (GMR)[87], tunnelling magnetoresistance (TMR) [87], anisotropic magnetoresistance (AMR)[88] and colossal magnetoresistance (CMR) [89]. These magnetoresistances lays the foundation for the spintronics based devices. The GMR behaviour is realized in ferromagnetic/metal/ferromagnetic (FM/metal/FM) type junctions

Communicated

[26, 90–93], granular ferromagnets [94], alloys [95–97]. The GMR is prone to be affected by the thickness of the metallic spacer layer of FM/metal/FM junction [25]. If the spacer layer is made insulating, the charge carrier cannot pass directly and has to tunnel through the barrier thus giving rise to TMR behaviour in FM/insulator/FM configuration [98]. Several composites [99], multilayer systems [100–102], polycrystalline materials [103] have been found to show TMR effect. The potential of TMR was not realized until the development of MTJ (magnetic tunnel junctions), which is based on the spin polarized tunnelling (a kind of TMR in which the spin of the charge carriers play important role) also seen in some polycrystalline compounds e.g., $La_{2/3}Sr_{1/3}MnO_3$ [104], $La_{0.55}Ho_{0.15}Sr_{0.3}MnO_3$ [105] and $La_{0.7}Ca_{0.3}MnO_3$ [106]. The polycrystalline oxides are liable to exhibit either GMR (when the junctions are more conducting than the grain) or TMR (when the conducting grains are linked via insulating grain boundary) or even both, if mixture of conducting and insulating junctions are present. Thus the polycrystalline material offers a great deal of opportunity for the investigation of underlying physics. Further, with the arrival of nano materials, the effect of coulomb blockade is also expected to play crucial role in determining the magnetoresistances [107, 108].

Although known for several years, only recently the double perovskite oxides have been paid their due attention for their exotic properties such as, room temperature ferromagnetism, half metallicity[6], spin filtering[57], magnetoresistance (MR) and magnetodielectricity (MD). Endowed with many interesting features, the compound La_2NiMnO_6 ($T_C \sim 270K$)[10] have been comparatively less studied. In particular, the biphasic compositions for compounds sintered between 600°C ($Pbnm$) and 1400°C ($R-3c$)[44], is believed to contain many unrevealed phenomenon. Surprisingly most of the researchers have focused their study on single phase compounds only, leaving the biphasic compositions unexplored. Realizing the potential of biphasic compositions, we have focused our study on one such biphasic composition, where nano particles of this compound is studied[55]. The nano form is expected to contain a far more exciting results due to the combination of their intrinsic properties (such as half metalicity, MR, MD, etc.) to the extrinsic property (such as TMR) arising because the nanoparticles are weakly linked via their

surface atoms. As the nanoparticles have very large surface to volume ratio, these weak link based properties are expected to protrude significantly.

Here we present a very interesting MR behaviour of modified La_2NiMnO_6. By virtue of modification, the MR behaviour of La_2NiMnO_6 has changed drastically and enhanced significantly. Modification induced changes in MR behaviour is not unusual; for instance the conventional negative MR of Sr_2FeMoO_6 changes to a large positive MR for the sample prepared via wet chemical method [109]. Composition driven changes has also been found to affect the magnetotransport behaviour [110, 111]. Manipulation of grain boundaries has been found to greatly affect the magnetotranport behaviour[112]. In this chapter, we present a unique method to tailor the biphasic composition, which we believe may be extended to other compounds as well, so that new physics may be explored.

5.2 Results and Discussion

5.2.1 Magnetization Study

The temperature dependence of magnetization under 0.01T magnetic field, for the zero field cooled (ZFC) and field cooled (FC) protocol is plotted in fig.5.1. For the reference purpose, the magnetization data of LNM is also plotted in the inset. The magnetic transition of $R-3c$ phase, seen at 280K in the case of LNM, is now suppressed for M-LNM. This suppression is due to the reduction in the volume fraction of $R-3c$ phase, which is confirmed from the xrd result. The sharp rise in the magnetization at $\sim$ 200K and saturation at lower temperatures is due to the *Pbnm* phase. It should be noted that this saturating behaviour is absent for LNM. Further, a clear bifurcation in the ZFC and FC data seen for the LNM, is reduced to a great extent for M-LNM. Moreover, the ground state magnetization (extrapolated till T = 0) for M-LNM has also increased to 6emu/gm compared to 2.8emu/gm in case of LNM. These features are indications that the magnetic frustrations prevailing in the LNM sample, has reduced to a great extent

in M-LNM. Also, as in LNM, here too we found signatures of Griffiths phase with $T_G = 290K$ but with reduced $\theta_P = 230K$, probably due to the reduction in $R-3c$ phase. One more feature which is of utmost importance in the pretext of present discussion, is seen at $T < 150K$. While going down the temperature scale, the ZFC plot after an initial rise at 200K, shows a consistent downfall for $T < 150K$: a behaviour reminiscent of antiferromagnetic like arrangement of magnetic moments. However, this downfall is replaced by a saturated behaviour in the FC data. It thus reflects the opposite arrangement of magnetic moments under normal conditions and this arrangement turns to parallel in the presence of external magnetic field. The isothermal magnetization data (fig.5.2) collected at static temperatures 250K,

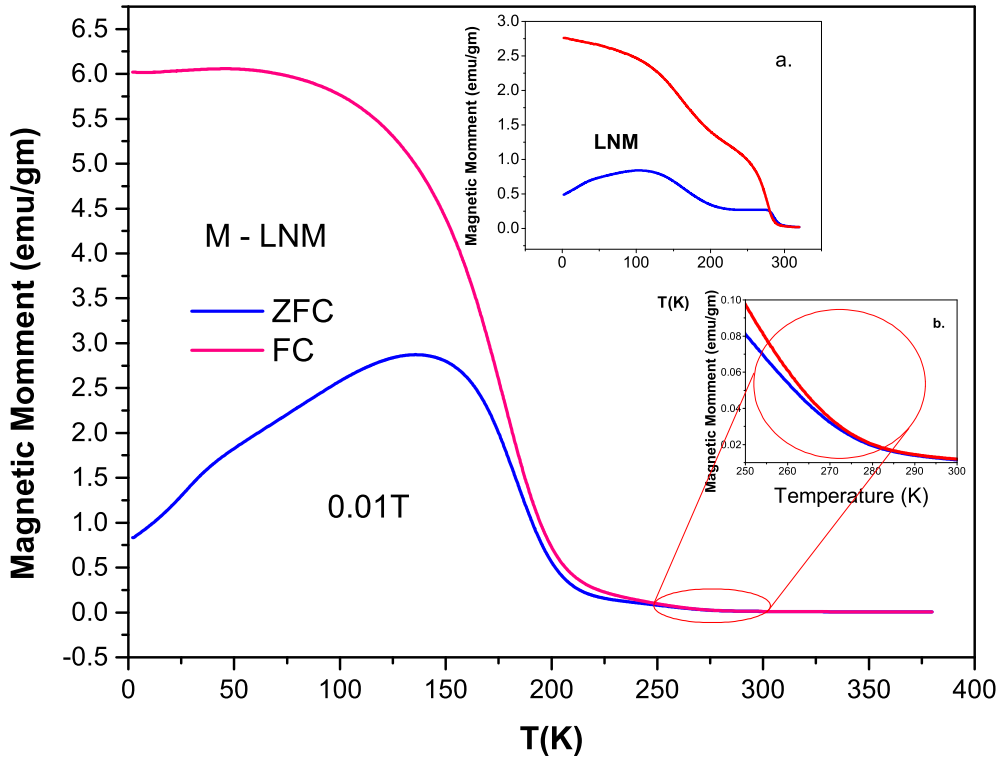

FIGURE 5.1: $M \sim T$ data for M-LNM recorded in ZFC and FC formalism. Inset (a) shows the corresponding magnetization data for LNM. Steep rise and initialization of bifurcation in the magnetization (shown in inset (b)) $\sim 270K$ marks the ordering of $R-3c$ phase.

200K, 150K, 100K & 50K, shows ferromagnetic behaviour of M-LNM. As the temperature is lowered, increase in the saturation magnetization as well as the coercive field (see inset fig.5.2a.) is observed. This supports the strengthening ferromagnetic behaviour with lowering of temperature.

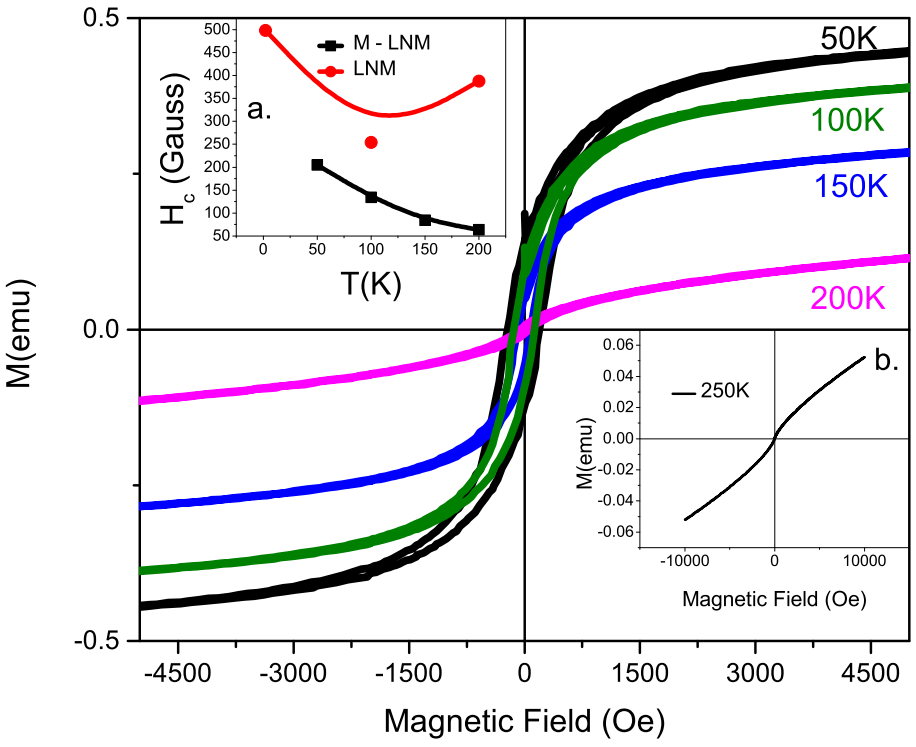

FIGURE 5.2: $M \sim H$ plot for M-LNM taken at various temperatures, shows increasing FM contribution at lower temperatures. The 250K data is plotted separately (inset b) for better clarity. Inset (a) shows the variation of coercivity with temperature for the two samples.

5.2.2 Magnetoimpedance Study

The impedance data is plotted in the Cole-Cole formalism. Each data at designated temperature is acquired under isothermal conditions by varying the frequency in "without" and "with" 1T magnetic field conditions. Some of the selected temperatures data are shown in fig.5.3(black square: without field, red circle: with field). Each semicircle represents a particular dielectric relaxation, which in our earlier report were found to be due to $R-3c$ and $Pbnm$ phases respectively[55]. The zero field and 1T data at 298K completely merge with each other resulting in negligible magnetoimpedance (MI). As the temperature is lowered, the with-field data starts deviating from the zero-field data. For LNM, the with-field semicircles are of increased radius, as compared to zero-field semicircles, thus implying a positive MI. This positive MI shows substantial rise on lowering of temperature.

On the other hand, for M-LNM sample, the with-field semicircles are quite suppressed from the zero field semicircles and this suppression keeps on increasing as

the temperature is lowered. This signifies the negative MI for this sample. So it is quite intriguing that how a slight modification of LNM sample leads to a giant and contrasting behaviour of MI. In order to understand the responsible mechanisms; the impedance data needs to be further resolved. Thus the experimental data are fitted to the Harverliak - Negami (HN) model as described earlier [34]. The solid green lines represent the fit of the zero field data and that in blue represent the fit to 1T field data. The radius of the semicircle represents the resistance (R) of the individual phases. From the fit, the respective resistances of $R-3c$ phase (R1) and $Pbnm$ phase (R2) are obtained in the zero-field and with-field (1T) conditions.

The magnetoresistance (MR) in percent is obtained using the relation

$$MR(\%) = \left[\frac{R(H) - R(0)}{R(0)}\right] \times 100 \tag{5.1}$$

Both samples (LNM & M-LNM) displays two resistance values corresponding to two relaxations, which we had earlier ascribed to the two crystallographic phases viz. $R-3c$ and $Pbnm$. This time, measurement is done in a wider frequency spectrum upto 1MHz as compared to earlier study of 100kHz, and thus a more clear picture is obtained. The temperature dependence of MR is shown in fig.5.4. For LNM (see top panel of fig.5.4) at room temperature, only MR1 could be measured and an apparent MR2 could not be obtained until 260K. The MR1 starts with nearly zero value at room temperature and while decreasing temperature, shows a bit of fluctuation till 270K, which happens to be the T_C for $R-3c$ phase. Below 270K the fluctuation settles down and the MR1 rises monotonously till 170K to a peak value 33%. On further cooling, MR drops suddenly to 10% and stays there till 160K, temperature of lowest measurable MR1. On the other hand, MR2 differs from MR1 and starts with a negative value of 5% at 260K. On cooling, the difference between MR1 and MR2 narrows down and MR2 closely follows MR1. Contrary to MR1, the MR2 could be measured till the lowest temperature of measurement 100K with a value 15%. The observed behaviour of MRs obtained

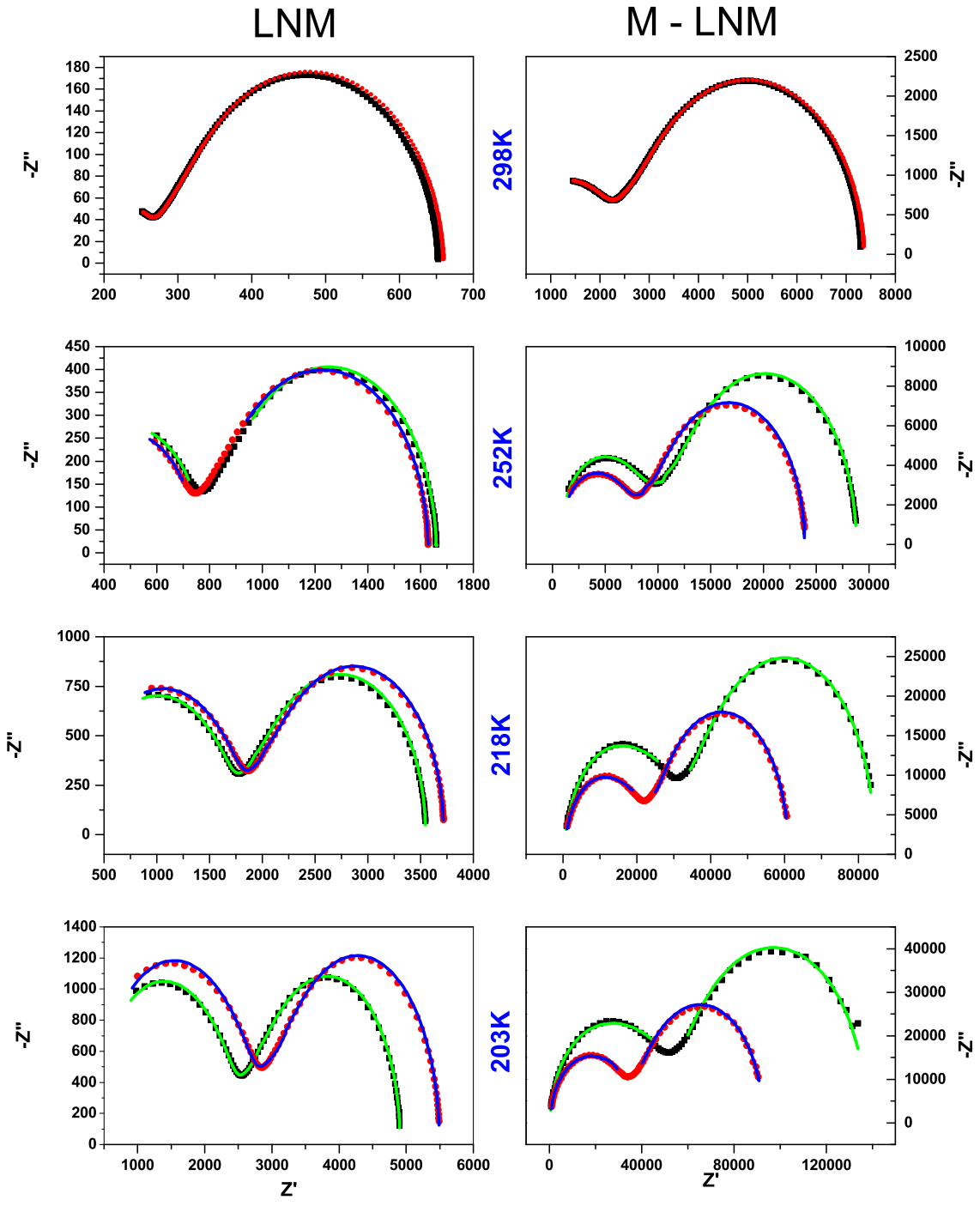

FIGURE 5.3: Cole-Cole plots under with (red circle) and without magnetic field (black square) conditions. The left pane represent the data for LNM and right pane represents the data for M–LNM.

in wider frequency range, suggest that the earlier proposition of R1 & R2 belonging to the two crystallographic phases, is still intact.

A very different behaviour of MR (see bottom panel of fig.5.4) is seen for M-LNM sample. At room temperature, MR starts with zero value and on decreasing the

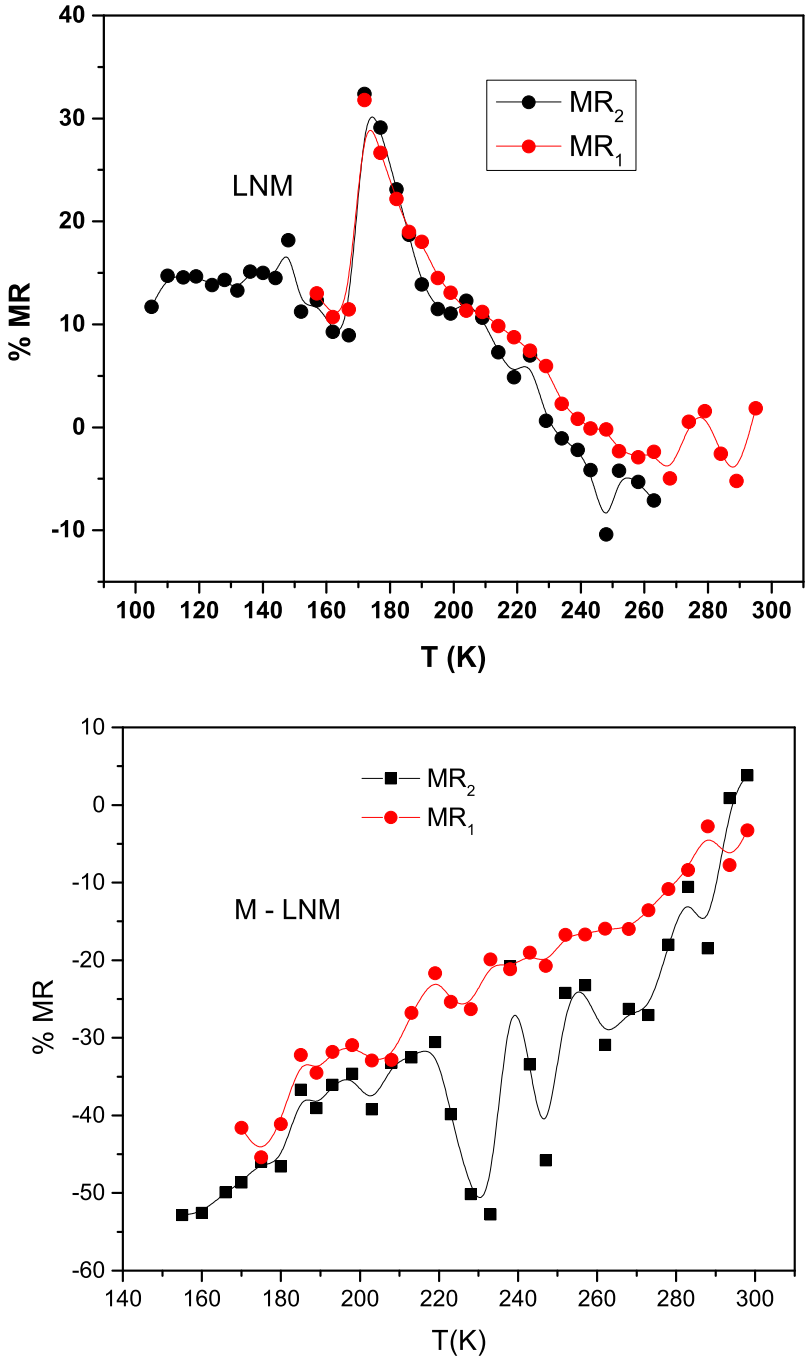

FIGURE 5.4: Temperature dependence of MR obtained from the Cole-Cole plot for (a) LNM (top panel) (b) M-LNM (bottom panel). MR2 & MR1 stands for the magnetoresistance of $R-3c$ and Pbnm phases respectively

temperature, it monotonously increases in the negative scale, to attain a value of -53% at 155K (lowest temperature at which resistance values could be obtained from the Cole-Cole plot). The behaviour indicates that, there is possibility of further enhancement of negative MR at lower temperatures. Coming to the two

respective magnetoresistances, here both MR1 and MR2 could be measured at room temperature. As the temperature is lowered, MR1 decreases with fluctuation. The fluctuation settles down at 220K, and the value continuously increases to -53% at 155K. From the magnetization plot, 220K is the region at which *Pbnm* phase starts ordering, thus we associate MR1 to the *Pbnm* phase. Similarly MR2 also shows decreasing trend with lowering temperature, but here the data is free of fluctuation. This is probably because, the $R-3c$ phase orders at higher temperature 270K. To have a deeper insight on the contrasting MR behaviour of the two samples, we performed $I \sim V$ (current – voltage) measurements at various temperatures.

5.2.3 Conductance Study

For the sake of comparison of the data to the existing theoretical models, the $I \sim V$ data is plotted as conductance 'dI/dV' vs. voltage 'V' in fig. 5.5. Starting with LNM, the 300K conductance plot resembles 'U' shape with a dip at the center. As the temperature is lowered, the near zero voltage curvature dominates the plot, such that below 200K, only central dip behaviour is present. Such behaviour (except the dip) of conductance is an indication of tunnelling behaviour of charge carriers through potential barrier. The dip region is found to obey $dI/dV \propto V^x$ with 'x' values close to 1. The value of $x = 1$ is a possible indication of tunnelling influenced by weak links due to shunt resistances. Thus it looks like as if the barrier is not perfectly insulating. Similar behaviour of conductance was observed in Cr_2O_3/CrO_2 composite by Coey *et.al.*,[113] where the authors tried to quantify the barrier height by fitting the relation

$$\sigma = \sigma_\infty exp[-(E_C + E_M)/eV] \tag{5.2}$$

slightly away from V = 0 region. Here E_C is the electrostatic energy required to generate a pair of positively and negatively charged grains. E_M is the additional energy required when the grains are ferromagnetic. Following ref.[113], we too tried to fit the conductance data via above mentioned expression. The $E_C + E_M$ value

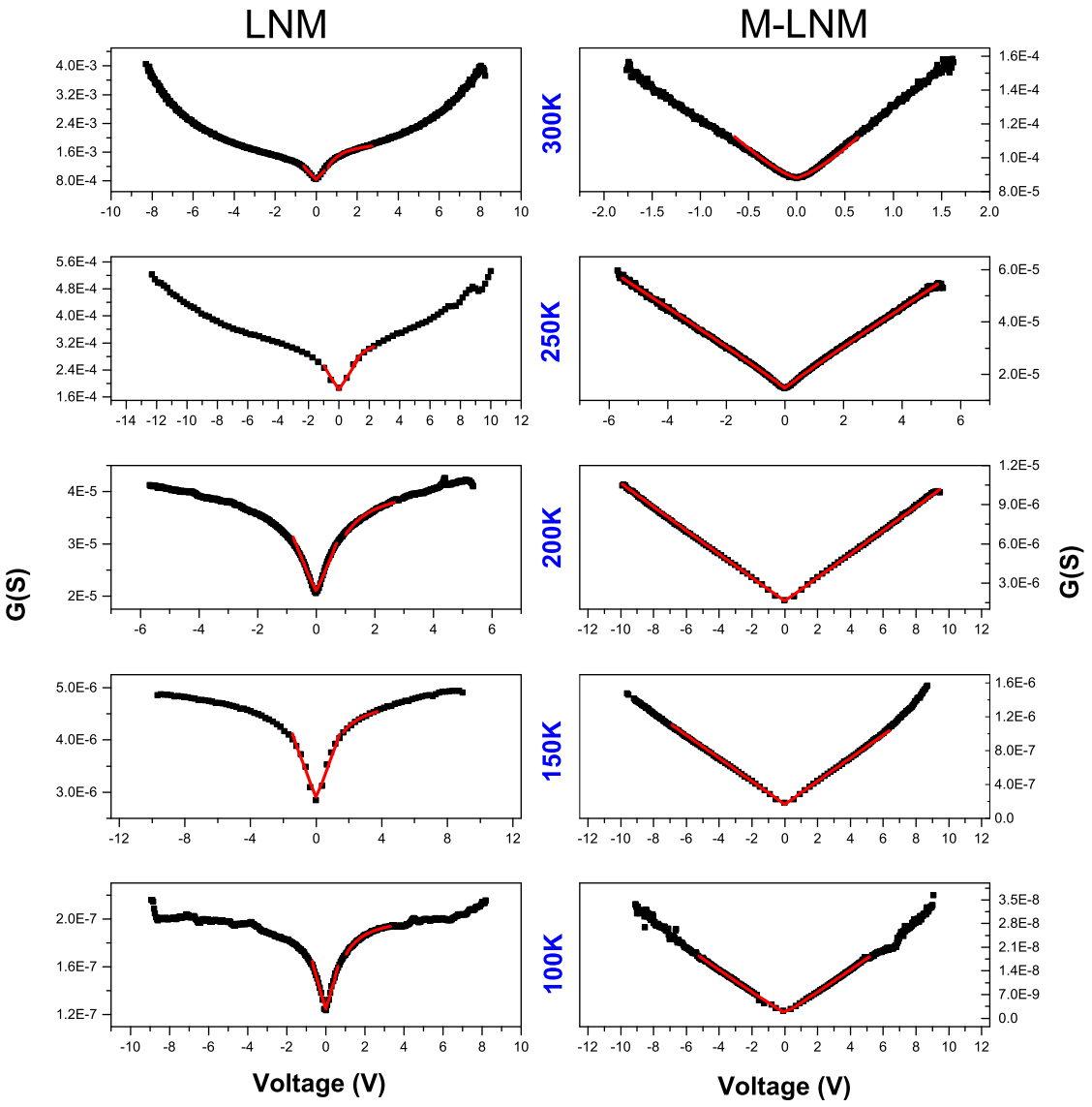

FIGURE 5.5: $dI/dV \sim V$ data for both the samples. The left pane represent the data for LNM & right pane for M − LNM samples.

shows a monotonic decrease with decrease in temperature and below 150K the fall is rapid (see fig. 5.6). This is consistent with the model, which proposes $E_M = 0$ for unidirectional ferromagnetic alignment. The sharp drop is in accordance with the observation of ferromagnetic state for both the phases i.e, $R-3c$ and $Pbnm$ for $T < 150$K.

On the other hand, a different behaviour of conductance is seen for M-LNM sample. Starting from 300K down to 100K, the conductance value increases monotonically with voltage. In terms of mathematical expression, $G \propto V^x$. The exponent $x \sim 2$

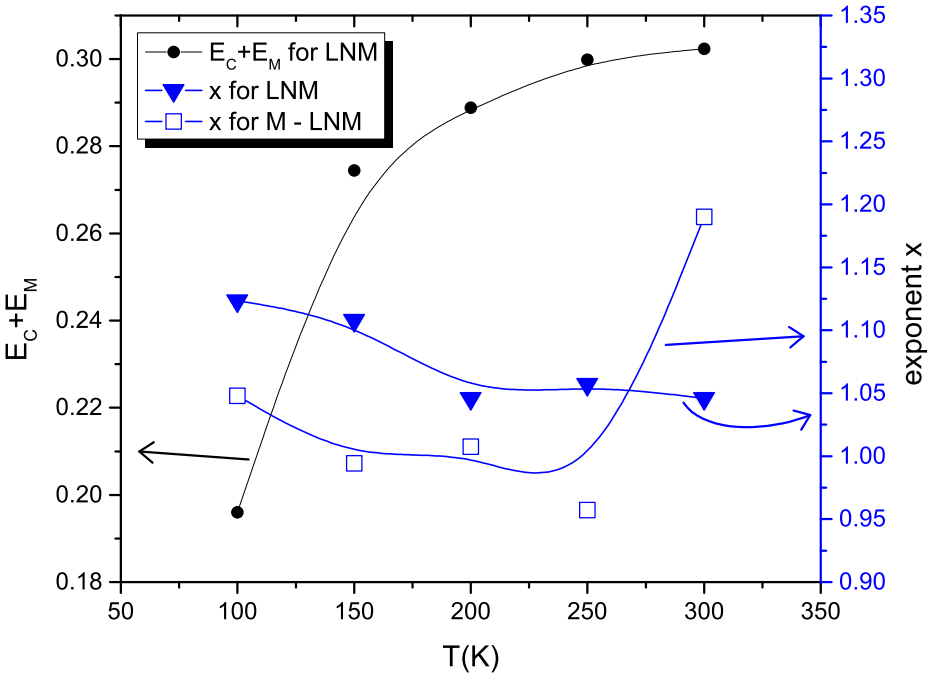

FIGURE 5.6: Temperature dependent energy gap ($E_C + E_M$) for spin polarized tunnelling. The right axis represents the exponent 'x'.

satisfies the conditions for direct tunnelling limit[114] and $x = 0$ corresponds to ohmic nature. The value observed in our case is in between that for tunnelling and ohmic. A similar fractional value of 'x' has been found in LCMO manganites[115] and YBCO/LCMO/YBCO trilayers[116].In their theoretical studies, Glazman and Matveev[117] shown that if the conductance G is governed by inelastic tunnelling via pairs of localized states, then $G \propto V^{4/3}$. The value of 'x' seen in this case is not exactly 4/3 and is slightly lower. However our results are somewhat closer to that observed by Ziese *et. al.*,[115], where the author have retained the picture of Glazman and Matveev but the lower values are ascribed to the presence of many tunnelling junctions and shunt resistances in the insulating boundary. The other prediction of Glazman and Matveev, $G \propto V^{4/3}$, is difficult to verify because the temperature range under investigation is dominated by multiple magnetic transitions.

It thus suggests that in *Pbnm* phase (which is dominant in M-LNM), the conductance is highly influenced by the presence of tunnelling junctions and shunt resistances. This might have some relation to the lower crystallizing temperature

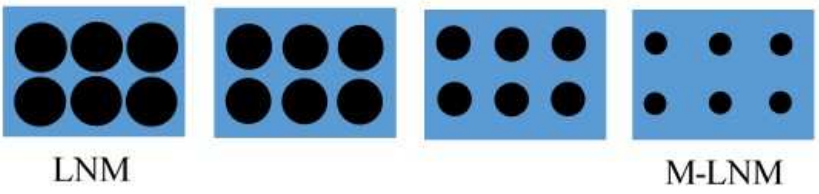

FIGURE 5.7: Evolution of $R-3c$ and $Pbnm$ phases in the sample. Black circles mark the $R-3c$ phase and blue regions mark the $Pbnm$ phase.

for $Pbnm$ phase, compared to $R-3c$. Here no indication of barrier/gap is seen, even at temperature as low as $100K$.

Based on these observations of dI/dV, we propose that in M-LNM, where $Pbnm$ is the major phase, the $Pbnm$ grains are connected to each other via more conducting shunt resistances with $R-3c$ phase embedded as island in the $Pbnm$ matrix (see fig.5.7). On the other hand, in LNM the $R-3c$ grains are connected via a thin layer of $Pbnm$ phase, which are acting as weak links between the $R-3c$ grains. The $Pbnm$ phase probably nucleates at the grain boundary and with increasing percentage, grain boundary becomes thick, isolating the islands of $R-3c$ phase. A proposed steps of phase evolution is shown in fig 5.7.

5.2.4 Isothermal DC Magnetoresistance Study

To address the physical processes responsible for such an exotic behaviour of MR, the magnetoresistance is measured using DC method as well. The DC MR data is collected by sweeping the magnetic field for the increasing and decreasing cycle in both forward and reverse direction of magnetic field. The isothermal MR vs H measurements are done at few selected temperatures seemed important: (1) 250K, $R-3c$ phase entered ferromagnet state (2) 200K, $Pbnm$ starts ordering (3) 150K, ordering temperature of $Pbnm$ phase (4) 100K, both the phases have ordered ferromagnetically. Before each isothermal measurement, the sample is heated to room temperature (paramagnetic state), in order to wipe off any ferromagnetic history. The left pane of fig.5.8 shows the MR data for LNM and right pane shows the data for M-LNM. The 250K data for LNM show dips at the positions of coercive field, obtained from the M-H measurement. These dips are observed in the

increasing cycle of magnetic field for both forward and reverse directions of H. This behaviour is an indication of spin polarized tunnelling through paramagnetic interface between two ferromagnetic neighbourhood entities. It is appropriate at this juncture to mention the findings of Li *et.al.,* [118], according to which, it is difficult to distinguish between spin polarized tunnelling and scattering, just from the behaviour of MR data, and only a dI/dV vs. V plot can do this. From the dI/dV vs. V measurement (discussed earlier), the presence of tunnelling mechanism is already confirmed. Hence, in our discussion, we will use " spin polarized tunnelling " to explain our MR data. On either side of the dip, the MR increases and attains a maximum of $\sim$ 1%. The spin polarized tunnelling effect is more pronounced at 200K as seen in fig.5.8b. The 200K data show a prominent dip near zero field and the MR value increases upto 10% on either side of the zero field data. The MR value is saturated above 0.5T of magnetic field. A small hysteresis is also seen between the field sweep direction. According to the magnetization plot, this temperature is dominated by the ferromagnetic $R-3c$ phase. At 200K the ferromagnetic components are more ordered, hence the spin polarized tunnelling is more favourable through the paramagnetic interface. The behaviour of MR is similar to that of $Ni_{70}Ag_{30}$ alloy [94], where the majority magnetic Ni are separated by minority non-magnetic Ag: a picture similar to that proposed in fig 5.7. Further lowering of temperature to 150K (see fig.5.8c.) displays the MR behaviour containing mixture of peaks and dips, but reproducible for both directions of magnetic field. This temperature corresponds to the ordering of *Pbnm* phase in LNM sample. The *Pbnm* phase becomes ferromagnetic below 160K, so the paramagnetic interface (which is actually *Pbnm* phase at higher temperature) is absent for spin polarized tunnelling to takes place. Hence at 150K a very negligible MR is observed. However the MR value oscillates between positive and negative value representing a transition like region. The sharp drop in MR value in fig.5.4 at 170K, also corroborates the fact that the change in magnetic state largely affects the MR value. At 100K, the MR data is hassle free and displays a negative MR of -10%, with small positive peaks at the position of coercive field. The 100K MR data in fig.5.8d. is more like a typical ferromagnet. This is supported from the

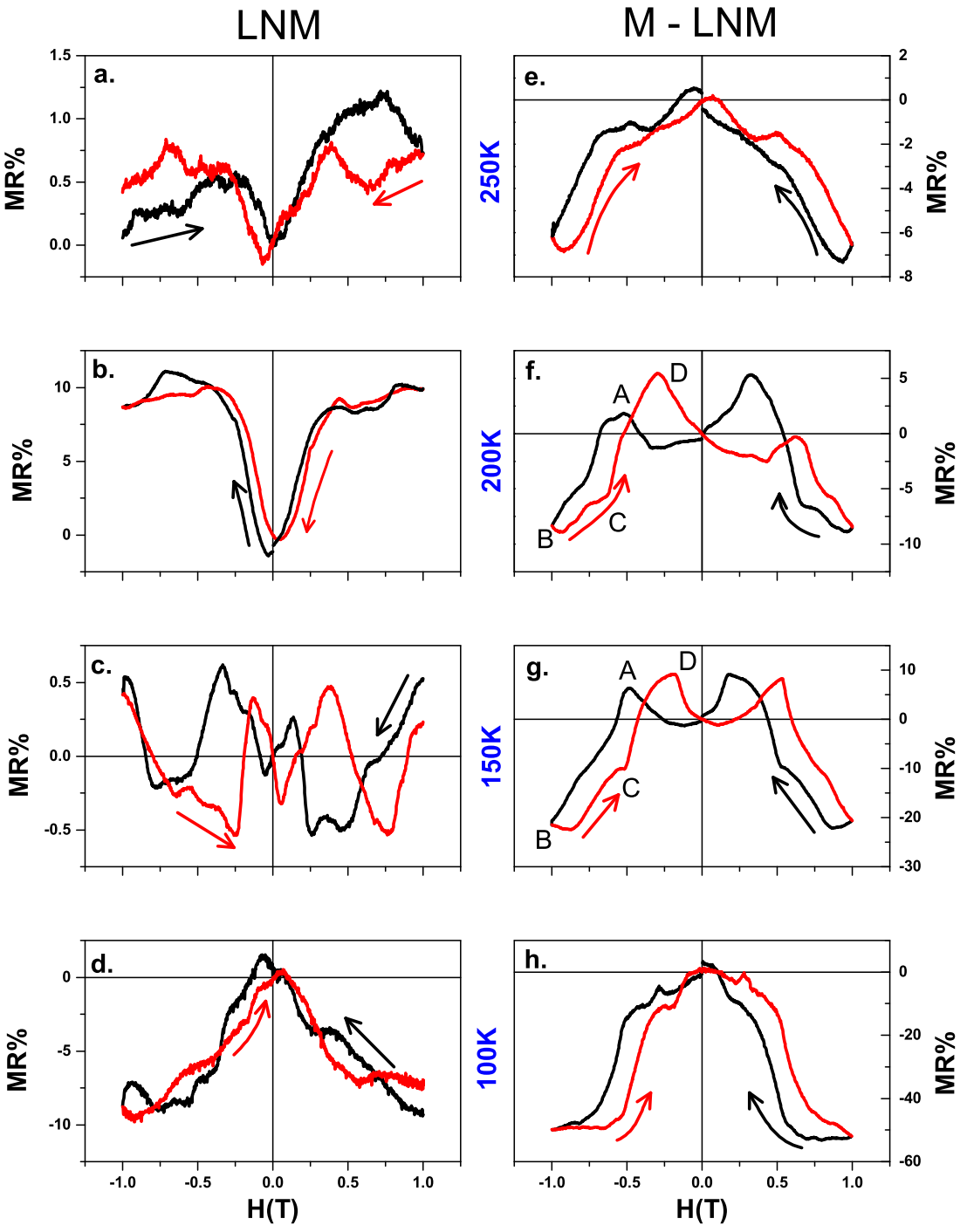

FIGURE 5.8: Isothermal DC MR data for the two samples: LNM on the left (a-d) and M-LNM on the right (e-h).

fact that at 100K both $R-3c$ and $Pbnm$ phases are in the ferromagnetic state. The highest resistance state i.e., the peak in MR data is observed around the zero magnetic field.

The DC MR behaviour of M-LNM shows a different behaviour than LNM (see

fig.5.8e.,f.,g.,h.). The 250K data shown in fig.5.8e. have slight positive maxima positioned at the coercive field values, followed by a monotonous decrease to -2% at 0.4T. From 0.4 to 0.75T, the MR remains flat and then decreases sharply to a value of -7% at 1T. In the decreasing cycle, a different path is adopted by the MR values with a small hump at $\sim$ 0.6T before reaching the origin, thus creating a hysteresis in the plot. In the forward sweep, the same behaviour is reproduced. On lowering the temperature to 200K (see fig.5.8f.), the MR starts with a negative value. The flat region in previous case changes to a peak valued 2.5% and positioned at $\sim$ 0.5T (say A). With further field increase (negative), the MR drops sharply to -8.5% at 1T (say B). While decreasing cycle, the MR rises monotonously till 0.5T (say C) and then rises sharply to peak at 0.3T with a value $+5\%$ (say D), before reaching the origin.

Like previously, this behaviour is reproduced in the forward direction of magnetic field as well. At 150K (see fig.5.8g.), feature becomes sharper where the peaks 'A' and 'D' takes the values 5% and 10% respectively. The peak 'D' moves to lower field of 0.25T. At 100K, the behaviour becomes completely different, reminiscent of a double step transition of MR: first to -10% at 0.5T and then -50% at 1T. Like previously, here too a hysteresis is seen in the return cycle.

At 250K, the temperature is close to the Tc of $R-3c$ phase. Hence the ferromagnetic ordering of $R-3c$ domains is hindered by the thermal fluctuations, which can be suppressed by the external magnetic field. Fig.5.8(b) shows that, the MR of LNM saturates at $\sim$ 0.5T, indicating that the ordering is maximum at 0.5T. Hence the initial drop in MR of 5.8(e) till 0.5T shows reduction in electron's scattering due to field induced magnetic ordering within the grain. The MR remains stagnated even beyond 0.5T (till 0.75T) because the ordering within grain is at its best. The ferromagnetically ordered $R-3c$ domains are separated by thick paramagnetic $Pbnm$ phase and thus the establishment of long rang ordering of $R-3c$ phase is hindered. Fields greater than 0.75T helps in establishing the long range ordering so that all grains align along the field direction. This further minimizes the scattering of spin polarized tunnelling and the MR drops very sharply for fields beyond 0.75T.

From here on wards, help of the recently mooted theory of reverse metamagnetic transition [119–122] is taken, to explain the observed MR behaviour. According to this theory, the MR is due to the scattering of conduction electrons at the domain boundary of two ferromagnetic regions of different strength. In fig.5.8f, the stagnated region (of fig.5.8e) has converted to a peak (position A) for the increasing field and this peak is shifted to position D, while decreasing field, leaving a hump (position C) exactly below position A. At 200K, the $R-3c$ is almost fully ordered and ferromagnetism in $Pbnm$ phase is in initial stages. Hence, it is quite logical to consider that $Pbnm$ should respond to the dipolar field of $R-3c$. However, had that been the case, such behaviour of MR might have appeared in LNM sample as well, where $R-3c$ phase is in abundance. From the magnetization data (fig.5.1), we found that the ground state magnetization for $Pbnm$ is way too large compared to $R-3c$ phase. Thus at 200K, though the nucleation of ordered $Pbnm$ has started, its magnetic strength is more than that of $R-3c$ phase and thus controls the $R-3c$ phase via dipolar field. The ferromagnetic $Pbnm$ phase induces a dipolar field [123] on the $R-3c$ phase, causing it to order opposite to that of $Pbnm$. Thus the peak in MR at 0.5T (position A), is a manifestation of large scattering of conduction electrons due to oppositely oriented $R-3c$ and $Pbnm$. Further increase of field causes both the ferromagnetic components i.e., $R-3c$ and $Pbnm$ to align along the field direction, thus a sharp drop in MR (position B). Once the entire sample has ordered ferromagnetically, the sample is guided by ferromagnetic exchange interaction J_F. Being a ferromagnetic sample, the ferromagnetic exchange J_F is stronger than the dipolar exchange J_D. Hence in the return cycle, where the magnetic ordering is guided by J_F, the $Pbnm$ & $R-3c$ domains does not order oppositely and only a small kink is seen at position C, marking the tussle between comparable J_D and weakened J_F. Maximum scattering of conduction electron happens at position D, where J_D again aligns the two phases oppositely. On further lowering of field, the J_D is weakened by the thermal fluctuation, and the domains rearrange themselves in the minimum energy configuration, leading to zero MR position. At 150K (fig.5.8g.), a similar behaviour of MR is observed, with only difference that the peaks and transitions are sharper

and bigger. This observation supports our explanation, because stronger magnetic domains is supposed to interact strongly.

The 100K data (fig.5.8h.) is different from the other temperatures data because here the entire sample is in ferromagnetic state and there is no boundary between the ferromagnetic domains. The MR data is reminiscent of two ferromagnetic components, ordering at different field strengths. The highest resistive state is at the zero field and a large (50%) drop in resistance is obtained on applying 1T field.

5.3 Conclusion

M–LNM is prepared by impregnating LNM pellets. Enhancement of *Pbnm* phase fraction with suppression of $R-3c$ phase is confirmed from the Rietveld refinement of XRD data and in corroboration with DC magnetization. Contrasting magnetoimpedance behaviours comprising positive magnetoimpedance for LNM and negative magnetoimpedance for M–LNM is seen. Magnetoresistance is calculated from the fitting of zero field and with field impedance data to the Harverliak – Negami equivalent equation.

With the decrease of temperature, the magnetoresistance for LNM shows gradual increase with peak value of 33% at 170K and dropping sharply to 10%, on further lowering of temperature. The drop in magnetoresistance below 170K is ascribed to the ferromagnetic state of both the phases. The conductance vs voltage analysis predicts the tunnelling of charge carriers through the insulating barriers, as the conduction mechanism. The barrier height $\mathrm{E}_C + \mathrm{E}_M$ (0.30 at room temperature) decreases steeply to 0.19 below 150K: temperature where both $R-3c$ and *Pbnm* phases are in ferromagnetic state.

On the other hand, in M–LNM, the magnetoresistance (calculated from magnetoimpedance) of both the phases, increases in the negative scale as temperature is lowered. A maximum magnetoresistance of -53% is achieved at 155K. The power

law fit to the conductance vs voltage data shows conduction through shunt resistances for M–LNM. The magnetoresistance behaviour at various static temperatures viz., 250K, 200K, 150K & 100K shows the signature of inverse metamagnetic transition originating due to the dipolar field of $Pbnm$ phase on $R-3c$ phase.

In summary, based on the magneto-conductance behaviour of LNM, a pictorial model of the biphasic LNM is presented (fig.5.7), according to which, in M-LNM where $Pbnm$ is the major phase, the $Pbnm$ grains are connected to each other via more conducting shunt resistances with $R-3c$ phase embedded as island in the $Pbnm$ matrix. On the other hand, in LNM the $R-3c$ grains are connected via a thin layer of $Pbnm$ phase, which are acting as weak links between the $R-3c$ grains. The $Pbnm$ phase probably nucleates at the grain boundary and with increasing percentage, grain boundary becomes thick, isolating the islands of $R-3c$ phase.

Chapter 6

Gas Sensing Application of La_2NiMnO_6

6.1 Introduction

LNM satisfies its true multifunctional nature by showing physical properties like colossal magnetoresistance (CMR)[6], colossal magnetodielectricity (CMD)[8], half metallicity and room temperature ferromagnetism[6, 8]. Its prospect as application oriented devices includes magnetodielectric capacitor, spin based sensors, multiple state memory elements and spin tunnelling junctions. The above applications are predominantly based on the magnetic properties of LNM. In this chapter, we have explored a new direction in its functionality i.e its application as gas sensor. The electrical conduction is found to be sensitive to gaseous environments as well as concentration. The gases adsorb at the electrode interfaces and at the grain boundaries constituting the space charge. The space charge greatly affects the electrical resistance of the sensor[124]. We have investigated the electrical conduction mechanism via impedance spectroscopy. Impedance measurement is preferred

AIP Conf.Proc.**1665**, 140050(1-3) (2015).

over the D.C. resistance measurement because under appropriate conditions various contributions from bulk, grain boundary and space charge can be resolved. The gas sensing property is investigated under different gaseous environments (O_2, N_2 and Ar) with varying concentration of gases.

6.2 Results and Discussion

The real (Z') and imaginary (Z'') component of the impedance are plotted in Nyquist plot. In this way various relaxing components such as grain, grain boundary and interface (due to space charge) may be separated out. Each relaxing component exhibits a semicircle whose radius represents the resistance of the individual component. Fig. 6.1& 6.2 show the Nyquist plot of LNM at room temperature for various gas (Argon, Oxygen, Nitrogen) concentrations. The black arrow in figure represents the direction of increasing gas concentration. For all the gases, a single semicircle is seen for minimal gas concentration and the radius of the semicircle increases with increase in concentration of gas. Increase in the radius of semicircle is the representation of increase in the resistance of LNM. Each semicircle is fitted to an equivalent R || C circuit model, where the real and

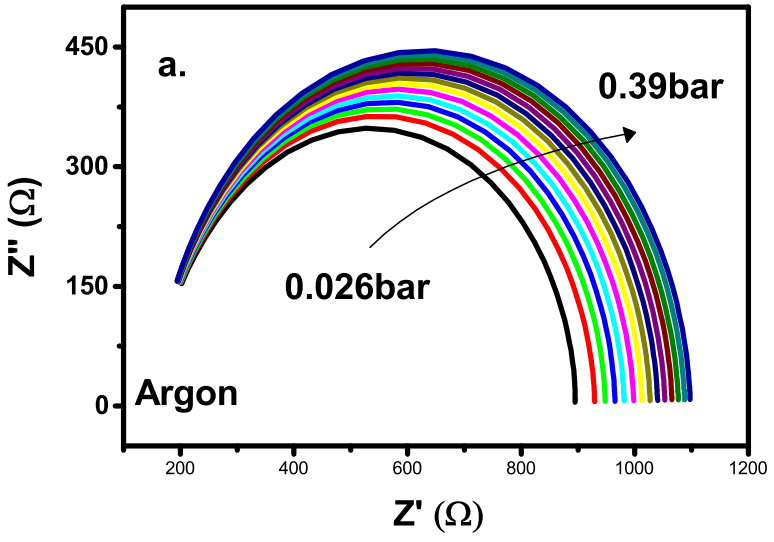

FIGURE 6.1: Nyquist plot for LNM at different concentrations of Argon.

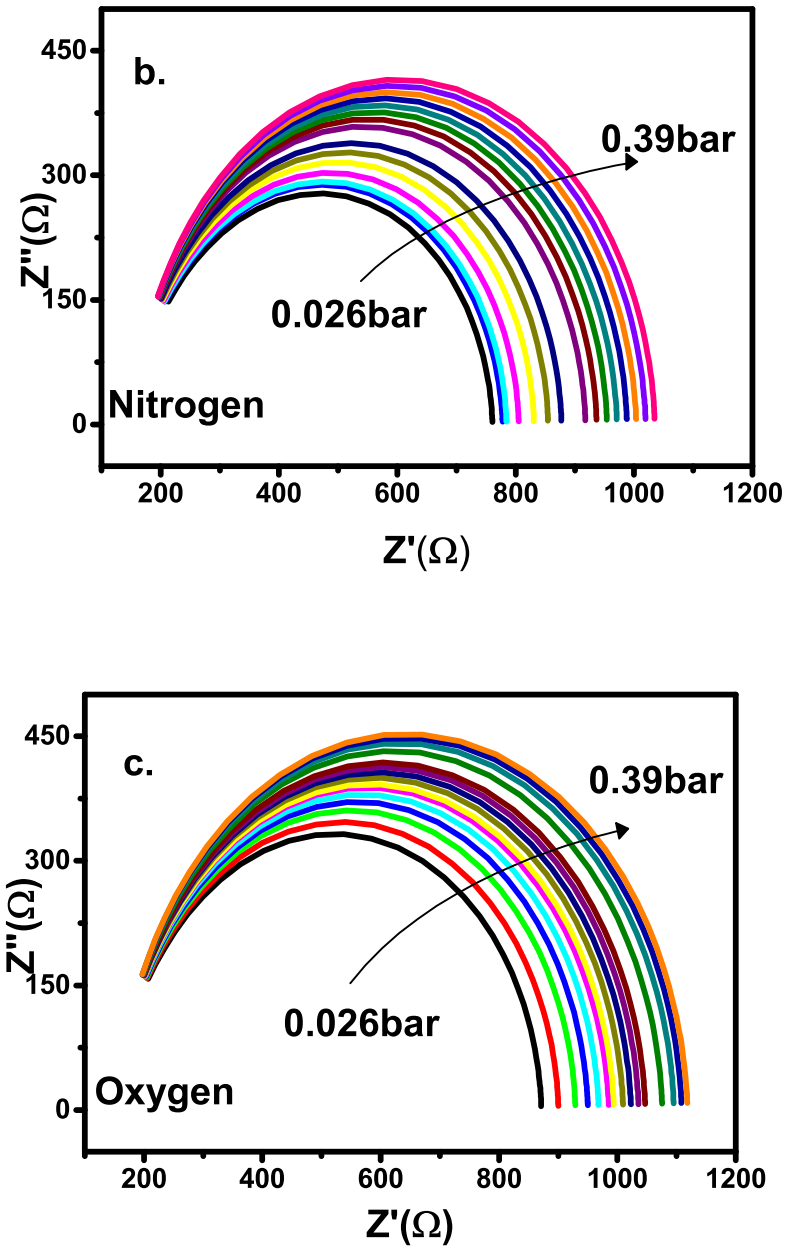

FIGURE 6.2: Nyquist plot for LNM at different concentrations of Nitrogen (top panel) and Oxygen(bottom panel).

imaginary parts of impedance are related by the expression in equation 6.1.

$$(Z'')^2 = \left(\frac{R}{2}\right)^2 - \left(Z' - \frac{x}{2}\right)^2 \tag{6.1}$$

Here $Z^{'}$, $Z^{''}$ are the real and imaginary parts of impedance and R is the resistance,

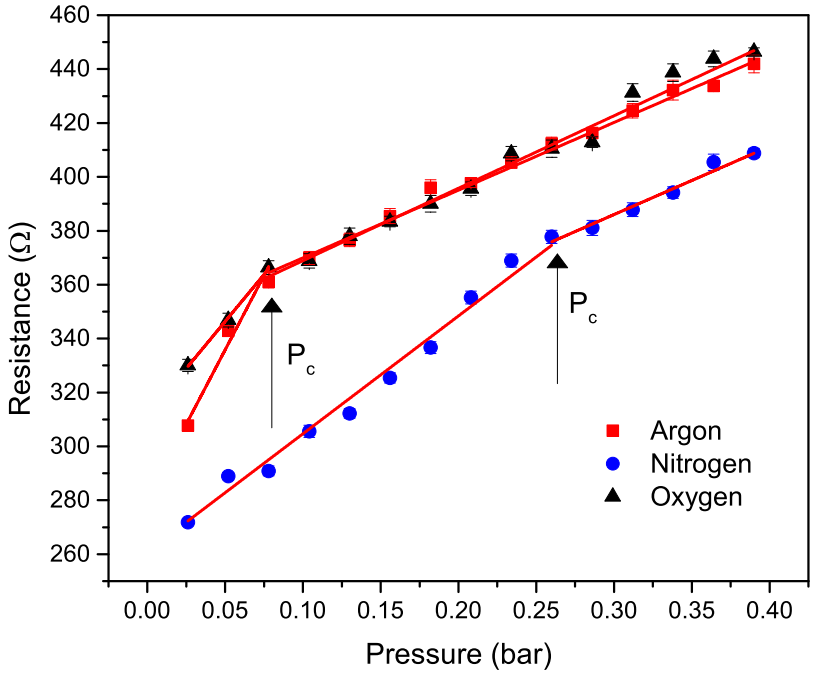

FIGURE 6.3: Resistance vs gas concentration for the three gases. The arrow marks the critical pressure (P_C) at which the slope changes distinctly. The red lines shows the linear fit.

x is the centre of the semicircle on abscissa. The resistance obtained from the fitting, for various gas concentrations are plotted in fig. 6.3. The resistance values are found to increase with increase in gas concentration. For all the three gases, initially the resistance increases rapidly, and then slowly. This change-over point (say critical pressure (P_c) is shown as arrow in fig.6.3. On the either side of P_c, the increase in resistance is almost linear. Beyond P_c, the resistance values for Ar and O_2 are same where as below P_c, that of Ar is slightly is lower. The P_c position for Ar and O_2 is almost same 0.078bar. The data for N_2 is slightly different and its overall value is lower than either of the two gases. Moreover the P_c position has also moved to higher value 0.26bar. The experimental data points above and below P_c are fitted linearly where the slope gives the sensitivity. In the region above P_c the slopes are 251, 252 and 268 for argon, nitrogen and oxygen respectively. Whereas in the region below P_c the slopes are 1103, 437, 696 for argon, nitrogen and oxygen respectively. So the maximum sensitivity is obtained for argon for lower gas concentration.

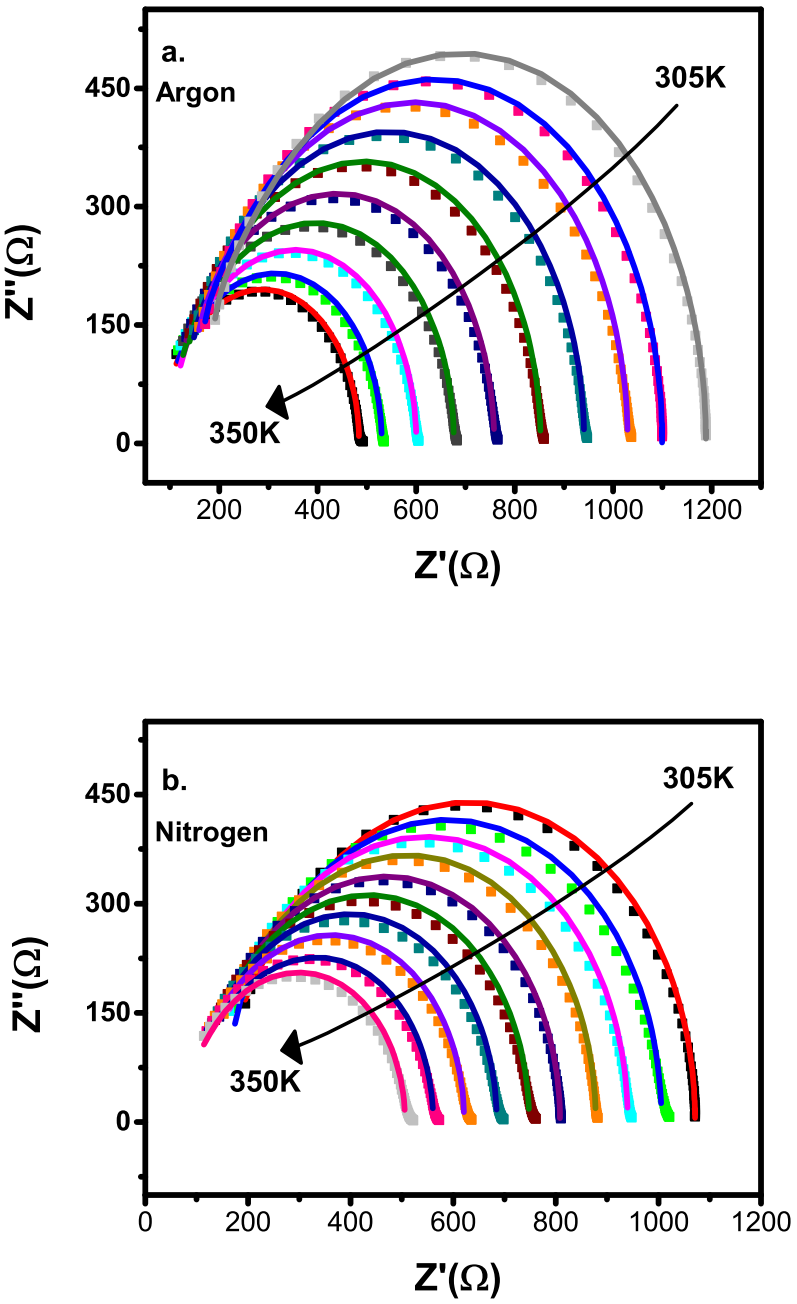

FIGURE 6.4: Nyquist Plot at various temperatures under atmospheric pressure of (a) Ar (b) N_2 environments. The arrow marks the direction of temperature increase.

For the versatility of LNM in gas sensing application, the impedance measurements for all the three gases are done at elevated temperatures upto 350K in the interval of 5K. The Nyquist plots at various temperatures for Argon, Oxygen and Nitrogen (under atmospheric pressure) are shown in fig.6.4a, 6.4b & 6.5c respectively. The solid lines represent the fitting to the experimental data via eq. 6.1. The fitted

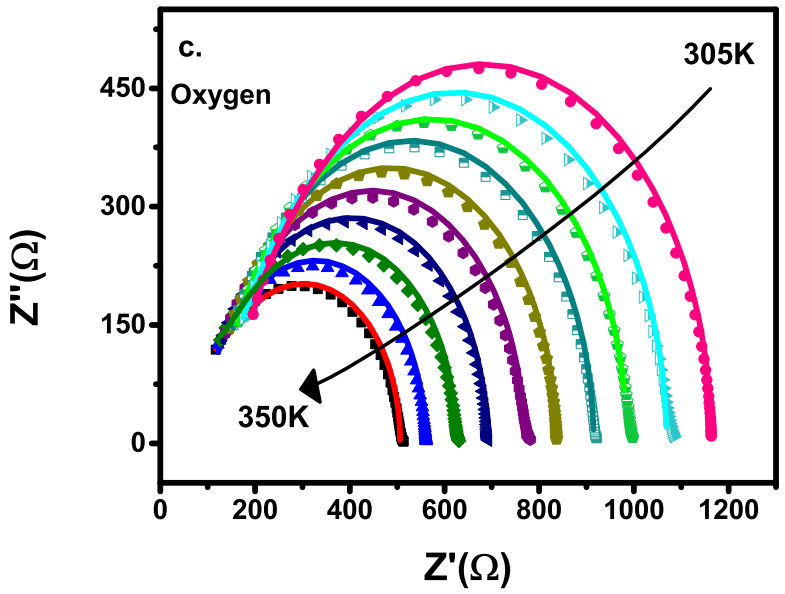

FIGURE 6.5: Nyquist Plot at various temperatures under atmospheric pressure of (c)O_2 environments. The arrow marks the direction of temperature increase.

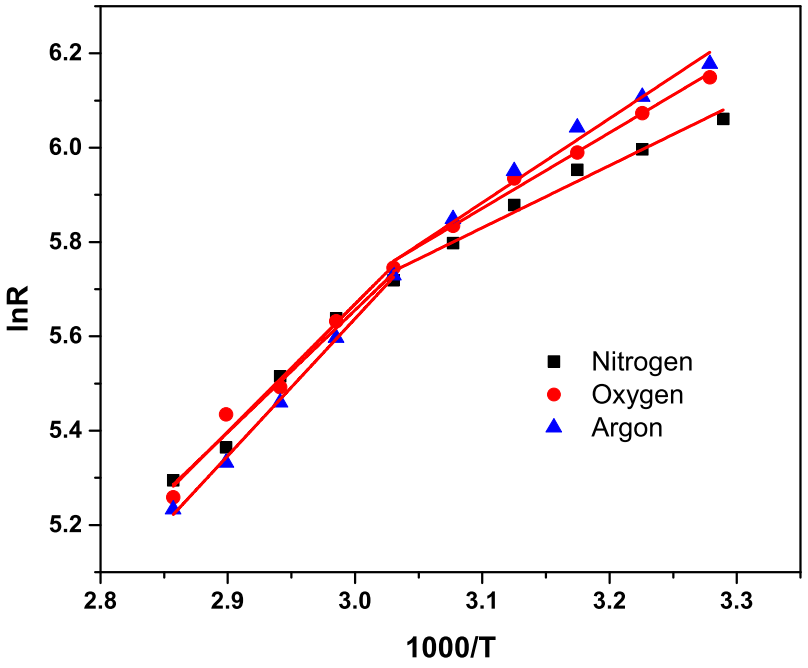

FIGURE 6.6: Thermally activated behaviour of LNM for all three gases. The red line show the fitting of the experimental data via equation 6.2.

semicircles show a decrease in semicircular radius with increase in temperature. Such behaviour indicates activated nature and hence the resistance values obtained

are examined for activated behaviour via Arrhenius equation (eq.6.2).

$$R = R_0 \ \ exp(E_a/KT) \tag{6.2}$$

where E_a, is the activation energy, K is the Boltzmann's constant and T is the temperature (in Kelvin). Fig.6.6 shows the plot of logarithmic resistance with inverse of temperature. The obtained activation energies for the three gases at two temperatures ranges viz. high temperature and near room temperature are shown in table 6.1.

Gas	Near room temperature	High temperature
Argon	0.16	0.25
Nitrogen	0.12	0.23
Oxygen	0.14	0.24

TABLE 6.1: Activation energy (E_a) in eV for different gases in high and low temperature regions

Owing to spectacular properties (CMR, CMD, etc) of LNM, the above-mentioned measurements at room temperature are also repeated under magnetic field of 1T. Fig.6.7a,b&c show the Nyquist plots for the three gases (at atmospheric pressure) at zero and 1T magnetic field. Remarkable variations are observed for the measurements done under magnetic field: Ar purged sample shows negative magnetoimpedance, N_2 purged sample shows no magnetoimpedance whereas O_2 purged sample shows positive magnetoimpedance. To have a clear idea, the % magnetoimpedance(eq.6.3)

$$\%Magnetoimpedance = \frac{[Z(H) - Z(0)]}{Z(0)} \times 100 \tag{6.3}$$

is plotted as Bode plot (fig. 6.7d), where the above mentioned features are clearly seen with maximum magnetoimpedance (in magnitude) of $\sim$ 5% is observed in Argon environment.

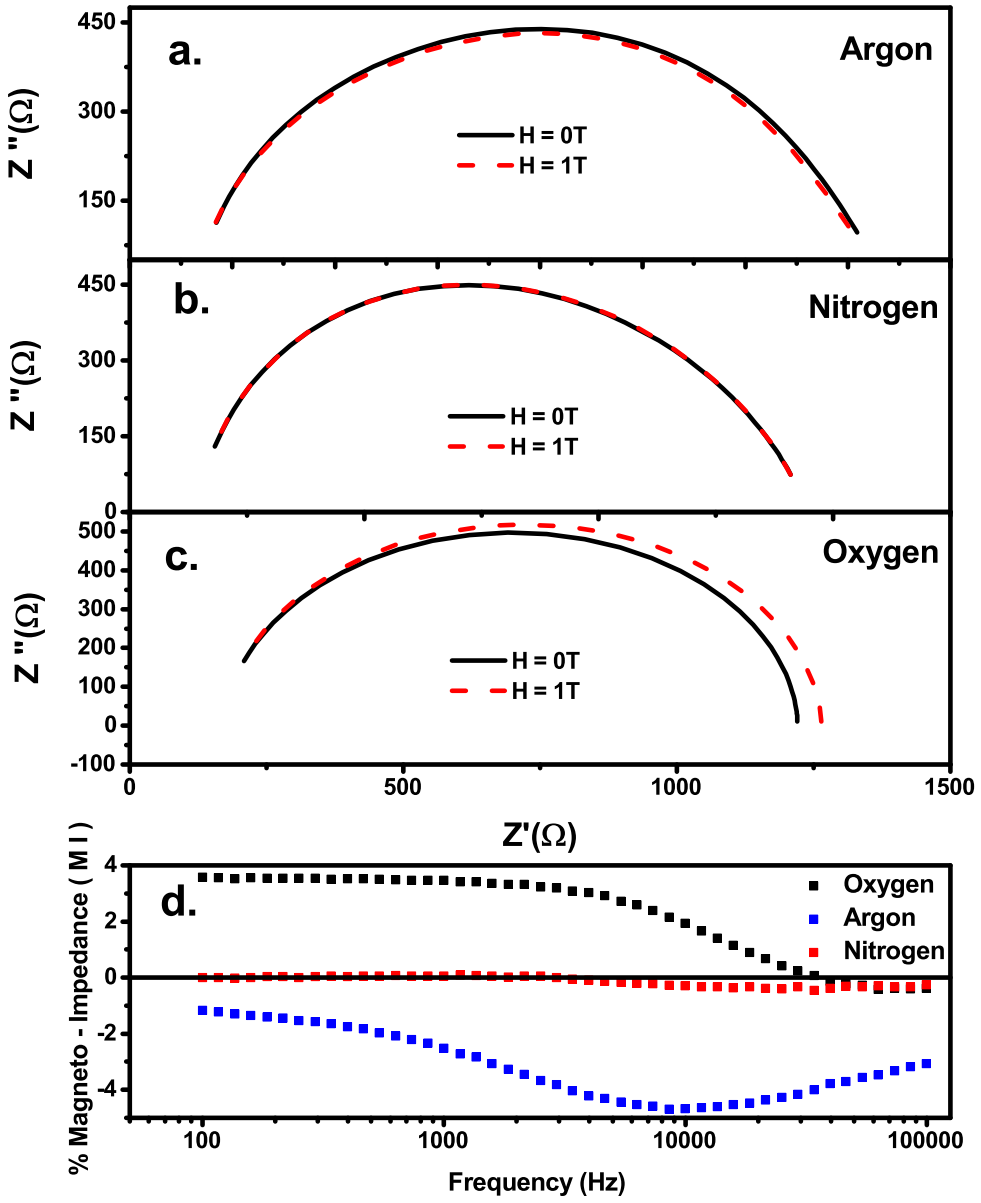

FIGURE 6.7: Nyquist Plot at 0T and 1T magnetic field at room temperature under atmospheric pressure of (a) Argon (b) Nitrogen (c) Oxygen environments. (d) Bode plot of Magnetoimpedance for different gaseous environments.

6.3 Conclusion

Impedance measurements at various stable temperatures are done on LNM under different gaseous (argon, nitrogen, oxygen) ambience with varied concentration. From the fitting of impedance data plotted in Cole-Cole formalism, the resistance (diameter of the semicircle) value shows strong dependency with respect to gaseous

concentration. Overall the resistance value increases with sharp change in slope at critical gas pressure P_C, as the gas concentration is increased. The sensitivity (slope change) is more below P_C and among the three it is highest for Argon. Resistance values at elevated temperatures show two distinct activated regimes with different activation energies. Magnetoimpedance at 1T magnetic field show a positive value for oxygen, negative value for argon and nearly zero for nitrogen atmosphere. The maximum magnetoimpedance of $\sim 5\%$ (in magnitude) is observed for Argon under 1T magnetic field. We have done a crude investigation of gas sensing property in LNM. So in future, the sensing device can be fabricated by making thin film of LNM and the sensing property can be extended to gas concentrations at ppm level as well as for various toxic gases.

Chapter 7

Conclusions and Scope of Future work

7.1 Conclusions

- Polycrystalline LMN and Cu doped samples are prepared via sol-gel nitrate combustion method. Modified LNM(M-LNM) is prepared by impregnation of LNM pellet.

- Rietveld refinement of XRD data confirms the biphasic nature of all samples with varying fraction of $R-3c$ & $Pbmn$ phases. Increase in $R-3c$ phase fraction is seen with Cu - doping. However increase in $Pbmn$ phase fraction is observed for M-LNM.

- Surface morphology study by FESEM show grain size of LNM and M-LNM is roughly around $\sim$ 30nm.

- From the magnetization data of LNM, it is observed that $R-3c$ and $Pbmn$ phase orders ferromagnetically at 277K and 160K respectively. With Cu^{2+} substitution the T_C value decreases for both the phases. This substitution has also enhanced the antiferromagnetic interactions in the sample, and thus variety of magnetic interactions which earlier were not seen properly

in LNM are now noticeable. The saturation magnetization and coerceivity are decreased with increase in Cu^{2+} content. For M-LNM the $R-3c$ phase magnetic transition is suppressed due to high fraction of $Pbnm$ phase content. The low temperature magnetization value is much higher in M-LNM than LNM. However the coerceivity in M-LNM is of lesser magnitude than LNM.

- Signature of Griffiths phase is observed in temperature dependent magnetization data of LNM. With increase in Cu^{2+} substitution, the strength of Griffiths phase increases with shifting of Griffiths range to lower temperatures. For M-LNM sample, signature of Griffiths phase is also observed.

- The relaxation dynamics of magnetic moments increases with increase in Cu^{2+} doping.

- The dielectric data shows, marginal increase in the intrinsic dielectric value, 1500 (x = 0) to 1700 (x = 0.1), but nearly two times rise in the dielectric loss. Due to partial substitution of Cu^{2+}, the activation energy for dielectric relaxation decreases, thus the temperature dependent dielectric plot shifts to lower temperature with Cu^{2+} doping.

- DC resistance as a function of temperature for all samples show hopping nature of conduction with extended hopping at room temperature and transition to Mott VRH at low temperature. Transition due to charge ordering is seen in the temperature range $230-245$K. The charge ordering effect decreases due to Cu^{2+} doping.

- Analysing the impedance data via Nyquist plot and the corresponding resistance, time constant and symmetric & asymmetric broadening parameters are obtained from the fitting by equivalent Harverliak-Negami equation. The time constants for $R-3c$ and $Pbnm$ phases show activated behaviour with activation energy 0.147eV and 0.088eV for $R-3c$ and $Pbnm$ phases respectively. Also, indication of strong magnetic ordering dependent dielectric relaxation is seen in the time constant plot. The values of symmetric and

asymmetric broadening parameters show Debye type relaxations in the ferromagnetic region of respective phases and Non- Debye nature before the ferromagnetic ordering temperature.

- Contrasting magnetoimpedance behaviours comprising +ve MI for LNM and −ve MI for M-LNM is seen. The magnetoimpedance is found to be strongly dependent on the magnetic states of the compound.

- The conductance vs voltage analysis predicts the tunnelling of charge carriers through the insulating barriers, as the conduction mechanism. Based on the magnetoconductance behaviour of LNM, a pictorial model of the biphasic LNM is presented (fig.5.7), according to which, in M-LNM the $Pbnm$ grains are connected to each other via shunt resistances with $R-3c$ phase embedded as island in the $Pbnm$ matrix. On the other hand, in LNM the $R-3c$ grains are connected via a thin layer of $Pbnm$ phase, which is acting as tunnelling barrier. The $Pbnm$ phase probably nucleates at the grain boundary and with increasing percentage, grain boundary becomes thick, isolating the islands of $R-3c$ phase.

- The isothermal D.C. magnetoresistance show positive magnetoresistance due to spin polarized tunnelling at 250K and 200K. The 100K magnetoresistance show normal tunnelling magnetoresistance behaviour, while 150K data represents a transition like region having minimal positive and negative magnetoresistance. However in M-LNM, magnetoresistance at the mentioned temperatures show negative magnetoresistance with large hysteresis between the field applied directions. Signature of inverse metamagnetic transition originating due to the dipolar field of $Pbnm$ phase on $R-3c$ phase is seen in M-LNM.

- Gas sensing property is successfully investigated in Argon, N_2 & O_2 environments. Among the three we got highest sensitivity for Argon. Sensitivity with magnetic field (Magnetoimpedance) of 1T show a positive value for oxygen, negative value for argon and nearly zero for nitrogen atmosphere.

The maximum magnetoimpedance of $\sim 5\%$ (in magnitude) is observed for Argon under 1T magnetic field.

7.2 Scope of Future work

In the thesis my focus mainly lies on the study of various physical properties and possible application of LNM and its derivatives. However I believe that the preliminary research output of this thesis can be extended to a next level.

1. We have investigated the compounds $La_2Ni_{1-x}Cu_xMnO_6$, $x = 0, 0.05\&0.1$. However for complete understanding of the structural transformations and related physical properties, the series of compounds $La_2Ni_{1-x}Cu_xMnO_6$, $x = 0 - 1$ can be investigated in due course of time.

2. We have done some preliminary investigation on Gd & Sr substituted LNM. The Sr substituted sample show some structural transformation. So both these series can be investigated in future.

3. Other prototype double perovskite of LNM, La_2CoMnO_6 exhibit various interesting properties viz. colossal magnetodielectricity and colossal magnetoresistance etc.. Many researchers have investigated this compound. However, a thorough investigation of dielectric relaxation parameters in the vicinity of the magnetic transition is necessary.

4. We have done a crude investigation of gas sensing property in LNM. So in future, the sensing device can be fabricated by making thin film of LNM and the sensing property can be extended to gas concentrations at ppm level as well as for various toxic gases.

5. We have done low temperature impedance measurement of LNM extensively. It can be carried out at higher temperatures to have more conclusive understandings of a.c relaxation phenomena.

6. High temperature magnetization measurements can be carried out to have distinctly clear picture on Griffiths phase. For M-LNM sample magnetization measurements at higher fields can be carried out to comment more on magnetic states.

7. We have studied hopping conduction behaviour of DC resistivity for all samples in the entire temperature range. However an entirely different conduction mechanism can be modelled. The charge ordering transition seen in DC resistivity can further be probed by other measurements like A.C susceptibility.

Appendix A

Interfacing the measuring Instruments through Labview

Depending on the required measurements, various instruments such as Electromagnet Power Supply (Kepco BOP 25 - 40MG), Lock in Amplifier (SRS 830), Temperature Controller (Lakeshore 331), Nano - Voltmeter (Kiethley 2182A), Current Source (Kiethley 6221), Electrometer (Keithley 6517B) are programmed for data acquisition through LabView software. Labview is a simple and powerful tool for data acquisition, where the user can view the behaviour of the data on-line through suitable graphics. The instruments are sequentially controlled for measurements like impedance, magnetoimpedance, dielectric, magnetodielectric, resistance, magnetoresistance, A.C susceptibility and $I \sim V$ characteristics. Few snapshots of on-line data acquisition are shown in the following figures.

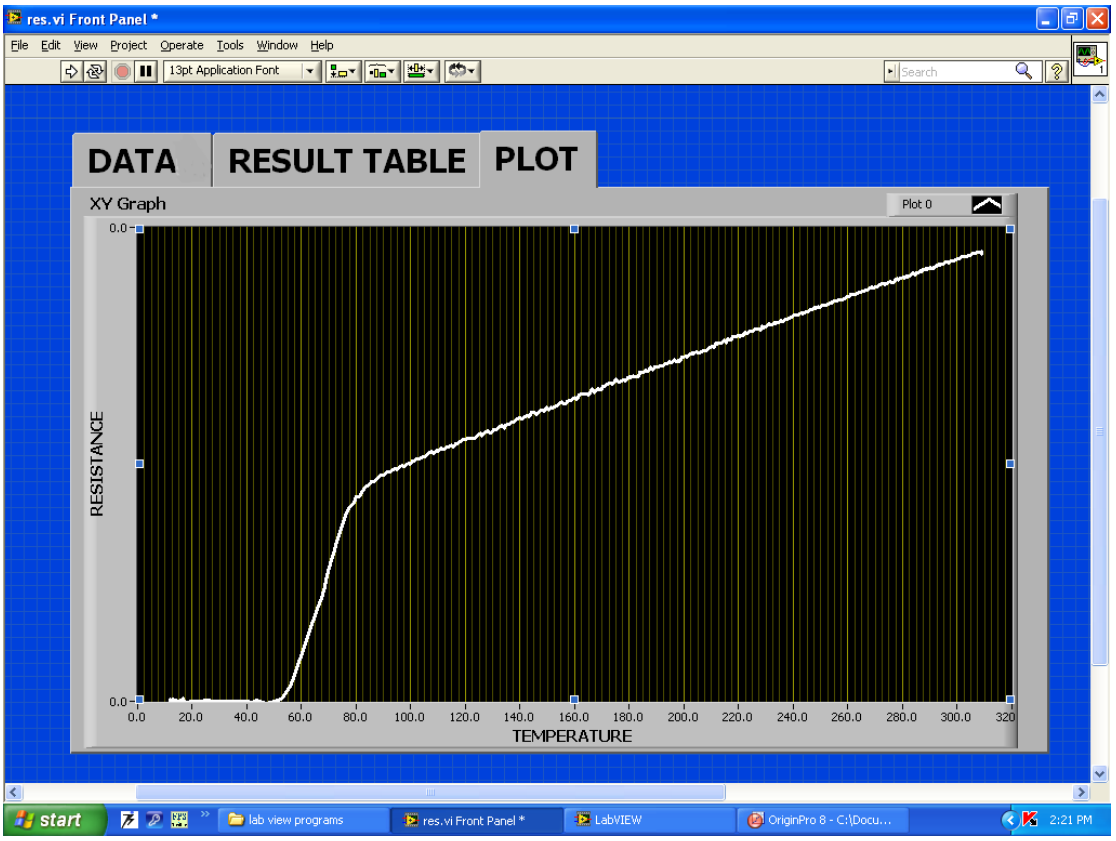

FIGURE A.1: Snapshot of temperature dependent resistance measurement. Current source, nano - voltmeter and temperature controller are interfaced for four probe resistance measurement. The plot in the graphics shows a superconducting transition.

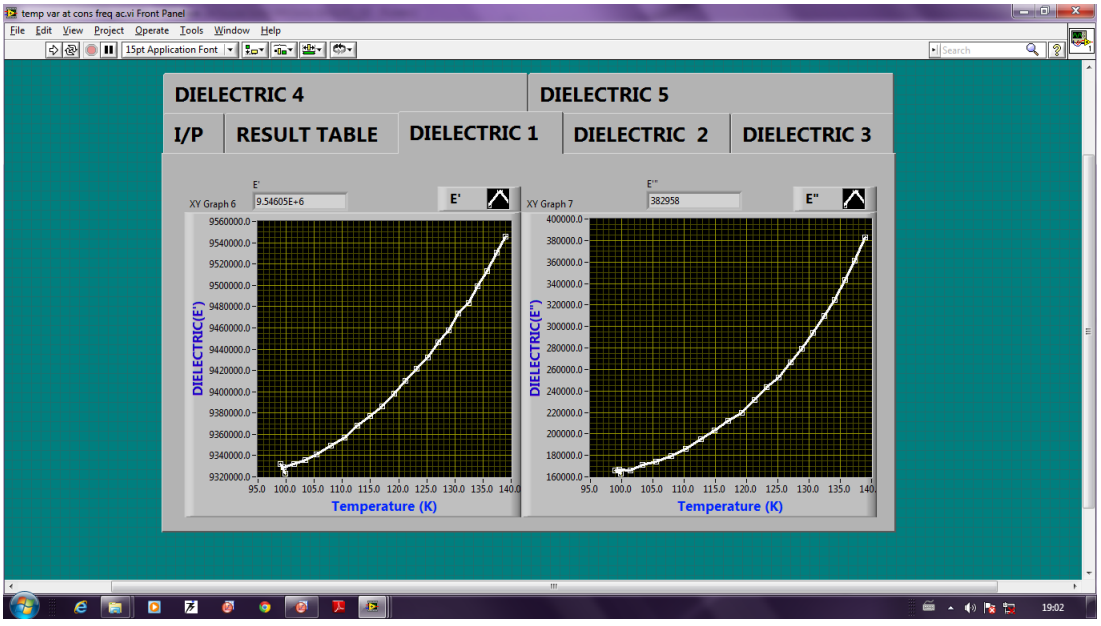

FIGURE A.2: Snapshot of temperature dependent dielectric measurement. Lock in Amplifier and temperature controller are interfaced for the measurement.

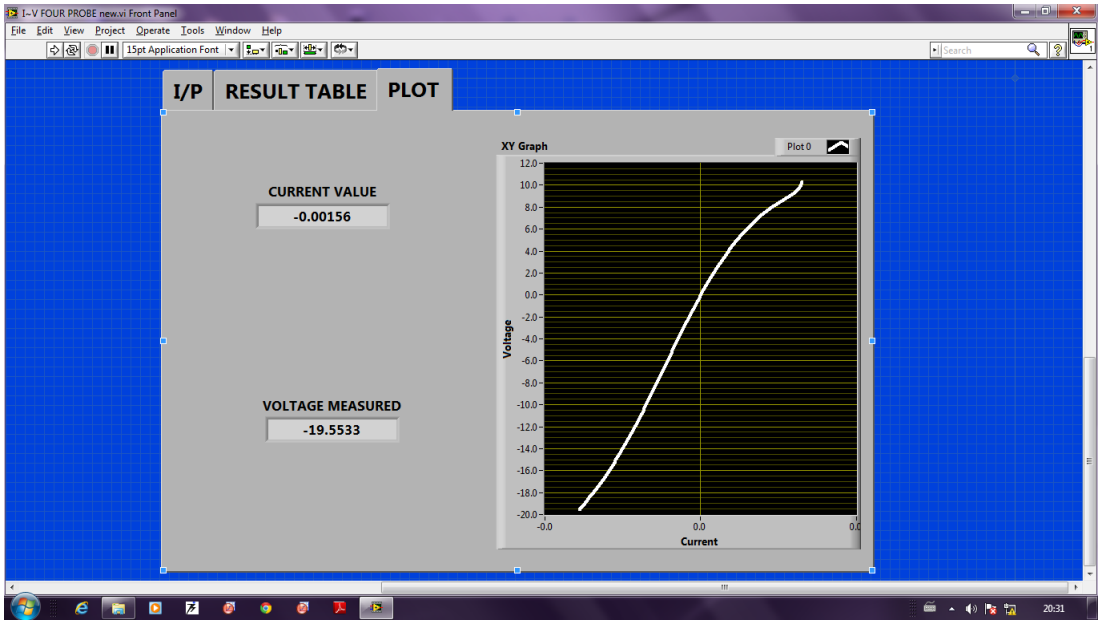

FIGURE A.3: Snapshot of $I \sim V$ characteristics. Current source, nano - voltmeter and temperature controller are interfaced for the measurement.

Bibliography

[1] Tatsumi Ishihara. *Perovskite Oxide for Solid Oxide Fuel Cells*. Springer, Oxford, 2009.

[2] Mark T. Anderson, Kevin B. Greenwood, Gregg A. Taylor, and Kenneth R. Poeppelmeier. B-cation arrangements in double perovskites. *Progress in Solid State Chemistry*, 22:197, 1993. URL http://www.sciencedirect.com/science/article/pii/007967869390004B.

[3] Yuichi Shimakawa, Masaki Azuma, and Noriya Ichikawa. Multiferroic compounds with double-perovskite structures. *Materials*, 4:153, 2011. URL http://www.mdpi.com/1996-1944/4/1/153.

[4] T. Saha-Dasgupta. Magnetism in double perovskites. *Journal of Superconductivity and Novel Magnetism*, 26:1991, 2013. URL http://link.springer.com/article/10.1007%2Fs10948-012-1920-7#.

[5] D. D. Sarma, Sugata Ray, K. Tanaka, M. Kobayashi, A. Fujimori, P. Sanyal, H. R. Krishnamurthy, and C. Dasgupta. Intergranular magnetoresistance in Sr_2FeMoO_6 from a magnetic tunnel barrier mechanism across grain boundaries. *Physical Review Letters*, 98:157205, 2007. URL http://link.aps.org/doi/10.1103/PhysRevLett.98.157205.

[6] K.-I. Kobayashi, T. Kimura, H. Sawada, K. Terakura, and Y. Tokura. Room-temperature magnetoresistance in an oxide material with an ordered double-perovskite structure. *Nature*, 395:677, 1998. URL http://dx.doi.org/10.1038/27167.

[7] M. C. Viola, M. J. Martínez-Lope, J. A. Alonso, P. Velasco, J. L. Martínez, J. C. Pedregosa, R. E. Carbonio, and M. T. Fernández-Díaz. Induction of Colossal Magnetoresistance in the Double Perovskite Sr_2CoMoO_6. *Chemistry of Materials*, 14:812, 2002. URL http://dx.doi.org/10.1021/cm011186j.

[8] D. Choudhury, P. Mandal, R. Mathieu, A. Hazarika, S. Rajan, A. Sundaresan, U. V. Waghmare, R. Knut, O. Karis, P. Nordblad, and D. D. Sarma. Near-Room-Temperature Colossal Magnetodielectricity and Multiglass Properties in Partially Disordered La_2NiMnO_6. *Physical Review Letters*, 108:127201, 2012. URL http://link.aps.org/doi/10.1103/PhysRevLett.108.127201.

[9] D. Serrate, J. M. D. Teresa, and M. R. Ibarra. Double perovskites with ferromagnetism above room temperature. *Journal of Physics: Condensed Matter*, 19:23201, 2007. URL http://stacks.iop.org/0953-8984/19/i=2/a=023201.

[10] N. S. Rogado, J. Li, A. W. Sleight, and M. A. Subramanian. Magnetocapacitance and Magnetoresistance Near Room Temperature in a Ferromagnetic Semiconductor: La_2NiMnO_6. *Advanced Materials*, 17:2225, 2005. URL http://dx.doi.org/10.1002/adma.200500737.

[11] A. Rebello and R. Mahendiran. Electric field-induced colossal electroresistance and its relaxation in multiferroic La_2NiMnO_6. *ArXiv e-prints*, 2009.

[12] M. A. Tanaka, Y. Shiji, T. Katsuragi, Y. Miyazaki, K. Mibu, K. Kondou, S. Kasai, and T. Ono. Magnetic and transport properties of spin-filtering tunnel junctions with magnetic insulator La_2NiMnO_6. *Journal of Physics: Conference Series*, 200:062032, 2010. URL http://stacks.iop.org/1742-6596/200/i=6/a=062032?key=crossref.4682115252174aaa85e1aba94fd80ccd.

[13] P. W. Anderson and H. Hasegawa. Considerations on double exchange. *Physical Review*, 100:675, 1955. URL http://link.aps.org/doi/10.1103/PhysRev.100.675.

[14] P. G. de Gennes. Effects of double exchange in magnetic crystals. *Physical Review*, 118:141, 1960. URL http://link.aps.org/doi/10.1103/PhysRev.118.141.

[15] Sanjeev Kumar and Pinaki Majumdar. Insulator-metal phase diagram of the optimally doped manganites from the disordered holstein-double exchange model. *Physical Review Letters*, 96:016602, 2006. URL http://link.aps.org/doi/10.1103/PhysRevLett.96.016602.

[16] Cengiz Cengiz Sen, Gonzalo Alvarez, Horacio Aliaga, and Elbio Dagotto. Colossal magnetoresistance observed in monte carlo simulations of the one and two-orbital models for manganites. *Physical Review B*, 73:224441, 2006. URL http://link.aps.org/doi/10.1103/PhysRevB.73.224441.

[17] Warren E. Pickett and David J. Singh. Electronic structure and half-metallic transport in the $La_{1-x}Ca_xMnO_3$ system. *Physical Review B*, 53:1146, 1996. URL http://link.aps.org/doi/10.1103/PhysRevB.53.1146.

[18] Stephen Blundell. *Magnetism in Condensed Matter*. Oxford University Press, University of Oxford, 2001.

[19] A. J. Millis. Lattice effects in magnetoresistive manganese perovskites. *Nature*, 392:147, 1998. URL http://dx.doi.org/10.1038/32348.

[20] A. K. Pramanik and A. Banerjee. Griffiths phase and its evolution with Mn-site disorder in the half-doped manganite $Pr_{0.5}Sr_{0.5}Mn_{1-y}Ga_yO_3$(y = 0.0, 0.025 and 0.05). *Physical Review B*, 81:24431, 2010. URL http://link.aps.org/doi/10.1103/PhysRevB.81.024431.

[21] H. S. Nair, D.A. Swain, N. Hariharan, S. Adiga, C. Narayana, and S. Elzabeth. Griffiths phase-like behavior and spin-phonon coupling in double perovskite Tb_2NiMnO_6. *Journal of Applied Physics*, 110:123919, 2011. URL http://scitation.aip.org/content/aip/journal/jap/110/12/10.1063/1.3671674.

[22] A. K. Biswal, J. Ray, P. D. Babu, V. Siruguri, and P. N. Vishwakarma. Signature of griffith singularity in half doped $LaMn_{0.5}Cu_{0.5}O_3$. *AIP Conference Proceedings*, 1591:1630, 2014. URL http://scitation.aip.org/content/aip/proceeding/aipcp/10.1063/1.4873058.

[23] Mathias Getzlaff. *Fundamentals of Magnetism*. Springer - Verlag, Berlin Heidelberg, 2008.

[24] P. Schiffer, A. P. Ramirez, W. Bao, and S-W. Cheong. Low temperature magnetoresistance and the magnetic phase diagram of $La_{0.75}Ca_{0.25}MnO_3$. *Physical Review Letters*, 75:3336, 1995. URL http://link.aps.org/doi/10.1103/PhysRevLett.75.3336.

[25] D. Tripathy, A. O. Adeyeye, and S. Shannigrahi. Effect of spacer layer thickness on the magnetic and magnetotransport properties of Fe_3O_4/Cu/$Ni_{80}Fe_{20}$ spin valve structures. *Physical Review B*, 75:012403, 2007. URL http://link.aps.org/doi/10.1103/PhysRevB.75.012403.

[26] M. N. Baibich, J. M. Broto, A. Fert, F. Nguyen Van Dau, F. Petroff, P. Etienne, G. Creuzet, A. Friederich, and J. Chazelas. Giant magnetoresistance of $(001)Fe/(001)Cr$ magnetic superlattices. *Physical Review Letters*, 61:2472, 1988. URL http://link.aps.org/doi/10.1103/PhysRevLett.61.2472.

[27] Jagadeesh S. Moodera, Janusz Nowak, and Rene J. M. van de Veerdonk. Interface magnetism and spin wave scattering in ferromagnet-insulator-ferromagnet tunnel junctions. *Physical Review Letters*, 80:2941, 1998. URL http://link.aps.org/doi/10.1103/PhysRevLett.80.2941.

[28] Anthony Arrott. Criterion for ferromagnetism from observations of magnetic isotherms. *Physics Review*, 108:1394, 1957. URL http://link.aps.org/doi/10.1103/PhysRev.108.1394.

[29] D. Fuchs, M. Wissinger, J. Schmalian, C.-L. Huang, R. Fromknecht, R. Schneider, and H. v. Löhneysen. Critical scaling analysis of the itinerant ferromagnet $Sr_{1-x}Ca_xRuO_3$. *Physical Review B*, 89:174405, 2014. URL http://link.aps.org/doi/10.1103/PhysRevB.89.174405.

[30] Sunil Nair, A. Banerjee, A. V. Narlikar, D. Prabhakaran, and A. T. Boothroyd. Observation of three-dimensional heisenberg-like ferromagnetism in single crystal $La_{0.875}Sr_{0.125}Mno_3$. *Physical Review B*, 68:132404, 2003. URL http://link.aps.org/doi/10.1103/PhysRevB.68.132404.

[31] Anthony Arrott and John E. Noakes. Approximate equation of state for nickel near its critical temperature. *Physical Review Letters*, 19:786, 1967. URL http://link.aps.org/doi/10.1103/PhysRevLett.19.786.

[32] Evgenij Barsoukov and J.Ross Macdonald. *Impedance Spectroscopy Theory, Experiment and Applications*. Wiley-Interscience, New Jersey, 2005.

[33] Arthur R. Von Hippel. *Dielectrics and Waves*. The M.I.T. Press, Massachusetts, 1964.

[34] S. Havriliak and S. Negami. A complex plane representation of dielectric and mechanical relaxation processes in some polymers. *Polymer*, 8: 161, 1967. URL http://www.sciencedirect.com/science/article/pii/0032386167900213.

[35] Pradeep Kumar, Somnath Ghara, B. Rajeswaran, D.V.S. Muthu, A. Sundaresan, and A.K. Sood. Temperature dependent magnetic, dielectric and raman studies of partially disordered La_2NiMnO_6. *Solid State Communications*, 184:47, 2014. URL http://www.sciencedirect.com/science/article/pii/S0038109814000076.

[36] R. I. Dass, J.Q. Yan, and J. B. Goodenough. Oxygen stoichiometry, ferromagnetism, and transport properties of $La_{2-x}NiMnO_{6+\delta}$. *Physical Review B*, 68:64415, 2003. URL http://link.aps.org/doi/10.1103/PhysRevB.68.064415.

[37] A. Wold, R. J. Arnott, and J. B. Goodenough. Some magnetic and crystallographic properties of the system $LaMn_{1-x}Ni_xO_{3+\lambda}$. *Journal of Applied Physics*, 29:387, 1958. URL http://scitation.aip.org/content/aip/journal/jap/29/3/10.1063/1.1723147.

[38] Min Zhu, Yong Lin, Edward W. C. Lo, Qiong Wang, Zhengjie Zhao, and Wenhui Xie. Electronic and magnetic properties of La_2NiMnO_6 and La_2CoMnO_6 with cationic ordering. *Applied Physics Letters*, 100:062406, 2012. URL http://scitation.aip.org/content/aip/journal/apl/100/6/10.1063/1.3683550.

[39] C. L. Bull, D. Gleeson, and K. S. Knight. Determination of *B*-site ordering and structural transformations in the mixed transition metal perovskites La_2CoMnO_6 and La_2NiMnO_6. *Journal of Physics: Condensed Matter*, 15: 4927, 2003. URL http://stacks.iop.org/0953-8984/15/i=29/a=304.

[40] Farheen N. Sayed, S.N. Achary, O.D. Jayakumar, S.K. Deshpande, P.S.R. Krishna, S. Chatterjee, P. Ayyub, and A.K. Tyagi. Role of annealing conditions on the ferromagnetic and dielectric properties of La_2NiMnO_6. *Journal of Materials Research*, 26:567, 2011. URL http://journals.cambridge.org/article_S0884291411000045.

[41] M. G. Masud, A. Ghosh, J. Sannigrahi, and B. K. Chaudhuri. Observation of relaxor ferroelectricity and multiferroic behaviour in nanoparticles of the ferromagnetic semiconductor La_2NiMnO_6. *Journal of Physics: Condensed Matter*, 24:295902, 2012. URL http://stacks.iop.org/0953-8984/24/i=29/a=295902.

[42] K. D. Chandrasekhar, A. K. Das, and A. Venimadhav. Spin glass behaviour and extrinsic origin of magnetodielectric effect in non-multiferroic La_2NiMnO_6 nanoparticles. *Journal of Physics: Condensed Matter*, 24: 376003, 2012. URL http://stacks.iop.org/0953-8984/24/i=37/a=376003.

[43] J. Blasco, M. C. Sánchez, J. Pérez-Cacho, J. García, G. Subías, and J. Campo. Synthesis and structural study of $LaNi_{1-x}Mn_xO_{3+\delta}$ perovskites. *Journal of Physics and Chemistry of Solids*, 63:781, 2002. URL http://www.sciencedirect.com/science/article/pii/S0022369701002281.

[44] V. L. J. Joly, P. A. Joy, S. K. Date, and C. S. Gopinath. Two ferromagnetic phases with different spin states of Mn and Ni in $LaMn_{0.5}Ni_{0.5}O_3$. *Physical Review B*, 65:184416, 2002. URL http://link.aps.org/doi/10.1103/PhysRevB.65.184416.

[45] S.F. Matar, M.A. Subramanian, A. Villesuzanne, V. Eyert, and M.-H. Whangbo. First principles investigation of the electronic structure of La_2NiMnO_6: An insulating ferromagnet. *Journal of Magnetism and Magnetic Materials*, 308:116, 2007. URL http://www.sciencedirect.com/science/article/pii/S0304885306008171.

[46] M. Balli, P. Fournier, S. Jandl, and M. M. Gospodinov. A study of the phase transition and magnetocaloric effect in multiferroic La_2NiMnO_6 single crystals. *Journal of Applied Physics*, 115:173904, 2014. URL http://scitation.aip.org/content/aip/journal/jap/115/17/10.1063/1.4874943.

[47] R. J. Booth, R. Fillman, H. Whitaker, Nag Abanti, R.M. Tiwari, K.V. Ramanujachary, Gopalakrishnan J., and S.E. Lofland. An investigation of structural, magnetic and dielectric properties of R_2NiMnO_6(R = rare earth, Y). *Materials Research Bulletin*, 44:1559, 2009. URL http://www.sciencedirect.com/science/article/pii/S0025540809000609.

[48] S. Zhao, L. Shi, S. Zhou, J. Zhao, H. Yang, and Y. Guo. Size-dependent magnetic properties and Raman spectra of La_2NiMnO_6 nanoparticles. *Journal of Applied Physics*, 106:123901, 2009. URL http://scitation.aip.org/content/aip/journal/jap/106/12/10.1063/1.3269707.

[49] M. N. Iliev, H. Guo, and A. Gupta. Raman spectroscopy evidence of strong spin-phonon coupling in epitaxial thin films of the double perovskite La_2NiMnO_6. *Applied Physics Letters*, 90:151914, 2007. URL http://scitation.aip.org/content/aip/journal/apl/90/15/10.1063/1.2721142.

[50] S. Zhou, L. Shi, H. Yang, and J. Zhao. Evidence of short-range magnetic ordering above T_C in the double perovskite La_2NiMnO_6. *Applied Physics Letters*, 91:172505, 2007. URL http://scitation.aip.org/content/aip/journal/apl/91/17/10.1063/1.2801694.

[51] Y. Q. Lin, X. M. Chen, and X. Q. Liu. Relaxor-like dielectric behavior in La_2NiMnO_6 double perovskite ceramics. *Solid State Communications*, 149: 784, 2009. URL http://www.sciencedirect.com/science/article/pii/S0038109809001057.

[52] K. D. Chandrasekhar, A. K. Das, C. Mitra, and A. Venimadhav. The extrinsic origin of the magnetodielectric effect in the double perovskite La_2NiMnO_6. *Journal of Physics: Condensed Matter*, 24:495901, 2012. URL http://stacks.iop.org/0953-8984/24/i=49/a=495901.

[53] Zhiqing Zhang, Hongbin Jian, Xianwu Tang, Jianming Dai, Xuebin Zhu, and Yuping Sun. Structural, magnetic and dielectric properties of La_2NiMnO_6 thin film by chemical solution deposition method. *Journal of Sol-Gel Science and Technology*, 61:224, 2012. ISSN 0928. URL http://dx.doi.org/10.1007/s10971-011-2617-2.

[54] Zhiqing Zhang, Hongbin Jian, Xianwu Tang, Jie Yang, Xuebin Zhu, and Yuping Sun. Synthesis and characterization of ordered and disordered polycrystalline La_2NiMnO_6 thin films by sol-gel. *Dalton Transactions*, 41:11836, 2012. URL http://dx.doi.org/10.1039/C2DT31214J.

[55] A. K. Biswal, J. Ray, P. D. Babu, V. Siruguri, and P. N. Vishwakarma. Dielectric relaxations in La_2NiMnO_6 with signatures of griffiths phase. *Journal of Applied Physics*, 115:194106, 2014. URL http://scitation.aip.org/content/aip/journal/jap/115/19/10.1063/1.4876723.

[56] Yuqiao Guo, Lei Shi, Shiming Zhou, Jiyin Zhao, and Wenjie Liu. Near room-temperature magnetoresistance effect in double perovskite La_2NiMnO_6. *Applied Physics Letters*, 102:222401, 2013. URL http://scitation.aip.org/content/aip/journal/apl/102/22/10.1063/1.4808437.

[57] M. Hashisaka, D. Kan, A. Masuno, T. Terashima, M. Takano, and K. Mibu. Spin-filtering effect of ferromagnetic semiconductor La_2NiMnO_6. *Journal of Magnetism and Magnetic Materials*, 310:1975, 2007. URL http://www.sciencedirect.com/science/article/pii/S0304885306023468.

[58] Craig L. Bull and Paul F. McMillan. Raman scattering study and electrical properties characterization of elpasolite perovskites $Ln_2(BB')O_6(Ln - La, Sm \ldots Gd$ and $B, B' = Ni, Co, Mn)$. *Journal of Solid State Chemistry*, 177:2323, 2004. URL http://www.sciencedirect.com/science/article/pii/S0022459604000994.

[59] Kaustuv Manna, A. K. Bera, Manish Jain, Suja Elizabeth, S. M. Yusuf, and P. S. Anil Kumar. Structural-modulation-driven spin canting and reentrant glassy magnetic phase in ferromagnetic Lu_2MnNiO_6. *Physical Review B*, 91:224420, 2015. URL http://link.aps.org/doi/10.1103/PhysRevB.91.224420.

[60] J.-S. Kang, H. J. Lee, D. H. Kim, S. Kolesnik, B. Dabrowski, K. Świerczek, Jieun Lee, Bongjae Kim, and B. I. Min. Valence and spin states, and the metal-insulator transition in ferromagnetic $La_{2-x}Sr_xMnNiO_6$. *Physical Review B*, 80:045115, 2009. URL http://link.aps.org/doi/10.1103/PhysRevB.80.045115.

[61] Bongjae Kim, Hong Chul Choi, Beom Hyun Kim, and B. I. Min. Electronic structure and magnetic properties of hole-carrier-doped La_2MnNiO_6: $La_{2-x}Sr_xMnNiO_6$. *Physical Review B*, 81:224402, 2010. URL http://link.aps.org/doi/10.1103/PhysRevB.81.224402.

[62] Yuqiao Guo, Lei Shi, Shiming Zhou, Jiyin Zhao, Cailin Wang, Wenjie Liu, and Shiqiang Wei. Tunable exchange bias effect in Sr-doped double perovskite La_2MnNiO_6. *Journal of Physics D: Applied Physics*, 46:175302, 2013. URL http://stacks.iop.org/0022-3727/46/i=17/a=175302.

[63] Yuqiao Guo, Lei Shi, Shiming Zhou, Jiyin Zhao, and Shiqiang Wei. Local valence and hole-doping effect on magnetic properties in double perovskite

La_2MnNiO_6. *Journal of Superconductivity and Novel Magnetism*, 26:3287, 2013. URL http://dx.doi.org/10.1007/s10948-013-2168-6.

[64] Wenjuan Shan, Jiali Yang, Lihua Yang, and Na Ma. Catalytic combustion of soot particulates over $La_{2-x}K_xNiMnO_6$ catalysts. *Journal of Natural Gas Chemistry*, 20:384, 2011. URL http://www.sciencedirect.com/science/article/pii/S1003995310602022.

[65] W. Z. Yang, X. Q. Liu, Y. Q. Lin, and X. M. Chen. Structure, magnetic, and dielectric properties of $La_2Ni(Mn_{1-x}Ti_x)O_6$ ceramics. *Journal of Applied Physics*, 111:084106, 2012. URL http://scitation.aip.org/content/aip/journal/jap/111/8/10.1063/1.4704392.

[66] Y. Q. Lin and X. M. Chen. Dielectric relaxation and polaronic conduction in double perovskite La_2MgMnO_6. *Applied Physics Letters*, 96:142902, 2010. URL http://scitation.aip.org/content/aip/journal/apl/96/14/10.1063/1.3377906.

[67] C.W. Nan, L. Liu, N. Cai, J. Zhai, Y. Ye, Y. H. Lin, L. J. Dong, and C. X. Xiong. A three-phase magnetoelectric composite of piezoelectric ceramics, rare-earth iron alloys, and polymer. *Applied Physics Letters*, 81:3831, 2002. URL http://scitation.aip.org/content/aip/journal/apl/81/20/10.1063/1.1521247.

[68] M. K. Lee, T. K. Nath, C. B. Eom, M. C. Smoak, and F. Tsui. Strain modification of epitaxial perovskite oxide thin films using structural transitions of ferroelectric $BaTiO_3$ substrate. *Applied Physics Letters*, 77:3547, 2000. URL http://scitation.aip.org/content/aip/journal/apl/77/22/10.1063/1.1328762.

[69] X. Yuan, Q. Li, J. Hu, and M. Xu. Unusual dynamic magnetic behavior of polycrystalline La_2NiMnO_6. *Physica B: Condensed Matter*, 424: 73, 2013. URL http://www.sciencedirect.com/science/article/pii/S0921452613002913.

[70] P.M. Pechini. Method of preparing lead and alkaline earth titanates and niobates and coating method using the same to form a capacitor, 1967. URL https://www.google.com/patents/US3330697. US Patent 3,330,697.

[71] L.A. Chick, L.R. Pederson, G.D. Maupin, J.L. Bates, L.E. Thomas, and G.J. Exarhos. Glycine-nitrate combustion synthesis of oxide ceramic powders. *Materials Letters*, 10:6, 1990. URL http://www.sciencedirect.com/science/article/pii/0167577X90900035.

[72] J. B. Goodenough. Theory of the Role of Covalence in the Perovskite-Type Manganites [La,M(II)]MnO_3. *Physical Review*, 100:564, 1955. URL http://link.aps.org/doi/10.1103/PhysRev.100.564.

[73] F. N. Sayed, S. N. Achary, O. D. Jayakumar, S. K. Deshpande, P. S. R. Krishna, S. Chatterjee, P. Ayyub, and A. K. Tyagi. Role of annealing conditions on the ferromagnetic and dielectric properties of La_2NiMnO_6. *Journal of Materials Research*, 26:567, 2011. URL http://journals.cambridge.org/article_S0884291411000045.

[74] D. Haskel, G. Fabbris, N. M. Souza-Neto, M. van Veenendaal, G. Shen, A. E. Smith, and M. A. Subramanian. Stability of the ferromagnetic ground state of La_2NiMnO_6 against large compressive stress. *Physical Review B*, 84:100403, 2011. URL http://link.aps.org/doi/10.1103/PhysRevB.84.100403.

[75] H. Das, U. V. Waghmare, T. Saha-Dasgupta, and D. D. Sarma. Theoretical evidence and chemical origin of the magnetism-dependent electrostructural coupling in La_2NiMnO_6. *Physical Review B*, 79:144403, 2009. URL http://link.aps.org/doi/10.1103/PhysRevB.79.144403.

[76] H. Das, U. V. Waghmare, T. Saha-Dasgupta, and D. D. Sarma. Electronic Structure, Phonons, and Dielectric Anomaly in Ferromagnetic Insulating Double Pervoskite La_2NiMnO_6. *Physical Review Letters*, 100:186402, 2008. URL http://link.aps.org/doi/10.1103/PhysRevLett.100.186402.

[77] M. P. Singh, K. D. Truong, S. Jandl, and P. Fournier. Long-range Ni/Mn structural order in epitaxial double perovskite La_2NiMnO_6 thin films. *Physical Review B*, 79:224421, 2009. URL http://link.aps.org/doi/10.1103/PhysRevB.79.224421.

[78] İ. Pehlivan, R. Marsal, P. Georén, C. G. Granqvist, and G. A. Niklasson. Ionic relaxation in polyethyleneimine-lithium bis(trifluoromethylsulfonyl) imide polymer electrolytes. *Journal of Applied Physics*, 108:074102, 2010. URL http://scitation.aip.org/content/aip/journal/jap/108/7/10.1063/1.3490133.

[79] N. F. Mott. *Metal-insulator transitions*. Taylor & Francis Ltd., London, 1975.

[80] P. N. Vishwakarma and S. V. Subramanyam. Hopping conduction in boron doped amorphous carbon films. *Journal of Applied Physics*, 100:113702, 2006. URL http://scitation.aip.org/content/aip/journal/jap/100/11/10.1063/1.2372585.

[81] M. Li, A. Feteira, and D. C. Sinclair. Relaxor ferroelectric-like high effective permittivity in leaky dielectrics/oxide semiconductors induced by electrode effects: A case study of CuO ceramics. *Journal of Applied Physics*, 105: 114109, 2009. URL http://scitation.aip.org/content/aip/journal/jap/105/11/10.1063/1.3143014.

[82] H. Guo, A. Gupta, M. Varela, S. Pennycook, and J. Zhang. Local valence and magnetic characteristics of La_2NiMnO_6. *Physical Review B*, 79:172402, 2009. URL http://link.aps.org/doi/10.1103/PhysRevB.79.172402.

[83] R. B. Griffiths. Nonanalytic Behavior Above the Critical Point in a Random Ising Ferromagnet. *Physical Review Letters*, 23:17, 1969. URL http://link.aps.org/doi/10.1103/PhysRevLett.23.17.

[84] L. Y. Wang, Q. Li, Y. Y. Gong, Dun H. Wang, Q. Q. Cao, and Y. W. Du. The positive and negative magnetodielectric effects in double perovskite

Pr_2CoMnO_6. *Journal of the American Ceramic Society*, 97:2024, 2014. URL http://dx.doi.org/10.1111/jace.13009.

[85] M. B. Salamon, P. Lin, and S. H. Chun. Colossal magnetoresistance is a griffiths singularity. *Physical Review Letters*, 88:197203, 2002. URL http://link.aps.org/doi/10.1103/PhysRevLett.88.197203.

[86] A. H. Castro Neto, G. Castilla, and B. A. Jones. Non-fermi liquid behavior and griffiths phase in f-electron compounds. *Physical Reviews Letters*, 81: 3531, 1998. URL http://link.aps.org/doi/10.1103/PhysRevLett.81.3531.

[87] S.Maekawa & T.Shinjo. *Spin Dependent Transport in magnetic nanustructures*. CRC Press, 2002.

[88] T.R. McGuire and R.I. Potter. Anisotropic magnetoresistance in ferromagnetic 3d alloys. *IEEE Transactions on Magnetics*, 11:1018, 1975. URL http://ieeexplore.ieee.org/xpls/abs_all.jsp?arnumber=1058782&tag=1.

[89] Y. Tokura. *Colossal Magnetoresistive Oxides*. CRC Press, 2000.

[90] G. Binasch, P. Grünberg, F. Saurenbach, and W. Zinn. Enhanced magnetoresistance in layered magnetic structures with antiferromagnetic interlayer exchange. *Physical Review B*, 39:4828, 1989. URL http://link.aps.org/doi/10.1103/PhysRevB.39.4828.

[91] A. E. Berkowitz, J. R. Mitchell, M. J. Carey, A. P. Young, S. Zhang, F. E. Spada, F. T. Parker, A. Hutten, and G. Thomas. Giant magnetoresistance in heterogeneous $Cu - Co$ alloys. *Physical Review Letters*, 68:3745, 1992. URL http://link.aps.org/doi/10.1103/PhysRevLett.68.3745.

[92] John Q. Xiao, J. Samuel Jiang, and C. L. Chien. Giant magnetoresistance in nonmultilayer magnetic systems. *Physical Review Letters*, 68:3749, 1992. URL http://link.aps.org/doi/10.1103/PhysRevLett.68.3749.

[93] W. P. Pratt, S.F. Lee, J. M. Slaughter, R. Loloee, P. A. Schroeder, and J. Bass. Perpendicular giant magnetoresistances of Ag/Co multilayers. *Physical Review Letters*, 66:3060, 1991. URL http://link.aps.org/doi/10.1103/PhysRevLett.66.3060.

[94] A. Gerber, A. Milner, B. Groisman, M. Karpovsky, A. Gladkikh, and A. Sulpice. Magnetoresistance of granular ferromagnets. *Physical Review B*, 55:6446, 1997. URL http://link.aps.org/doi/10.1103/PhysRevB.55.6446.

[95] E. F. Ferrari, F. C. S. da Silva, and M. Knobel. Theory of giant magnetoresistance in granular alloys. *Physical Review B*, 59:8412, 1999. URL http://link.aps.org/doi/10.1103/PhysRevB.59.8412.

[96] W.M. Xu, P. Zheng, Z.J. Chen, and B.G. Shen. Giant magnetoresistance in $CrFeMn$ alloys. *Journal of Magnetism and Magnetic Materials*, 172:183, 1997. URL http://www.sciencedirect.com/science/article/pii/S0304885397001042.

[97] Y. Asano, A. Oguri, J. Inoue, and S. Maekawa. Giant magnetoresistance in magnetic granular alloys. *Physical Review B*, 49:12831, 1994. URL http://link.aps.org/doi/10.1103/PhysRevB.49.12831.

[98] M. Julliere. Tunneling between ferromagnetic films. *Physics Letters A*, 54:225, 1975. URL http://www.sciencedirect.com/science/article/pii/0375960175901747.

[99] D. Tripathy, A. O. Adeyeye, and S. Shannigrahi. Magnetic and tunneling magnetoresistive properties of an all-oxide $Fe_3O_4 - Al_2O_3$ granular system. *Physical Review B*, 76:174429, 2007. URL http://link.aps.org/doi/10.1103/PhysRevB.76.174429.

[100] J. S. Moodera, Lisa R. Kinder, Terrilyn M. Wong, and R. Meservey. Large magnetoresistance at room temperature in ferromagnetic thin film tunnel junctions. *Physical Review Letters*, 74:3273, 1995. URL http://link.aps.org/doi/10.1103/PhysRevLett.74.3273.

[101] G. X. Miao, Y. J. Park, J. S. Moodera, M. Seibt, G. Eilers, and M. Münzenberg. Disturbance of tunneling coherence by oxygen vacancy in epitaxial Fe/MgO/Fe magnetic tunnel junctions. *Physical Review Letters*, 100:246803, 2008. URL http://link.aps.org/doi/10.1103/PhysRevLett.100.246803.

[102] Stuart S. P. Parkin, Christian Kaiser, Alex Panchula, Philip M. Rice, Brian Hughes, Mahesh Samant, and See-Hun Yang. Giant tunnelling magnetoresistance at room temperature with $MgO(100)$ tunnel barriers. *Nature Materials*, 3:862, 2014. URL http://dx.doi.org/10.1038/nmat1256.

[103] K.-I. Kobayashi, T. Kimura, Y. Tomioka, H. Sawada, K. Terakura, and Y. Tokura. Intergrain tunneling magnetoresistance in polycrystals of the ordered double perovskite Sr_2FeReO_6. *Physical Review B*, 59:11159, 1999. URL http://link.aps.org/doi/10.1103/PhysRevB.59.11159.

[104] H. Y. Hwang, S-W. Cheong, N. P. Ong, and B. Batlogg. Spin-polarized intergrain tunneling in $La_{2/3}Sr_{1/3}MnO_3$. *Physical Review Letters*, 77:2041, 1996. URL http://link.aps.org/doi/10.1103/PhysRevLett.77.2041.

[105] P. Raychaudhuri, K. Sheshadri, P. Taneja, S. Bandyopadhyay, P. Ayyub, A. K. Nigam, R. Pinto, Sujeet Chaudhary, and S. B. Roy. Spin-polarized tunneling in the half-metallic ferromagnets $La_{0.7-x}Ho_xSr_{0.3}MnO_3 (x = 0$ and 0.15): Experiment and theory. *Physical Review B*, 59:13919, 1999. URL http://link.aps.org/doi/10.1103/PhysRevB.59.13919.

[106] P. Dey and T. K. Nath. Effect of grain size modulation on the magneto- and electronic-transport properties of $La_{0.7}Ca_{0.3}MnO_3$ nanoparticles: The role of spin-polarized tunneling at the enhanced grain surface. *Physical Review B*, 73:214425, 2006. URL http://link.aps.org/doi/10.1103/PhysRevB.73.214425.

[107] V. D. Okunev, R. Szymczak, M. Baran, H. Szymczak, and P. Gierłowski. Effect of coulomb blockade on the low- and high-temperature resistance of

$La_{1-x}M_xMnO_3$ (M = Sr, Ca) films. *Physical Review B*, 74:014404, 2006. URL http://link.aps.org/doi/10.1103/PhysRevB.74.014404.

[108] S. Takahashi and S. Maekawa. Effect of coulomb blockade on magnetoresistance in ferromagnetic tunnel junctions. *Physical Review Letters*, 80:1758, 1998. URL http://link.aps.org/doi/10.1103/PhysRevLett.80.1758.

[109] M. Retuerto, J. A. Alonso, M. J. Martínez-Lope, J. L. Martínez, and M. García-Hernández. Record saturation magnetization, curie temperature, and magnetoresistance in Sr_2FeMoO_6 double perovskite synthesized by wet-chemistry techniques. *Applied Physics Letters*, 85:266, 2004. URL http://scitation.aip.org/content/aip/journal/apl/85/2/10.1063/1.1772857.

[110] X. M. Feng, G. H. Rao, G. Y. Liu, H. F. Yang, W. F. Liu, Z. W. Ouyang, L. T. Yang, Z. X. Liu, R. C. Yu, C. Q. Jin, and J. K. Liang. Structure and magnetoresistance of the double perovskite Sr_2FeMoO_6 doped at the Fe site. *Journal of Physics: Condensed Matter*, 14:12503, 2002. URL http://stacks.iop.org/0953-8984/14/i=47/a=323.

[111] F. Bardelli, C. Meneghini, S. Mobilio, Sugata Ray, and D. D. Sarma. Local structure of $Sr_2FeMo_xW_{1-x}O_6$ double perovskites across the composition-driven metal to insulator transition. *Journal of Physics: Condensed Matter*, 21:195502, 2009. URL http://stacks.iop.org/0953-8984/21/i=19/a=195502.

[112] W. Zhong, W. Liu, C. T. Au, and Y. W. Du. Tunnelling magnetoresistance of double perovskite Sr_2FeMoO_6 enhanced by grain boundary adjustment. *Nanotechnology*, 17:250, 2006. URL http://stacks.iop.org/0957-4484/17/i=1/a=042.

[113] J. M. D. Coey, A. E. Berkowitz, Ll. Balcells, F. F. Putris, and A. Barry. Magnetoresistance of chromium dioxide powder compacts. *Physical Review Letters*, 80:3815, 1998. URL http://link.aps.org/doi/10.1103/PhysRevLett.80.3815.

[114] John G. Simmons. Generalized formula for the electric tunnel effect between similar electrodes separated by a thin insulating film. *Journal of Applied Physics*, 34:1793, 1963. URL http://scitation.aip.org/content/aip/journal/jap/34/6/10.1063/1.1702682.

[115] M. Ziese. Grain-boundary magnetoresistance in manganites: Spin-polarized inelastic tunneling through a spin-glass-like barrier. *Physical Review B*, 60:R738, 1999. URL http://link.aps.org/doi/10.1103/PhysRevB.60.R738.

[116] M.A. Bari, O. Cabeza, L. Capogna, P. Woodall, C.M. Muirhead, and M.G. Blamire. Conduction mechanisms in c-axis oriented YBCO based trilayer junctions with ferromagnetic $A_{0.7}B_{0.3}MnO_3$ manganite barriers. *Applied Superconductivity, IEEE Transactions on*, 7: 2304, 1997. URL http://ieeexplore.ieee.org/stamp/stamp.jsp?tp=&arnumber=621699&isnumber=13488.

[117] L.I. Glazman and K.A. Matveev. Inelastic tunneling across thin amorphous films. *Sov. Phys. JETP*, 67:6, 1988. URL http://www.jetp.ac.ru/cgi-bin/e/index/e/67/6/p1276?a=list.

[118] X. W. Li, A. Gupta, Gang Xiao, and G. Q. Gong. Low-field magnetoresistive properties of polycrystalline and epitaxial perovskite manganite films. *Applied Physics Letters*, 71:1124, 1997. URL http://scitation.aip.org/content/aip/journal/apl/71/8/10.1063/1.119747.

[119] K. Mukherjee, Sitikantha D. Das, Niharika Mohapatra, Kartik K. Iyer, and E. V. Sampathkumaran. Anomalous butterfly-shaped magnetoresistance loops in the alloy Tb_4LuSi_3. *Physical Review B*, 81:184434, 2010. URL http://link.aps.org/doi/10.1103/PhysRevB.81.184434.

[120] R. Hauser, E. Bauer, E. Gratz, H. Müller, M. Rotter, H. Michor, G. Hilscher, A. S. Markosyan, K. Kamishima, and T. Goto. Decoupling of the magnetic ordering of the rare-earth and the Co sublattice in $Er_{1-x}Y_xCo_2$ compounds

driven by substitution or pressure. *Physical Review B*, 61:1198, 2000. URL http://link.aps.org/doi/10.1103/PhysRevB.61.1198.

[121] Niharika Mohapatra, K. Mukherjee, Kartik K. Iyer, and E. V. Sampathkumaran. A first-order magnetic phase transition near 15K with novel magnetic-field-induced effects in Er_5Si_3. *Journal of Physics: Condensed Matter*, 23:496001, 2011. URL http://stacks.iop.org/0953-8984/23/i=49/a=496001.

[122] K Mukherjee, Kartik K Iyer, and E V Sampathkumaran. Evolution of a metastable phase with a magnetic phase coexistence phenomenon and its unusual sensitivity to magnetic field cycling in the alloys $Tb_{5-x}Lu_xSi_3(x \leq 0.7)$. *Journal of Physics: Condensed Matter*, 23:206002, 2011. URL http://stacks.iop.org/0953-8984/23/i=20/a=206002.

[123] P. Anil Kumar and D. D. Sarma. Effect of "dipolar-biasing" on the tunability of tunneling magnetoresistance in transition metal oxide systems. *Applied Physics Letters*, 100:262407, 2012. URL http://scitation.aip.org/content/aip/journal/apl/100/26/10.1063/1.4731206.

[124] A. Labidi, C. Jacolin, M. Bendahan, A. Abdelghani, J. Guérin, K. Aguir, and M. Maaref. Impedance spectroscopy on WO_3 gas sensor. *Sensors and Actuators B: Chemical*, 106:713, 2005. URL http://www.sciencedirect.com/science/article/pii/S0925400504006380.